UNIVERSITY OF SOUTHERN QUEENSLAND

DOPPLER IMAGING OF YOUNG SOLAR-TYPE STARS USING THE ANU 2.3 M SIDING SPRING TELESCOPE.

A dissertation submitted by
Donna Marie Burton
B.Sc. (Computing)

For the award of
Master of Science

School of Agricultural, Computational, Environmental Sciences
University of Southern Queensland

5 August 2013

Abstract

The study of surface activity on young solar-type stars provides an opportunity to improve understanding of stellar dynamos and indirectly gain insight into early solar evolution. Doppler Imaging (DI) can be used to map stellar surface activity, and utilises rotation-induced Doppler-broadening of spectral lines to calculate the surface distribution of a fundamental parameter such as temperature.

DI requires high-resolution spectroscopic observations distributed over one or more stellar rotation periods. To date only a limited number of single young solar analogues have been observed using this technique. Observations of many stars at various evolutionary states and with varying physical parameters are necessary to comprehensively constrain stellar dynamo models. These observations require long-term access to a telescope with a high-resolution echelle spectrograph to undertake multiple epoch studies of stellar activity.

This project has used the ANU 2.3 metre telescope to test Doppler Imaging with two active young stars, AB Doradus (AB Dor) and HIP43720, with the HIP43720 observations contemporaneous with the Anglo-Australian Telescope (AAT) observations.

Analysis of the AB Dor mapping and comparison of the 2.3 metre and AAT results for HIP43720 indicates that the ANU 2.3 metre telescope with its high resolution echelle spectrograph is capable of undertaking scientifically useful Doppler Imaging for stellar dynamo surveys.

Certification of Dissertation

I certify that this dissertation contains no material accepted for the award of any other degree or diploma in any university. To the best of my knowledge, it contains no material published or written by another person, except where due reference is made in the text.

Signature of Candidate	Date

ENDORSEMENT

Signature of Supervisor	Date

Dedication

Dedicated to Stan Ramage, the best father-in-law any girl could have. I am sorry that you never got to read it, but it is finally done. Thanks for believing in me!

Dedicated also to my parents, who passed away during this last 12 months, because of whom, I have always dared to reach for the stars and to believe all things are possible, as long as you work hard at it. Especially thanks to my Dad - who taught me to hate fences and that even a 'drover's brat' can be whatever they want to be! It just took me longer than most!

Acknowledgments

This has been no easy task, interesting, challenging and certainly a revealing journey into self-discovery. I have learnt that a document that compiles perfectly, somehow fails dismally just before it is due to journey through the ether to one's supervisor. I have learnt what procrastination is. For one, who hates ironing with a passion, it was enlightening to be reminded how many times I chose to iron instead of sit down and write this document. The observing tasks, in spite of the vagaries of weather, telescope and instrument gremlins were the fun bit; as was the initial data reduction and the sense of discovery. But there were those frustrating times, when nothing would work and a sneaky bracket in LaTex would take 5 hours to find; when drafts came back with seemingly more comments than the original word count. Do I regret it all? No way! Would I do it again? Too right! But, one would hope, wiser and much better organised and realising that all those early comments and warnings from my supervisors were true and the voice of experience not just nagging!

So, these have been an interesting few years. Life has a habit getting in the way of even our best intentions. Being privileged to have looked after my Father in Law prior to his passing and then losing both my parents within a year. The stress of many long interstate trips in their final months and weeks, giving up was a tempting alternative with a full time job, house, farm and a variety of animals to care for. But, being a 'drover's brat' as my Dad so liked to remind me – giving up is not in my make up! Even when the bush fires earlier this year burnt large parts of our property and provided even more excuses to avoid the writing tasks – the support and friendship of my partner Christopher, the community of Coonabarabran, the USQ team and my friends at Siding Spring I could not have got to this point. My PhD journey surely will have to be far less rocky!

I can't find the right superlative to express my thanks and appreciation to Dr Brad Carter and his wife Lynette, for their on-going support, friendship

and assistance during the last couple of years. Without their help and that of Dr Stephen Marsden and Ian Waite who have always made me feel a part of the team I would not have had the motivation to keep on keeping on.

Help was only an email, Skype or voice call away and when things seemed insurmountable, they helped put things into perspective. Stephen and Ian have been awesome in helping me get to terms with the idiosyncrasies of the data reduction software and in navigating the unique issues involved in getting it to work with 2.3metre data. Thanks have to go to Dr Gayandhi De Silva her help with telescope time proposals and helping me come to grips with reducing echelle spectra in IRAF. Dr Carolyn Brown - thanks for being the buffer this last exhausting week.

Thanks also to Dr Jean-François Donati for allowing our team access to his ESpRIT code and the permission to use his results from the AAT and to produce the 2002 map of AB Dor.

Thanks also to staff of the USQ Office of Research and Higher Degrees Staff and in particular especially Mrs Annmaree Jackson and Sophie Ivory for their assistance at being on the end of a phone and email to help me navigate the system.

There are several free online services, including: the SIMBAD database and the Vizier Service for Astronomical Catalogues, both operated at CDS, Strasbourg, France; NASA Astrophysics Data System (ADS) Data Services, operated by the Smithsonian Astrophysical Observatory (SAO); IRAF, distributed by the National Optical Astronomy Observatory and the Hipparcos and other astronomical catalogues that were essential tools used in my research.

Finally, a huge thank-you to my long suffering partner Chris, who has been so incredibly supportive of me throughout this adventure and who now knows far more about 'spotty' stars than he probably ever wanted to. Even though your patience has been so often sorely tested you have been my rock and when I wanted to give up, you were there to push and encourage me. Also, thanks to Judy, Sue and the rest of the ladies at the old Siding Spring Lodge and Exploratory for the coffee, chocolate and a place to hide out! Unfortunately, the Lodge was destroyed in the January 2013 fires but the memories live on! That's all Folks!

Weather is God's handicap for the world's greatest astronomers. Olin J Eggen

Contents

List of Figures

List of Tables

Chapter 1

Solar and Stellar Magnetic Activity

1.1 Introduction

Four centuries of in-depth study of the Sun has only served to reveal how little is understood about early solar evolution. This is particularly true in understanding the role the once rapidly rotating and intensely active young Sun played in the formation and early evolution of the solar system. Nevertheless, through the study of young solar type stars, insight can be gained into this early activity and the powerful internal magnetic dynamo of the Sun.

Stars less than 100 million years old are of interest in understanding how the Sun and its planetary system developed as this is the age range in which the formation of the solar system would have been essentially complete (Wetherill, 1980). So studying young solar analogues should provide a window into the characteristics and behaviour of the young Sun during the solar system's formative stages (Dorren and Guinan, 1994).

1.2 The Sun Today

The Sun today is a magnetically active, medium-sized, middle-aged main sequence, G2V dwarf star. Table 1.1 provides a summary of its fundamental physical characteristics.

The Sun supports a strong magnetic field which drives solar activity. This magnetic field varies from year to year and each 22 years it reverses polarity.

Observable signs of solar activity include sunspots, flares, prominences, and coronal mass ejections (CMEs).

Sunspots are the most readily visible signposts of solar activity and mark the location of strong magnetic fields arising from an internal regenerative dynamo (Berdyugina, 2005; Chaisson and McMillan, 2010).

Table 1.1: Summary of the Fundamental Physical Characteristics of the Sun, adapted from Phillips (2006) and Thomas and Weiss (2008)

Property	Magnitude
Solar Mass ($M_\odot$)	1.989 x 10^{30} kg
Equatorial Radius ($R_\odot$) of photosphere	6.955 x 10^8 m
Mean Diameter	1.392 x 10^9 m
Luminosity ($L_\odot$) from solar irradiance	3.854 x 10^{26} W
Effective Photospheric Temperature ($T_{eff\odot}$)	
from luminosity and Stefan-Boltzman Law	5,778 K
Age (from the age of oldest meteorites)	4.6 x 10^9 years
Spectral and Luminosity Type	G2 V
Mean Density	1.4 x 10^{34} kg m^{-3}
Equatorial Surface Gravity	274.0 ms^2
Rotational Velocity (at equator)	1.996 km s^{-1}
Rotational Period (equatorial)	25.05 days (Sidereal)
Rotational Period (80° latitude)	33.50 days (Sidereal)
Rotational Period (Poles)	34.30 days (Sidereal)
Rotational Velocity (Poles)	1.971 km s^{-1}
Mass Loss Rate	4 x 10^9 kg s^{-1}
Mean Distance to Earth (AU)	1.496 x 10^{11}m

1.3 Sunspots

Sunspots are temporary bi-polar phenomena that appear as darker areas on the solar disk caused by magnetic flux tubes. These flux tubes emerge at the photosphere restricting the motion of ionised gas to travel along field lines. This restriction inhibits the convective transport of energy to the surface, leading to the formation of areas of reduced surface temperature.

At temperatures of approximately 3,000–4,000 K, they become clearly visible as dark surface spots in contrast with the surrounding material, which is at a temperature of around 5,800 K (Rice, 2002).

Sunspots may be as large as 80,000 km in diameter, such as the one shown in Figure 1.1. Sunspot groups may last for up to six months and form the heart of the magnetically active regions, expanding and contracting as they move across the surface of the Sun (Mossman, 1989).

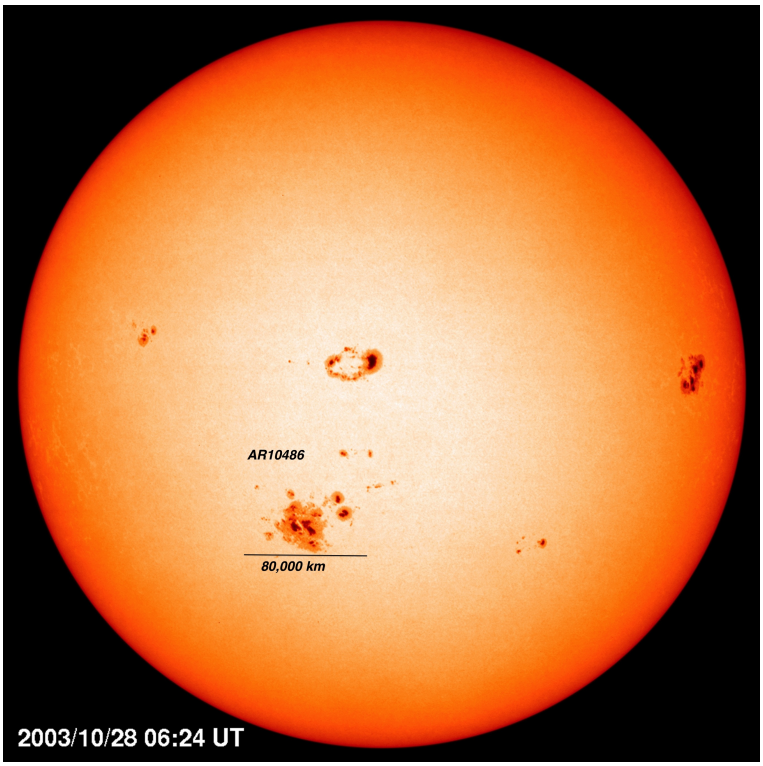

Figure 1.1: Active Region AR1048 is, at 80,000 km in diameter (the size of 15 Earths), the largest sunspot ever seen by SOHO up until this time. The image was taken on October 28, 2003. Credit: SOHO (ESA & NASA)

Figure 1.2 shows a high-resolution G-band image of a group of sunspots illustrating their basic anatomy. The main spot area consists of the darker umbra surrounded by the penumbra, and in this image, the filaments of the lighter penumbra are clearly visible. There are also smaller dark features known as pores that are essentially naked umbrae, or spots without penumbrae.

Figure 1.3 identifies the characteristics and positions of sunspots during the three stages of the solar cycle. Active regions and sunspots can be found

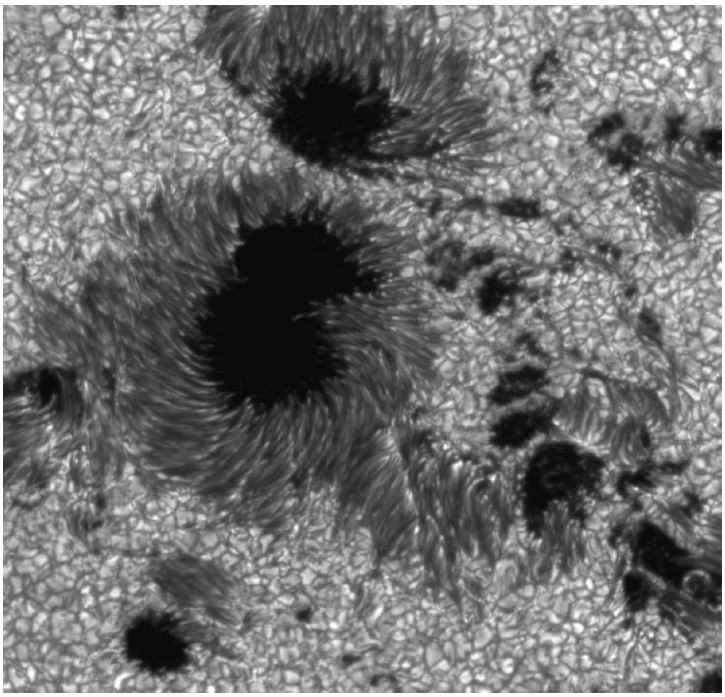

Figure 1.2: High-resolution G-band Sunspot image, obtained with the Swedish Solar Telescope, showing an active region with both sunspots and pores. Penumbral filaments are clearly visible, as is the surrounding pattern of granular-scale convection (Scharmer *et al.*, 2002). (Courtesy of the Royal Swedish Academy of Sciences)

to be concentrated in rotating bands about 15–30° either side of the equator with the average latitude varying in line with the solar cycle. The first spots of the new cycle begin to appear just after solar minimum and around 18 months before the old cycle ends. These appear at latitudes between 25–30° north and south of the equator (Zirin, 1988). There may also be a few remaining spots of the old cycle evident near the equator at the same time. As these spots from the old cycle dissipate, new larger and more numerous spots form. These new spots form into distinct sunspot groups often consisting of a larger leader spot or spots, followed, as the Sun rotates, by several smaller trailing spots.

The sunspot maximum occurs usually around mid-cycle. The main activity belts then are nearly 40° wide and centred on latitude 20° North/South. On very rare occasions there have been a few short-lived spots seen at latitudes of up to 70° North/South.

Very large complex groups of spots, often with complicated magnetic structure occur either side of the solar maximum. Then, as the cycle progresses newer spots form closer to the equator with the last sunspots of the cycle appearing around the latitude band 5–10° either side of the equator. Over the next few years, the number of spots decline. The active regions and spots developing at this time in the cycle tend to be smaller and be located at lower latitudes. This continues until the sunspot minimum again approaches, and if any spots are visible they will be near latitude 7° North/South (Zirin, 1988).

Sunspots have never been observed at solar latitudes greater than 70°. This is a significant difference between the Sun and young solar analogues (Thomas and Weiss, 2008).

The study of sunspots is essential to understanding the solar dynamo. There is a direct link between them and the presence of magnetic fields. This relationship means that they can be used as strong tracers of magnetic activity.

1.4 The Solar Cycle

The Sun exhibits cyclic behaviour in its activity, evidence of which is found in its spectral output as well as in spot coverage (Willson and Mordvinov, 2003). The amount of magnetic flux that rises up to the Sun's surface varies with time. This is the solar or sunspot cycle. In 1844, Samuel Schwabe showed definitively that the Sun went through cycles, when he announced his findings relating to sunspot activity variations over periods of 11 years.

These cycles refer to the periodic 11-year-long variation in the number of active features such as sunspots visible on the Sun's photosphere. The end of each 11-year sunspot cycle also corresponds to the reversal of the Sun's global magnetic field. The entire solar magnetic cycle, therefore, consists of two spot cycles and so lasts approximately 22 years.

The solar magnetic cycle consists of the dynamo periodically flipping between the poloidal and toroidal field configurations.

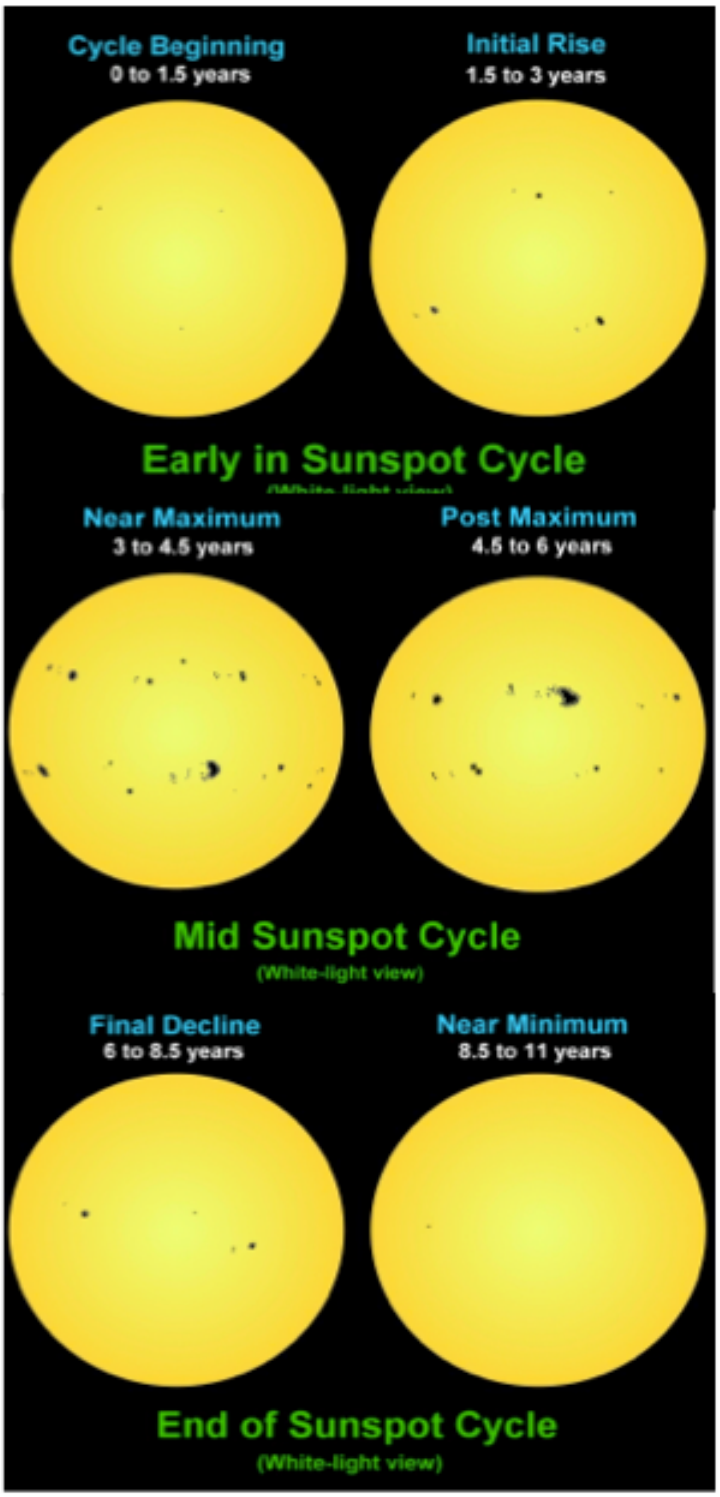

Figure 1.3: Sunspot Cycle (Credit: NOAA Space Environment Centre)

1.5 The Solar Dynamo

To understand the formation of sunspots and the existence of their related magnetic fields, it is necessary to investigate the various complicated plasma processes occurring within the Sun, which are not well understood. The absence of any way to directly probe the solar interior means that the internal dynamics of the Sun can only be inferred from a combination of theory and observations of the solar surface.

Larmor (1919) proposed the theory that motions of charged particles in the solar surface could create magnetic fields, just as currents flowing in ordinary wire. Physicist T. S. Cowling identified that there was a problem with Larmor's dynamo in that the fields could not sustain themselves for long, due of the resistance of the solar gases (Gough and McIntyre, 1998).

1.5.1 Magnetohydrodynamics

The combining of the equations of fluid mechanics with Maxwell's equations of electrodynamics led to the field of study known as magnetohydrodynamics (MHD). The foundations of MHD were laid in the first half of the twentieth century by scientists including Parker, Alfven, Cowling, Chandrasekhar and Elsasser.

1.5.2 Parker Solar Dynamo

Parker (1955) demonstrated that it was theoretically possible to generate reasonably permanent solar magnetic fields similar to those observed. The "Parker Solar Dynamo Theory" proposed that currents of charged particles in the convective outer layer of the Sun would generate magnetic fields. As these magnetic fields float to the surface, they would be twisted by the Coriolis force leading to the formation of surface sunspot-like magnetic regions as shown in Figure 1.4 *(d)*.

Over the course of a full sunspot cycle, these regions would merge to form the large-scale solar magnetic field, but with the opposite polarity to its former field. He proposed that this would be a cyclical process resembling the sunspot cycle while the actual period of the cycle could not, as yet, be predicted. This twisting was critical to the model since it helped to explain how the magnetic "polar field" changes from a poloidal to a toroidal field (Parker, 1955).

1.5.3 Babcock-Leighton Magnetic Dynamo Model

The 1960s saw the development of the Babcock-Leighton Magnetic Dynamo Model. According to Leighton (1964), the poloidal magnetic field of the Sun is a product of decay and the diffusion of large active regions associated with bipolar spot groups.

The model is based upon the premise that differential rotation, which occurs at the photosphere, causes the magnetic field distortions. It further assumes differential rotation is the cause of the process by which these field distortions become wrapped tighter and tighter. The Babcock-Leighton model goes on to propose the existence of a relationship between sunspot activity over the 11-year solar-cycle and the intensity of the large-scale axisymmetric magnetic field observed at the subsequent cycle minimum.

Observations show at the beginning of the cycle that sunspots tend to form at higher solar latitudes and then steadily migrate to the lower latitudes as it progresses. As the cycle continues the preceding members of a sunspot pair in each hemisphere are opposite in polarity, following a distinct pattern. If the polarity of the northern hemisphere is "north", then the polarity of the leading sunspot would be "south" and the alternative opposite true for the southern hemisphere. As the process continues, the magnetic field dissipates leading to the formation of a new global, opposite polarity magnetic field and the new cycle begins and when the polarity next changes then the twenty-two year solar cycle is complete (Babcock, 1961).

Solar differential rotation has been known and measured since the early seventeenth century; the Babcock-Leighton Model was the first to consider it as an explanation for the solar dynamo. Differential rotation is an important component in understanding the dynamo. It extends to the tachocline providing a shearing effect, which generates magnetic flux and helps enable a persistent magnetic cycle (Babcock, 1961).
In Figure 1.4, the field lines are shown twisting as they emerge from the photosphere. It is this twisting of field lines that leads to the formation of the sunspot cycle. Throughout the sunspot cycle, coronal loops cause partial dispersion of the magnetic field as the sunspots dissipate, and new ones migrate towards the equator (Freedman and Kaufmann, 2007).

This model certainly seemed to reproduce all of the observable features of the sunspot cycle, even down to the appearance of individual sunspot pairs. The model, however, could neither predict the length of the cycle nor explain the mechanism that created the initial surface magnetic field.

1.5.4 The Omega (ω) Effect

Magnetic fields within the Sun are stretched out and wound around the Sun by the mechanism of differential rotation or change in rotation speed as a function of both latitude and radius. Since the Sun does not rotate as a solid body, rotation occurs faster at the equator than at the poles. This differential rotation is a crucial ingredient for the dynamo action responsible for the conversion of the poloidal magnetic field to a toroidal magnetic field and leads to the effect as shown in Figure 1.4 *a, b, and c* (Hathaway, 2012).

1.5.5 The Alpha (α) Effect

Early models of the Sun's dynamo assumed the twisting resulted from the effects of solar rotation on the large convective flows carrying heat to the surface. More recent dynamo models have based their premises on the assumption that this twisting is due to the effect of the Sun's rotation on the rising "tubes" of magnetic field from deep within the Sun.

As a result of the inclination of active regions (where the leading spot of a bipolar pair is at a slightly lower latitude, also known as Joy's law), the following polarity has a slightly larger chance to migrate towards the nearest pole than the leading polarity This causes the magnetic field to reverse from one sunspot cycle to the next (Hale's law).

The twisting of the magnetic field lines as a direct result of Solar rotation causes the alpha-effect as shown in Figure 1.4 *d, e, and f.* Although an α–effect only exists if the star rotates, the precise mechanism that causes it is not yet understood (Love, 1999).

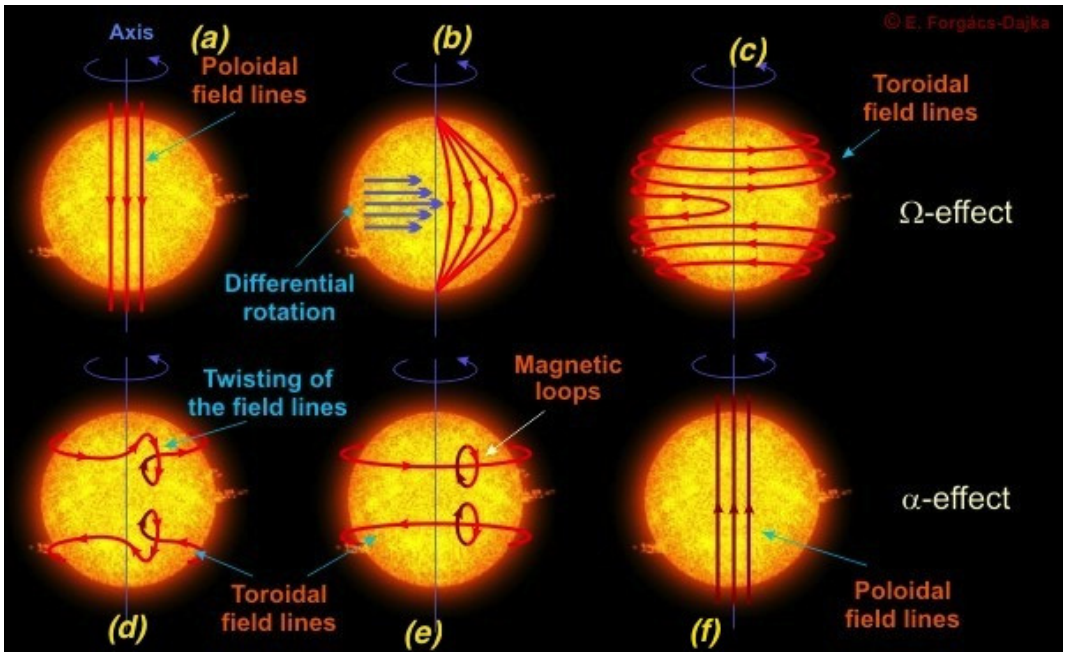

Figure 1.4: The Alpha–Omega Effect. Parts: *a, b, c* illustrate the Omega Effect and how the poloidal field is converted to a toroidal field. In parts *d,e,f* the Alpha Effect is shown as the toroidal field is converted into a poloidal one (Love, 1999).

1.5.6 The Interface Dynamo

Once it was known that magnetic fields within the convective zone would rise rapidly to the surface, it became obvious that there was insufficient time for either the α or ω effect to develop. Since a magnetic field exerts a pressure on its surroundings, regions within that field should push aside the surrounding gas, which would create a bubble that would then continue to rise all the way to the surface. This means that such an effect could not be produced in the stable layer below the convective zone. A magnetic bubble, which formed in the radiative zone, would not be able to rise far before it would become as dense as the surrounding matter. It was this realisation that led to the concept that the most likely place for the Sun's magnetic field to be produced was within the interface layer.

This layer forms an interface between the deep radiative zone that rotates at one speed and the overlying convective zone, which rotates differentially with a faster rate in the equatorial regions. The shear flows across this layer stretch magnetic field lines of force and make them stronger. It is this change in flow velocity that gives this layer the name tachocline (Hathaway, 2012).

1.6 Stellar Activity

The stellar equivalent of solar activity such as spots, flares, and activity cycles are present on a number of cool, rapidly rotating stars. The solar-stellar connection is the comparison of the Sun with other stars for improved understanding of solar and stellar physics, especially activity and dynamos. For cool stars like the Sun, dynamo action persists from the star's initial formation throughout its whole life cycle until the star ceases to generate nuclear fusion (Schrijver and Zwaan, 2003).

The Sun's internal dynamo depends upon the combination of both convection and rotation. In studying other stars, if their internal structure is similar to that of the Sun, it is, therefore, reasonable to expect similar dynamo processes occur and that they will demonstrate magnetic activity.

It appears that stars on the Main Sequence which are later than spectral type F0 and giants later than G0 have convective zones similar to the Sun. Observations show that some level of magnetic activity occurs in all cool stars, irrespective of their mass and radius (Saar, 1990).

Solar-type stars are defined as those with the same basic radiative and convective interior structure as the Sun based upon their mass. In contrast, it is known that stars with a mass greater than $1.3_{\odot}$ lack a convective zone; while stars, with a mass lower than $0.3_{\odot}$, are in theory entirely convective. Thus, solar-type stars range from mid F to mid K (Schrijver and Zwaan, 2003).

Throughout the lifetime of the Sun, it loses mass via the solar wind and similar effects and behaviour also occur on other stars. Conservation of angular momentum would imply that as a star expels its magnetically coupled wind, its rotation rate would slow and the star becomes less active (Baliunas and Vaughan, 1985) and so the younger rapidly rotating stars will be more active.

1.6.1 Starspots as Probes of the Stellar Dynamo

Like sunspots, starspots are the most easily observed form of magnetic activity on cool young stars and like sunspots they appear as cooler dark regions on the stellar surface (Biermann, 1938).

Kron (1947) first proposed the existence of starspots as an explanation for the irregularities seen in eclipsing binary light curves. Since then, there has been significant progress in the refining and development of techniques available to observe starspots and in understanding their physical properties.

Modern indirect imaging techniques such as Doppler Imaging (DI) when combined with high precision photometry, mean that it is now possible to measure the lifetimes, surface brightness, latitude distributions and local rotation rates of starspots as well as being able to track changes as the stellar magnetic cycle progresses.

Key parameters necessary in the investigation of stellar magnetic activity include the determination of spot configuration, temperature variation, and spot coverage. These are important to understanding the effectiveness of the dynamo production of the stellar magnetic field.

1.6.2 Observed Starspot Distributions

Starspots exist on a broad variety of stars across the Hertzsprung-Russell diagram. Rotational period appears to be the most significant parameter in the determination of starspot latitude while the fractional size of the radiative core also plays an essential role. Evolutionary stage and mass, previously considered important are now thought to play only secondary roles (Granzer, 2002).

There have been Doppler Imaging studies, enabling the measurement of starspot distributions undertaken on rapid rotators across the entire range of cool star spectral types (G, K and M dwarfs) (Donati and Landstreet, 2009).

Many rapidly rotating stars appear to have spots present across all latitudes leading to the possibility that compared to the Sun, there is a completely different mechanism responsible for generating some of the magnetic flux in these stars (Strassmeier, 2008).

1.6.3 Chromospheric Indicators

On the Sun, chromospheric plage regions produce Ca II H&K emission. When solar activity is at a maximum, there will be more plage regions on the solar surface meaning commensurately more Ca II H&K emission which makes it an ideal indicator. The search for a similar correlation in other stars initiated by Olin Wilson at the Mt. Wilson Observatory led to the initial discovery of stellar activity cycles. The project resulted in the long-term monitoring of 111 stars across spectral types F2 to M2. Many of these stars have observations covering over 30 years (Donahue *et al.*, 1995; Rodonò *et al.*, 1995).

The survey shows that there is a strong correlation between the presence of cyclic activity and stellar age. Younger rapidly rotating stars exhibit high levels of activity and rarely display a smooth cyclic variability, whereas, older, slowly rotating stars reveal lower activity and evidence of smooth cycles more analogous to the 11-year solar-cycle. Subsequent follow-up photometry undertaken for a subset of the Wilson survey stars showed that young stars become fainter at their activity maximum. This reduction in magnitude is in contrast to the Sun and other slower rotating stars which become brighter at their activity maximum (Lockwood *et al.*, 2007; Radick *et al.*, 1998). The implication of this is that the activity cycles on young stars are a result of brightness variations caused by dark spots rather than the emission from bright faculae.

1.7 Properties of Starspots

1.7.1 Temperature Variations

The determination of the spot configuration, temperature, and size is critical in understanding the role of the magnetic field in blocking the convective heating flux inside starspots. Spots are a key diagnostic in investigating stellar magnetic activity because they probe the production and the emergence of magnetic flux tubes from the dynamo. Starspots, usually have a temperature some 500–2,000 degrees cooler than the stellar photosphere (Berdyugina, 2005). This temperature variation causes a change in brightness of up to 0.6 magnitudes between the spot and the surrounding stellar surface. The observed relationship between spot and photospheric temperatures show that starspots behave the same regardless of their spectral type (O'Neal *et al.*, 1998).

Some DI studies incorporate the inversion of data type, spectroscopy, and photometry and so can provide the best-determined spot temperatures. Molecular absorption band spectroscopy utilising the TiO 7055Å and 8860Å features, in conjunction with DI and contemporaneous photometry, has been successful in measuring stellar spot surface area and temperatures (O'Neal *et al.*, 1998). Absolute spot temperatures are still difficult to obtain; differing results can be obtained when utilising the various stand-alone techniques. Through the combining of complementary observational techniques such as DI and photometry the most accurate and repeatable results are achieved.

1.7.2 Spot Sizes and Filling Factors

Spots, the size of those on the Sun, will be difficult to detect on other stars, due to the small variation in brightness produced. Active stars have large starspots, in some cases they appear to cover up to 20-30% of the stellar surface. This corresponds to spot sizes more than 100 times larger than those seen on the Sun (Berdyugina, 2002). The filling factor or the amount of the stellar surface covered by spots can be up to 50% in some cases. This has been found through the modelling of molecular bands observed in the spectra of spotted stars (O'Neal *et al.*, 1998).

The more rapidly rotating the star is the more sensitive DI will be to small-scale surface structure. Many stars show evidence of a large, dark polar spot. Vogt and Penrod (1983) recorded the first of these on the RS Canum Venaticorum (RS CVn) variable star HR1099.

The K0 giant RS CVn, XX Tri (HD12545), in Figure 1.5, has a gigantic starspot as seen in this Doppler Image displayed in a spherical projection with surface temperature as labeled to the side. This spot is about 10,000 times larger than any seen on the Sun and has a spot temperature cooler by 1,300±120K with respect to the undisturbed photosphere.

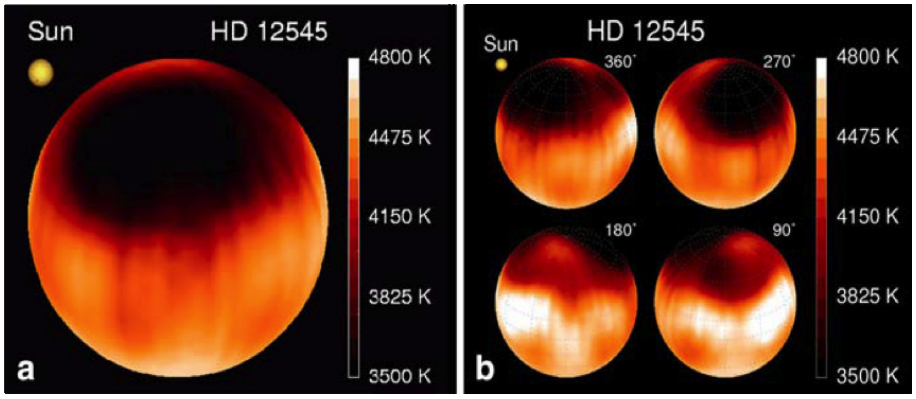

Figure 1.5: The gigantic starspot on the K0 giant star XX Triangulum (HD12545) is shown here in Image *a* alongside a white light image of the Sun with the largest sunspot ever recorded shown for the purpose of comparison. Image *b* shows the same Doppler Image but at four different rotational phases (Strassmeier, 1999).

Measurement of total spot coverage is a critical measurement, and while direct techniques can provide estimates, indirect measurements have sometimes been considered controversial due to their dependence upon the techniques and assumptions used (Strassmeier *et al.*, 1999).

Differing definitions between methodologies and groups exist in relation to both spot size and area. With sunspots, it is simple to determine where one spot ends and another starts as there is a very sharp contrast. When using DI to measure starspots, the images appear much smoother and are of poorer resolution. Since spots are most likely constantly changing, just like sunspots, different mapping techniques would need to be applied to the same star simultaneously to allow for meaningful technical comparisons.

1.7.3 Lifetimes of Spots

The lifetime of a starspot is dependent upon its size. While, in the case of smaller starspots, their lifetime is directly proportional to their size; the lifetime of larger spots appears to be more dependent upon the presence and strength of the stellar differential rotation rate. There are indications that larger spots, assumed to be the cause of significant photometric light variations, survive many years (Hall and Henry, 1994) while smaller spots are more like sunspots surviving only for a few hours to days.

As an example, the weak line T-Tauri star, V410 Tau, has a large polar spot that appears to have survived for at least 20 years. Later Doppler Images suggest that the large polar region may consist of many large spot groups with as yet unidentified life times (Berdyugina, 2005; Hatzes, 1995).

A detailed view by Hussain (2002) suggested that spots on tidally locked binary systems last months longer than spots on single main-sequence stars. Spots on the single stars appear to last for only a few weeks. Hussain (2002) also suggested the large polar spots were most likely formed through a different mechanism, for example, magnetic flux swept up to the rotational poles from lower latitudes by strong poleward meridional flows.

Lower latitude spot lifetimes observed from time-series photometry appear to be about one year. The presence of active longitude "flip flops" may lead to the termination of the imprint of the spot or a group of spots on the light curve. This can mask the cause of the usual decay mechanism (Hussain, 2002).

Strassmeier and Hall (1994) traced 20 individual spots or spot groups on the spotted RS CVn binary HR7275, and found individual spot lifetimes of up to 4.5 years with an average lifetime of 2.2 years and used these observations to set an upper limit to the differential surface rotation of five to eight times less than that of the Sun.

1.7.4 Polar Spots

In recorded history, there has been no evidence of sunspots at high latitudes or near the poles of the Sun. This fact has previously raised doubts regarding the reality of polar spots on other stars (Schrijver and Title, 2001). However, the application of a number of different image reconstruction techniques by independent groups along with extensive testing of the algorithms has provided significant evidence in favour of their existence (Strassmeier, 2001).

Doppler Imaging allows direct recovery of spot latitudes. Starspots at high latitudes, or even covering the stellar rotational poles, are common among the most active of the cool stars. The overview by Strassmeier (2008) shows that of the 79 stars and stellar systems for which Doppler Images were available in 2008, a total of 70% appear to have polar spots. Some targets have both polar and equatorial spots. Since Strassmeier's review, there have been an increased number of Doppler Images obtained for more stars confirming these percentages. There does not appear to be any clear correlation between the occurrence of polar or high latitude starspots and selected group of stars studied. The only thing that the stars with polar spots appear to have in common is that they are all rapid rotators. This may however, be due to an observational bias within the technique and selection methodology since DI may only be successfully applied to rapid rotators.

Schüssler *et al.* (1999) made the suggestion that high-latitude starspots in rapidly rotating stars could be the consequence of a strong Coriolis force acting on magnetic flux bundles rising from deep within the star. Now it is considered that the immense polar spots cause a change in the structure of the stellar winds.

On the Sun, the dense and slower solar wind is created above the low latitude active regions, which have closed magnetic field lines while the faster solar wind originates predominantly at the high-latitude coronal holes with their open field lines. If the presence of the large polar spots forced the slower stellar wind to flow from the polar-regions, it would then cause them to flow along and almost parallel to the rotation axis potentially affecting magnetic braking of stellar rotation in the early stages of the star's evolution (Zaqarashvili *et al.*, 2011).

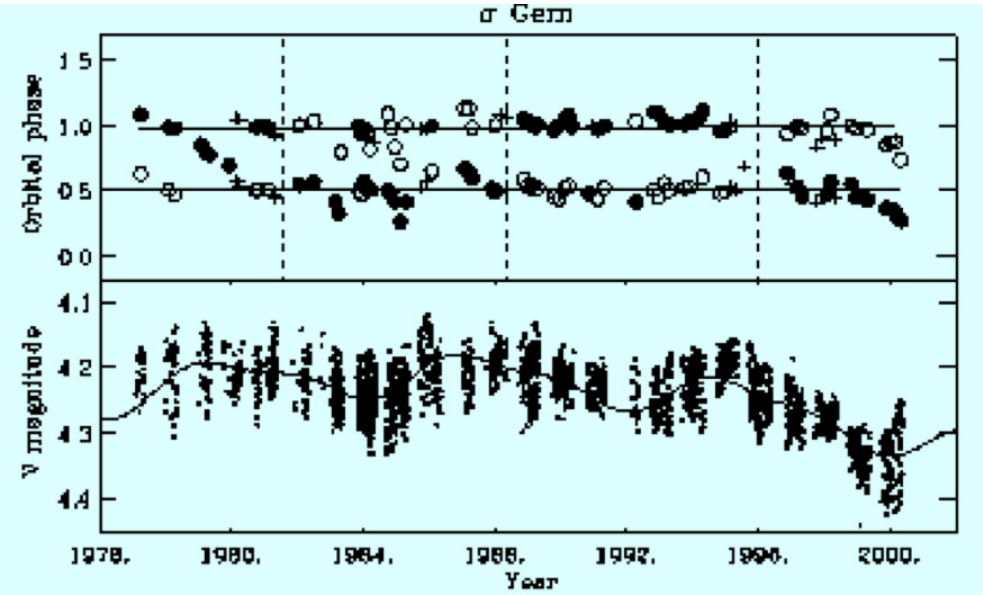

Figure 1.6: Active longitudes, flip-flops and sunspot-like cycles on the RS CVn star σGem (Berdyugina and Tuominen, 1998).

1.7.5 Active Longitudes

After many years of photometrically monitoring RS CVn stars, large spots appear to maintain their identities for several years (Zeilik *et al.*, 1988). This was interpreted as a signature of one or two active longitudes similar to the distribution of solar energetic flares (Berdyugina and Tuominen, 1998).

Figure 1.6 shows active longitudes, flip-flops and sunspot-like cycles on the RS CVn star σGem. The upper panel shows phases of major spot concentrations with the filled and open circles denoting primary and secondary regions, respectively. The solid lines emphasise the migration paths of the active longitudes while the vertical dashed lines mark flip-flop jumps to the opposite active longitude. The lower panel shows variations of the stellar brightness, which reflects variations of the spot area (Berdyugina and Tuominen, 1998).

In most cases observed so far, the active longitudes on RS CVn stars tend to be permanent and separated on average by 180°. However these active longitudes permanently migrate within the orbital reference frame most likely due to differential rotation.

This behaviour occurs on the Sun and appears to be typical for single stars, young solar type dwarfs, and FK Com-type giants studied to date (Berdyugina and Usoskin, 2003).

The migration of active longitudes through changes in the mean latitude where the spots form and also as a result of differential rotation. On the Sun, spots first form at higher latitudes approaching closer to the equator as the solar cycle advances. Migration towards the equator is faster at the start of the new cycle and while being slower towards the cycle-end. This migration pattern of the active longitudes provides information on both differential rotation and mean spot latitudes. It can be used to infer the stellar differential rotation and butterfly diagrams.

1.7.6 Differential Rotation

Differential rotation, where the equator of the star rotates at a faster rate than at the poles, plays an essential role in the generation of magnetic fields in the convective zone. Differential rotation of the Sun is a key factor in theories of magnetic-field generation and is thought to be the dominant process by which poloidal to toroidal field conversion occurs. Solar differential rotation causes the weaker large-scale poloidal field to be transformed into a stronger toroidal component(Berdyugina, 2005).

Solar differential rotation is readily observed in the relative motion of sunspots. However, on other stars such characteristics can only be determined from indirect observations. One method is the cross-correlation of successive Doppler Images; a technique first performed by Donati and Collier-Cameron (1997) for the active young dwarf AB Doradus. Different studies have revealed that there exists a solar type surface differential rotation on AB Doradus, with the equator rotating faster than the polar regions (Barnes *et al.*, 2000).

The parameter fit method utilising DI or Zeeman Doppler Imaging (ZDI) was developed by Donati *et al.* (2000) and Petit *et al.* (2002). When applied to a small sample of active G2 and M2 dwarfs it was found that all stars targeted demonstrated the presence of solar type differential rotation. This work also showed that there exists a relationship between spectral class and rotational shear (Barnes *et al.*, 2005; Petit *et al.*, 2004). For M dwarfs, differential rotation has been found to be almost negligible while for G dwarfs it was far stronger and varied significantly from that seen on the Sun. Observed differential rotation varied from predictions for cool spots or magnetic regions with what appear to be temporal fluctuations on time-scales of one to a few years (Donati *et al.*, 2003a).

1.8 Discussion

Studying numbers of cool young stars will lead to a better understanding of how the dynamo works through understanding the generation and behaviour of magnetic fields in different circumstances.

The Sun is only one example, and from an observational point of view it does not provide sufficient constraints in relation to theories of stellar dynamos. Consequently, it is essential for other stars to be observed in order to establish how mass, rotation, brightness, and age affect the patterns of stellar activity and the underlying dynamo.

Stellar spot studies can help answer questions such as:
What determines cycle strength and duration?

How common is solar-type activity?

Can multiple cycles exist at the surface? and

How do polar spots form?

Starspots are created by local magnetic fields on the surfaces of stars, just as sunspots are on the Sun. Their fields are strong enough to suppress the overturning convective motion, blocking or redirecting the flow of energy from the stellar interior outwards to the surface. They then appear as locally cool, darker regions against an otherwise bright photosphere (Biermann, 1938, 1948). As such, starspots are observable tracers of the still as yet unknown internal processes. Understanding starspots, their surface location and migration pattern and what they reveal about stellar dynamos are important for understanding low-mass stellar formation and evolution.

Given the scientific value of Doppler Imaging for stellar dynamo surveys this thesis sets out to establish the suitability of the ANU 2.3-metre telescope as a facility for ongoing DI studies. As a 2-metre class telescope with an echelle spectrograph, the instrument should provide a useful survey tool for these studies as long as suitable targets can be identified and DI can be performed successfully using such a facility.

To ensure that DI at the 2.3-m would have a suitable target list of southern active rapidly rotating solar-type stars a survey of around 200 southern stars was selected from the HIPPARCOS catalogue (Koen and Eyer, 2002). This survey was undertaken and work is continuing with the data and the results planned to be published as a separate survey paper.

Chapter 2

Doppler Imaging

2.1 Introduction

The Doppler Imaging (DI) technique is one of the most effective methods for observational studies of stellar activity. As a result of the Doppler effect, the spectral contributions of different surface zones are shifted in wavelength and surface spots reveal themselves as bumps, moving across line profiles as the star rotates. Each Doppler-broadened line profile represents a one dimensional projection of the stellar surface so that observing the star from different aspect angles makes it possible to reconstruct a map of surface structure (Kochukhov *et al.*, 2004).

Doppler Imaging has its foundations in the concept of the “oblique rotator" first suggested by Deutsch (1958). Deutsch used this concept to explain the periodic and persistent variations of spectral line strength in chemically peculiar (CP) stars. The “oblique rotator" model assumes chemical elements are concentrated in specific areas spread over the whole the stellar surface and that it is stellar rotation that causes the variability (Piskunov, 2008). DI exploits the correspondence between wavelength position across a rotationally broadened spectral line and spatial position across the stellar disk to reconstruct surface maps of rotating stars (Vogt and Penrod, 1983). The technique has continued to be perfected and refined using improved observations and increased computing power and has been used to reconstruct temperature maps of cool stars (Strassmeier, 2002) and abundance maps of hotter stars (Kochukhov *et al.*, 2004).

2.2 General Principles of Doppler Imaging

Since Deutsch (1958) first formulated this idea, Goncharskii *et al.* (1977b) and Schüssler and Solanki (1992) developed the first inversion technique with minimisation. DI has since been employed widely for studying starspots on many active stars. The technique utilises high-resolution spectral line profiles of rapidly rotating stars for mapping the stellar surface.

Originally used for the mapping of chemical peculiarities on the surface of Ap stars, it has since been used to determine, through the modelling of photometric variations in late-type active stars, that starspots could potentially cover up to 50% of the stellar surface, resulting in noticeable line profile variations. In 1983, Vogt and Penrod obtained the first Doppler Image of a spotted star, after profile variations were first observed in the spectra of the RS CVn star HR1099 (Vogt and Penrod, 1983).

DI allows starspots to be studied in detail. Several stars have now been observed over many years making it possible to study starspot evolution over time. Through DI, it is possible to identify the broad latitude range over which starspots occur as opposed to the limited latitude range on the Sun. Starspots are frequently seen at very high latitudes, 50-65° away from the equator and even on the poles. DI has identified that the size of spots and/or spot groups on other stars are significantly larger than those on the Sun. Currently, there is insufficient resolution to differentiate whether the huge polar spots, found on many young stars, are large single spots or groupings of smaller spots.

On the Sun, the lifetime of spots can be measured in the order of days or at most weeks. On other stars, however, some spots appear to remain in the same general location for several years. This, of course, does not necessarily mean that the same spot remains in one position all the time, but rather that there appears to be constant spot activity in the same area.

The DI technique has two major limitations, firstly the assumption that the studied field is not evolving, and secondly accurate temperatures of the magnetic regions are not usually known. The first assumption is questionable given the high level of activity and rate of flaring of these stars. Little information on characteristic timescales and evolution patterns is available on these active young stars. Secondly, although temperatures of stellar active regions are poorly known in stars other than the Sun, regions of higher or lower temperature add more or less flux to the observed spectra than the quieter solar photosphere and so the differential can be calculated.

DI allows a map of irregularities or variations of the stellar surface to be obtained by utilising the correspondence between wavelength positions across a rotationally broadened spectral line as well as the spatial position (Strassmeier, 2008). It is an inversion technique to reconstruct 2-dimensional, latitude and longitude, images from a time series of 1-dimensional spectral line profiles taken at different rotational phases. The technique is based upon the Doppler effect discovered by mathematician and physicist, Christian Doppler in 1842 (Gray, 1992).

In the non-relativistic limit, the absolute value of the Doppler shift, $|\delta|$ for the wavelength λ can be found by using the equation:

$$\frac{|\Delta\lambda_0|}{\lambda} = \frac{\nu_r}{\nu_w} \tag{2.1}$$

where: λ_0 is the rest wavelength, which the star emits when it has no radial velocity;
ν_w is the velocity of the wave, for example the speed of sound or the speed of light (in this case $\nu_w = c$, where c is the speed of light); and
$\nu_r \ll c$ is the radial velocity of the source with respect to the observer.
The sign for the Doppler shift $\Delta\lambda_0$ is dependant upon the direction of the radial velocity ν_r of the source.

DI currently remains the only way to obtain information on both the latitude and longitudinal distribution of spots on stars other than the Sun. The position of the deformation of the line profile shows the latitude of the spot. The information from the line profiles can then be reconstructed by a mathematical inversion technique to enable a picture of the stellar surface to be created. One complete stellar rotation is necessary to gather the requisite information.

Figure 2.1 demonstrates the principles of Doppler Imaging. As the star rotates, the spots are carried across the disk of the star, which causes a change in the Doppler shifts of the bumps in relation to their projected distances from the star's rotation axis. The portion of the rotation cycle that a spot is visible depends upon its latitude as well as the inclination of the stellar rotation axis to the line of sight.

By noting the times at which the spot signature crosses the centre of the line profile enables the collecting of latitude information and the longitude of the spot can be identified by measuring the amplitude of the profile (Collier-Cameron, 2000).

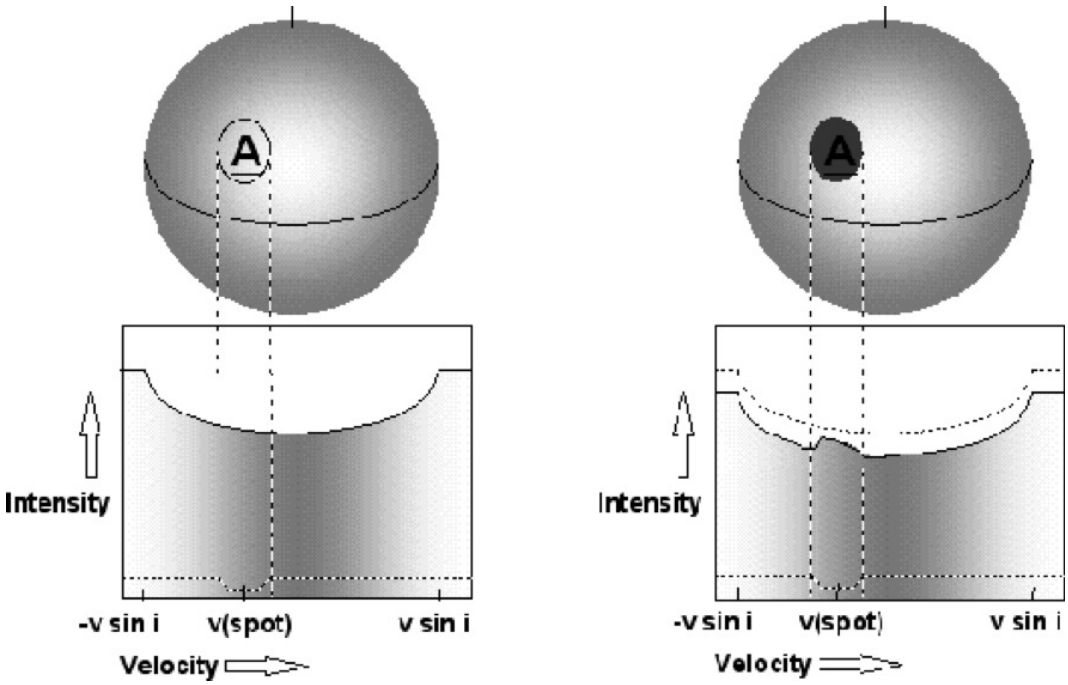

Figure 2.1: How Doppler Imaging Works - The "missing" light of the spot consists of a continuum contribution that spans the line profile, plus a narrow line contribution that is Doppler shifted by an amount that depends on the projected distance of the spot from the stellar rotation axis. Removing this light causes an overall depression of the continuum, but less light is removed at the Doppler shift of the spot relative to the centre of the line. The observable signature of a dark spot on the stellar surface is therefore a bright bump in every photospheric absorption line in the star's spectrum (Collier-Cameron, 2000).

Spots near the stellar equator produce a distortion, which is only visible for half the rotational cycle of the star, moving over time from the extreme blue wing of the line profile to the extreme red. Higher latitude spots produce distortions that may be visible at all times and that migrate back and forth near the line centre as the star rotates, if the star is inclined. The radial velocity at which the distortion is observed is defined by the position of the cool spot, while its size is proportional to the size of the spot.

A time series of the temperature-sensitive atomic line profiles observed over a full stellar rotation contain information about the spot distribution on the stellar surface. This distribution can then be inferred using an inversion technique resulting in a map, or image, of the stellar surface (Berdyugina, 2002).

2.3 Basic Techniques of Doppler Imaging

The foundation of DI is the distinctive manner in which spots at varying locations on the surface of the star produce deviations from the ideal rotationally broadened line profile. Piskunov and Rice (1993) undertook a review of some of the DI techniques in use up to that time. The evolution of DI techniques commenced from the initial use of analytical shapes for local line profiles, such as the Minnaert profile used with minimisation through conjugate gradients (Goncharskii *et al.*, 1977a). The use of a fixed empirical local line profile was then used as an alternative to using analytical expressions for the line shapes and this allowed for a linearised forward calculation (Vogt *et al.*, 1987).

Subsequent techniques have replaced the analytical or empirical local line profiles with profiles calculated from model atmospheres appropriate to the local conditions on the image. Calculating the line profiles for every element of the surface for each iteration of the conjugate gradient minimisation routine would demand an inordinate amount of computing time so the profile calculations are tabled for an array of limb angles and temperatures as outlined in Piskunov and Rice (1993).

2.4 Requirements for Doppler Imaging

To create accurate and good-quality Doppler maps, there are a number of important prerequisites. DI requires absorption lines with a signal to noise ratio (SNR) of a few hundred per pixel to have the best opportunity to obtain an accurate useful image. Exposure times must be minimised to reduce the effects of rotational blurring. These limitations constrain the types of stars which would make suitable targets for DI studies. This has led to a bias towards brighter targets of magnitude 8 or less and greater representation of early K giants due to their higher luminosities.

The stars selected to be used as proof of concept stars for this thesis were the bright, well studied K0 dwarf AB Doradus (AB Dor) at magnitude 6.99 and the G1V star HIP43720 at magnitude 9.11. The previously well-studied AB Dor is bright with a high rotational velocity, ≈0.51 day period. HIP43720 is more challenging at magnitude 9.1, has only a moderate rotational velocity of 39 km s^{-1} and a period of ≈3.2 days (Waite *et al.*, 2011).

2.4.1 Accurate Stellar Parameters

Stellar parameters, relevant to DI, include temperature, radius, inclination, rotational velocity, rotational period and orbital parameters where relevant (Washuettl *et al.*, 2008). Many of these parameters may not be known precisely, and this could introduce errors into reconstructions. First of all, a reliable photometric period and the radial velocity shifts of all the spectra, which are to be used for the DI have to be determined. This can be difficult in longer-period targets as it can take several nights to months to obtain a complete period measurement.

Use of incorrect input parameters can mean that features such as large polar spots and wide latitudinal belts can be obtained when using incorrect values of the stellar rotational velocity or effective temperature of the star (Berdyugina and Tuominen, 1998). Spot latitudes, for example, are strongly dependent upon the inclination angle of the rotational axis to the line of sight. Various tests have shown that there are limitations as to the capability of the technique relating to spot recovery in the equatorial region where recovered spots may have reduced area and contrast. Sub-equatorial spots cannot be restored, especially at lower inclinations (Berdyugina, 2005).

The sensitivity of Doppler Image reconstructions can be tested through the creation of synthetic data from a given image, introducing some noise and reconstructing an image from the synthetic data with changed parameters and doing a comparison with the actual image to see how well the different features have been reconstructed and where artefacts have appeared or suspected features disappeared.

2.4.2 Projected Rotational Velocity - $v\sin i$

Piskunov *et al.* (1990) discussed the issue of minimal spectral resolution or minimum $v\sin i$ for useful DI. These authors considered resolutions ranging from 20,000 to 50,000 and a $v\sin i$ between 15 and 30 km s^{-1}. At the lowest spectral resolution and with a $v\sin i$ of 30 km s^{-1}, they could still accomplish a reasonable recovery of coarse features. This could also be achieved with the highest resolution and a much lower $v\sin i$ of 15 km s^{-1}.

Although, in much of their work, these authors focus on Ap star mapping, the guidelines they put forward are still reasonable for cool star work, where the non-polar spot features are not as coarse.

In cool star DI, the stars EK Dra and AG Dor have both been able to be mapped on a number of occasions even though they have rotational velocities of 17 and 18 km s^{-1} respectively (Järvinen *et al.*, 2007; Rice, 2002; Washuettl *et al.*, 2001). A minimum $v\sin i$ of ∼20 km s^{-1} which corresponds to a half-width of the spectral line of 0.4 and a resolution of eight surface elements at a spectral resolution of 0.1 (64,000) is a suitable $v\sin i$ limit for most telescope/instrument setups.

However, as further discussed by (Piskunov *et al.*, 1990), what the minimum $v\sin i$ is for an individual telescope/spectrograph depends on the spectral resolution of the instrument used. Recent studies of CoRoT data have enabled the surface mapping of stars with a $v\sin i$ of around 10 km s^{-1} (Mathur *et al.*, 2011).

Figure 2.2 shows the LSD profiles of three stars observed as a part of the Doppler Imaging Candidate Survey undertaken with the ANU 2.3-metre telescope. They have differing $v\sin i$ measurements of ≈100, 55 and ≤20 km s^{-1} respectively. The line deformation, which could indicate spot activity on the two faster rotators is clearly evident. These two targets could most likely be suitable for DI on the 2.3-m telescope. Surface features on the slower rotating star could not currently be resolved. Stars like the Sun, both in age and activity would be unsuitable candidates for this methodology using current technology. This introduces a bias in target selection towards stars which are young or have high rotational velocities.

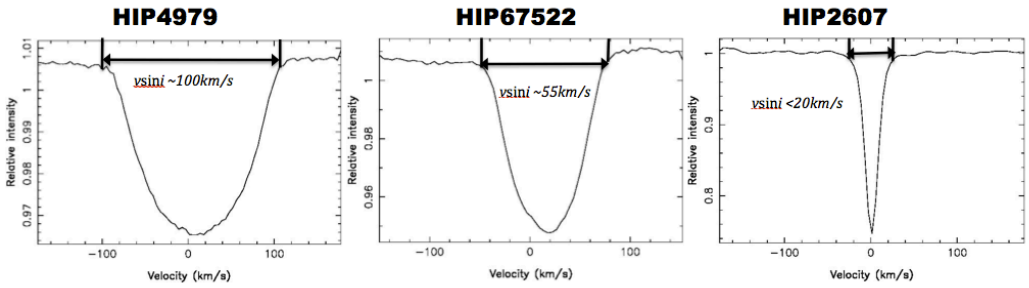

.

Figure 2.2: Examples of LSD profiles. These are for three of the survey targets, each of which have a different rotational velocity $v\sin i$. HIP4979 ≈ 100 km s^{-1}, HIP67522 ≈ 55 km s^{-1}, and HIP2607 ≤ 20 km s^{-1}

It is essential that any broadening of spectral lines is predominantly due to stellar rotation. If the stars rotational velocity is too low, degraded spatial resolution results. When rotational velocities are too high, the resulting spectral lines can be too broad making identification of spots difficult. Most stars are not viewed straight on, but rather, their axis are inclined either toward or away from the Earth. This is known as the star's inclination angle i, the true rotational velocity has to be higher by the factor $1/\sin i$, which adds 15% to the velocity if i is 60°.

2.4.3 Rotation Period and Phase Coverage

An important aspect of the evolution of cool stars is stellar rotation. Dark spots are being carried across the stellar disk by the stellar rotation modulating the total brightness with the rotational period of the star, allowing the determination of stellar rotation periods with high precision. This allows an accurate measurement of rotation rates with respect to spectroscopic measurements as they are independent of the unknown inclination of the rotational axis (Barnes *et al.*, 2001).

2.4.3.1 Rotation Period

To be a suitable candidate for DI, a star needs a high rotational velocity or more precisely, a high $v\sin i$. This ensures that rotational broadening is the main line broadening mechanism. In a first approximation, the number of elements that could be resolved on the stellar surface is approximately:

$$\frac{2vsini}{W} \tag{2.2}$$

where: $v\sin i$ is the projected rotational velocity; and
W is the full width of the line profile at its half-maximum in case of no rotation.

Typically, $W \approx 10$ km s^{-1} for spotted cool stars, which puts a limit of about 20–30 km s^{-1} on the projected rotational velocity ($v\sin i$) of the star.

Deriving rotation periods is not a trivial exercise. Constructing light curves is labour-intensive involving observations spread out over several days, weeks or months to obtain sufficient coverage. This leads to a bias in DI studies towards stars which are rapid or ultra-rapid rotators as they have the shortest rotational periods.

Young stars are believed to be more active, and a significantly larger percentage of them have detectable photometric variations, which results in a bias towards active young stars. An accurate rotational period is essential to determine the stellar phases necessary for the precise mapping of spot features.

The portion of the rotation cycle that a spot is visible depends upon its latitude as well as the inclination of the stellar rotation axis to the line of sight.

To calculate the stellar inclination angle i to the observer's line of sight use:

$$\sin i = \frac{P.vsini}{2\pi R} \tag{2.3}$$

Where: i is the inclination angle;
P is the rotational period;
$v\sin i$ is the rotational velocity; and
R is the stellar radius.

However, even though DI is sensitive to the stellar inclination, errors of the order of $\pm 10^{\circ}$ can still yield acceptable reconstructions.

In Table 2.1 a summary of what makes a star suitable for DI is given, together with appropriate observational conditions for stellar surface reconstruction.

Table 2.1: Summary of Doppler Imaging Requirements

Observations	
Phase coverage	$>$ 6 observed spectra
Spectral resolution, $\lambda/\Delta\lambda$	$\geq$30 000
SNR	$\geq$100
Observational period	$<$ 2$-$3 months
Input geometrical parameters of the star	
Projected velocity, $v\sin i$.	20–100 km s^{-1}
Inclination, i	20°–70°
Rotational period	$\neq$n days and $<$2 month

2.4.4 Other Important Input Parameters

Doppler Imaging is a robust and well-accepted technique, but it is essential in order to obtain the highest quality and accurate Doppler Image maps that the inputs are correct. Incorrect or inaccurate inputs such as fundamental stellar parameters, stellar atmosphere models and atomic and molecular line lists can significantly affect the resulting DI map (Berdyugina, 2005; Unruh and Collier-Cameron, 1995).

Although very small variations may not be critical in simple DI maps, accuracy is crucial when differential rotation measurements are attempted.

The line lists used in the data reduction process of this thesis are the line lists generated by J-F Donati from Kurucz (1993). The deconvolution process used by the software is fairly robust with respect to choice of line list spectral type. The later the stellar spectral type to be deconvolved, the greater the number of photospheric absorption lines are available. However, using a line list of significantly later spectral type than the objects being observed is not a good idea, since, in the actual spectrum, there may only be continuum where in the line list a synthetic line exists.

For a K0 dwarf, such as AB Dor, using a K5V line list, which has about 600 more lines than the correct K0 line list, will certainly give a greater signal to noise value. However, because line patterns, which do not exist, will be, therefore, included in the least squares calculation as well the possibility of adding continuum if a line occurs in the list but is not present in the observed spectrum. Similarly, using a line list of earlier spectral type, with too few lines, will also result in incorrect treatment of the line pattern and a reduce signal to noise value.

Some of the necessary stellar parameters, if unknown, may need to be determined by trial and error as part of the Doppler Imaging process itself (Collier-Cameron *et al.*, 2002). These include the stellar inclination angle and spot temperature distribution. Parameters such as stellar rotation and photospheric parameters need to be known in advance. Therefore, care and attention must be paid when calculating, identifying and inputting these parameters to ensure a good quality image rather than one which could be contaminated by artefacts.

2.5 Discussion

Although there are a number of methods available to study young solar analogues, their starspots and related stellar activity, it is apparent that the method of Doppler Imaging offers the most effective method to observe the surface activity of young solar-type stars and so advance understanding of the history of the solar dynamo and its cycles.

In Australia, there are currently only two echelle spectrographs available for cool star studies. The first of these instruments is the University College London Echelle Spectrograph (UCLES) on the AAT at Siding Spring Observatory. UCLES has been used for both DI and (with the addition of the SEMPOL polarimeter) ZDI studies of a number of active young solar analogues over the past 25 years. However, the reality of observational astronomy is that the amount of time available on the AAT compared with the number and size of projects seeking telescope access makes major ongoing DI surveys with this telescope an unlikely option. As time for long-term projects is difficult to come by on a 4-metre class telescope and by its nature Doppler Imaging requires many nights over many epochs for even a single star to obtain any depth of information, an alternative approach is needed. This thesis, therefore, focuses on the second instrument available in Australia, namely the high-resolution echelle on the ANU 2.3-metre telescope also located at Siding Spring Observatory.

Chapter 3

Instrumentation, Observations and Analysis

3.1 Introduction

High-resolution spectroscopy was undertaken with the Australian National University (ANU) 2.3-metre telescope at Siding Spring Observatory (SSO) near Coonabarabran in New South Wales, Australia between December 2008 and January 2013. Doppler Imaging (DI) and Zeeman Doppler Imaging (ZDI) has been carried out with the Anglo-Australian Telescope for the past 25 years using the visiting instrument SEMPOL for ZDI and UCLES for DI.

3.2 Instrumentation

3.2.1 The Telescope - ANU 2.3-metre Telescope at Siding Spring Observatory (SSO)

Initial DI observations for this project were carried out using the high-resolution 79 grooves/mm echelle (R2) spectrograph mounted at the Nasmyth–B focus of the ANU 2.3-m telescope at SSO. (Figure 3.1) Used in the f/18 configuration the telescope has a field of view of 6.62'. (Figure 3.2)

In 2009, the telescope and control software were upgraded in to enable remote operation.

Echelle spectroscopy is traditionally used to observe single objects at high spectral detail. The spectrum is then mapped using a cross-disperser to a 2-dimensional array onto the detector providing large wavelength coverage.

Figure 3.1: ANU 2.3-metre Advanced Technology Telescope at Siding Spring Observatory.

The power of an echelle lies in its high efficiency, and low polarisation effects over large spectral intervals and this leads to compact, high-resolution instruments. (Figures 3.3 and 3.4)

The camera was designed so that the dispersion of the spectrograph is wavelength/1000 in Å/mm so that at 4000Å, it is 4Å/mm and at 6500Å, it is 6.5Å/mm. The camera itself is f/2 and the spectrograph f/10.

Due to the positioning of the camera, dewar and the liquid nitrogen auto filler the instrument itself is unable to be rotated.

There is a choice of two cut-off filters (GG13 and GG495) that remove the light below 3900Å and 5000Å respectively to stop second order blue light from overlapping the first order red observations. No filter, however, was needed for these observations.

3.2.2 High Resolution Echelle Spectrograph

Since adjustments to the spectrograph need to be done manually, remote observing with the echelle instrument, is only possible provided the instrument can be set up by the technical or support staff. The provision of a wavelength calibration arc image from the previous run assists in this process. All observing for this project was on site. The observer undertook the setup for each of the observing runs to match it as close as possible to previous setups.

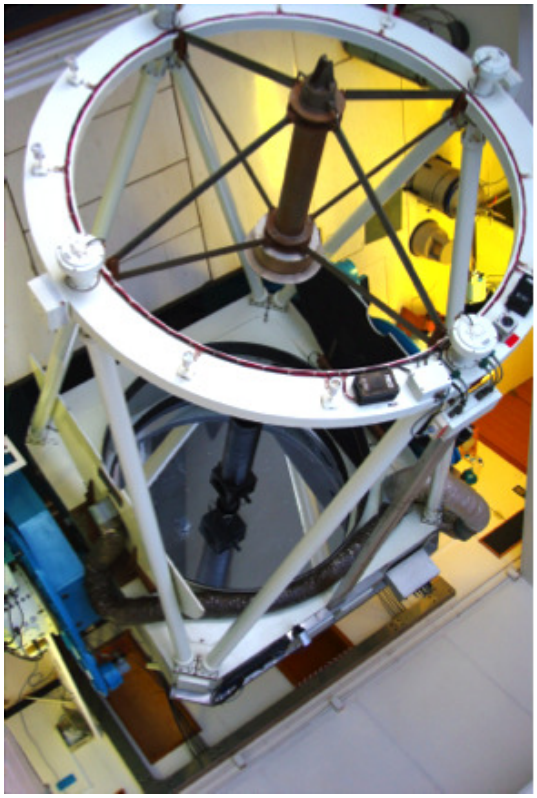

Figure 3.2: 2.3-m telescope with mirror cover open. Echelle spectrograph is located at Nasmyth focal station B on left of photo.

3.2.2.1 Slit Unit

The slit unit is located near the front of the spectrograph on the camera side. Adjusting the slit width itself requires carefully removing the slit unit from the spectrograph and adjusting the micrometer. The unit needs to be removed and replaced very carefully to avoid damaging the optical components that in practice, means that it is rarely adjusted.

The slit rotation and dekker width are easily adjusted from the outside of the instrument. The maximum decker width is a setting of 1 for 7000 . The dekker, which is adjustable via a central knob on the slit unit, is used to limit the length of the slit as well as to allow slit rotation. '0' is the maximum and '20' the minimum length. The slit rotation is adjusted with the outer knob. A dekker setting of 13 was found to give the best results with the 316/7500Å cross disperser set to observe orders 57 to 34.

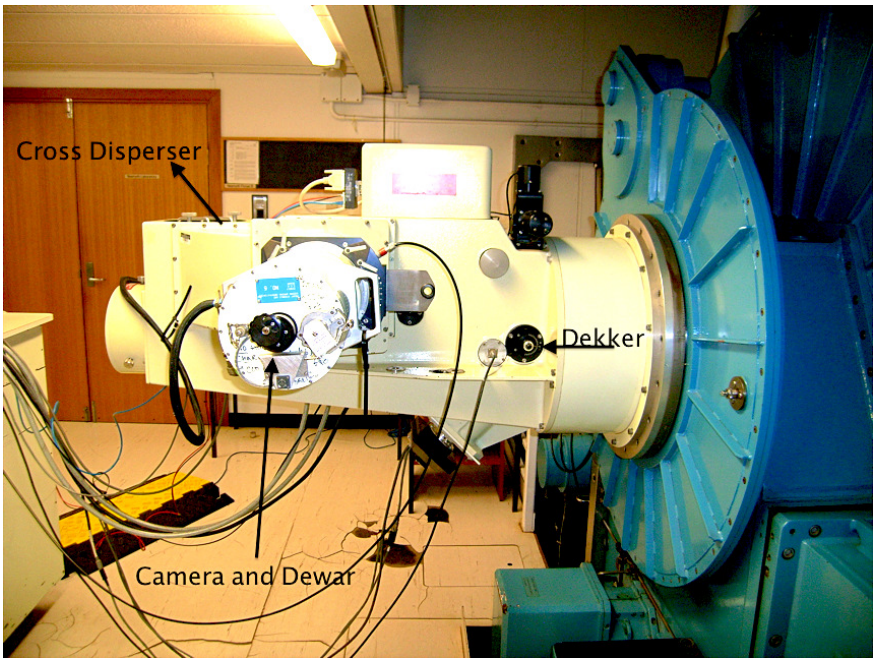

Figure 3.3: The Echelle Spectrograph viewed facing the camera dewar spectrograph with various components labelled.

3.2.2.2 Camera

The camera contains a 2K x 2K E2V CCD with 13.5μm x 13.5μm pixels. The gain is two electrons per Analog-to-Digital Unit (ADU) resulting in a read noise of approximately 2.3 ADU for each pixel. An ADU is a measurement of pixel value or brightness.

There is a field flattener attached to the front surface of the CCD dewar window for the echelle which has reduced most aberrations so that the whole 2K x 2K of the CCD can now be used. It does, however, introduce some spherical aberration across the field, which results in some small residual curvature in the focal plane. The result being that the arc lines toward the edge of the field are asymmetrical as is evident in Figure 3.5. The central resolution is 3 pixels extending out 5.5 pixels at the edge of the chip.

The camera is focused by moving the collimator after loosening two screw clamps on the collimator mirror located at the end of the instrument away from the telescope. There is a knob to turn the collimator drive and a dial gauge, which reads the position. However, the spectrograph focus is particularly robust and insensitive to temperature meaning it also is rarely if ever adjusted. The CCD does have relatively good cosmetics.

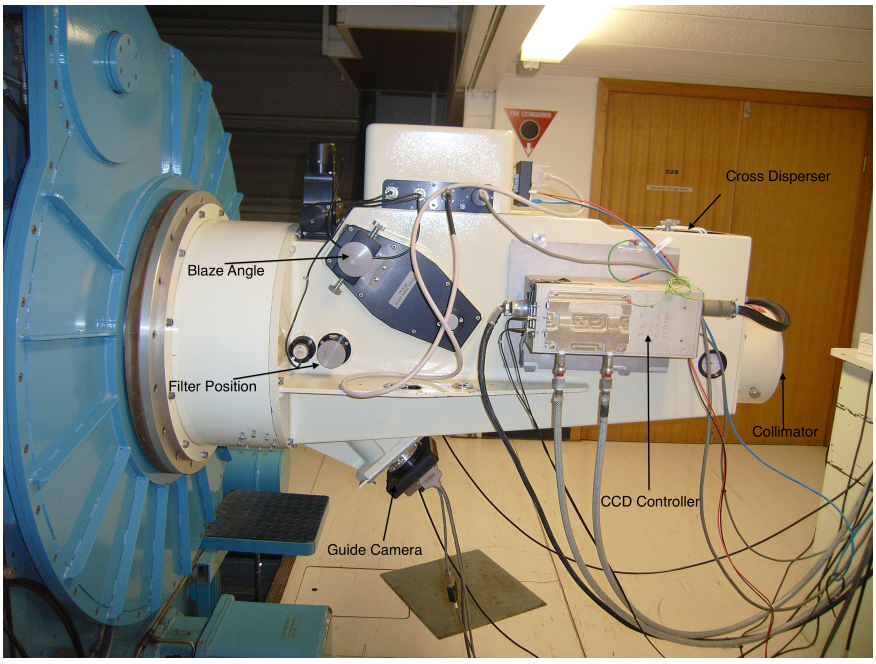

Figure 3.4: The Echelle Spectrograph looking from the rear with the various components labelled.

There is, however, fringing beyond 6600Å, but good flat fielding with a Quartz flat field exposure removes it. Binning of the data by 2 along the slit in the y-direction can be used to improve the signal-to-noise Ratio (SNR) when observing faint stars. It also reduces the readout time. The decision was made not to bin the data for these observations, as early tests did not indicate a significant improvement in the SNR. Most of the targets were bright, and the readout time of ∼15 seconds imposes no significant overhead.

The CCD is cooled by liquid nitrogen via a dewar attached to the front of the instrument as can be seen in Figure 3.3. The CCD dewar can be rotated relative to the spectrograph, in order to have the orders parallel to the CCD rows. The CCD dewar is usually removed for pumping down by technical staff between runs or when an instrument change occurs. It is prudent to check with an arc exposure that everything lines up as it did previously. Pumping down during a run will also occur if there has been a power interruption and the camera has started to warm up. If this occurs a check needs to be done by taking an arc frame and comparing it to the previous night and, if necessary, adjusting the camera rotation slightly in the spectrograph as it may not have been put back in exactly as before.

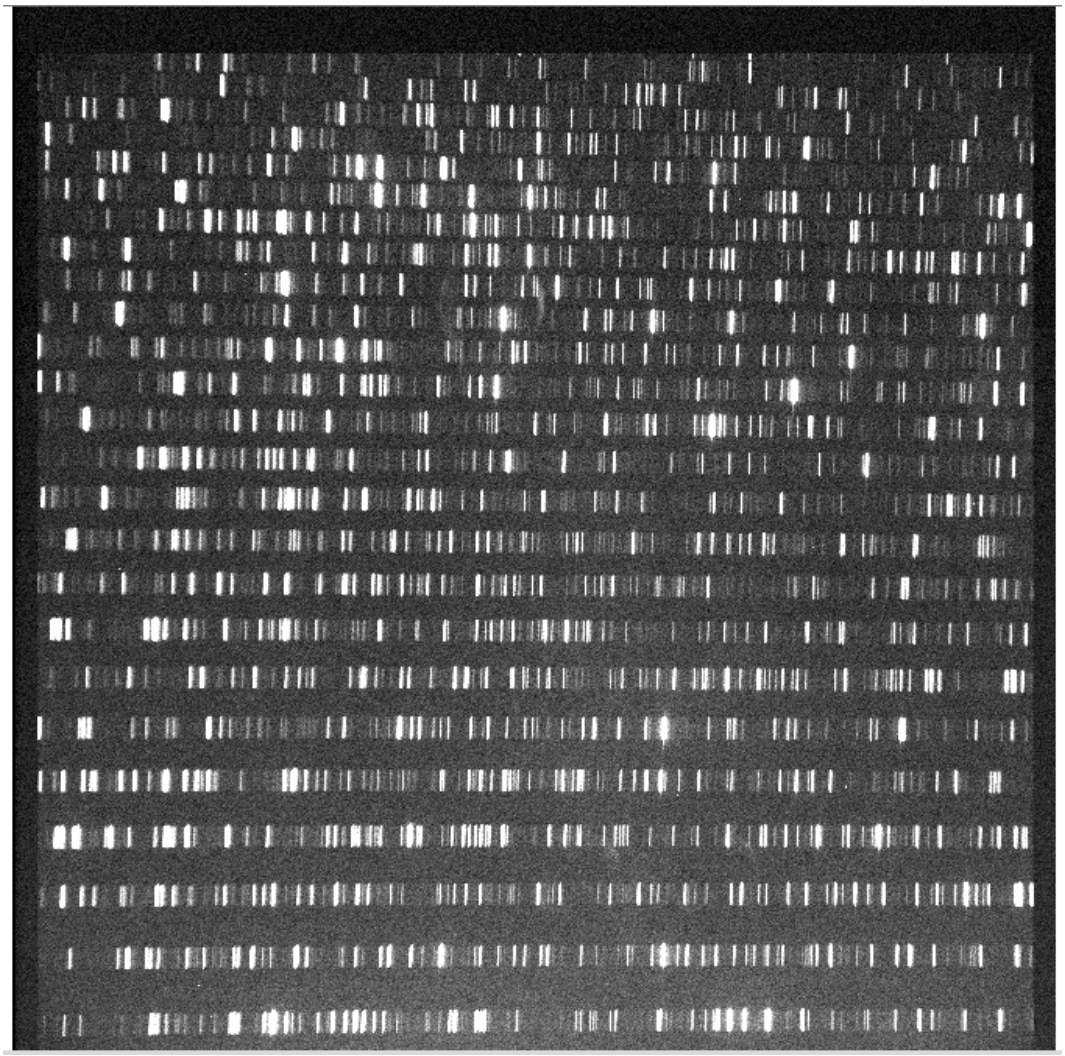

Figure 3.5: Thorium Argon Arc showing asymmetry towards the edge of the frame.

3.2.3 CCD Cooling

There is now an auto-filler for the dewar which fills at 15:00, 23:00, 05:00 and 11:00 (local time). However, for the earlier observations undertaken in 2009/2012, liquid nitrogen filling was the responsibility of the observer, done in the afternoon, prior to opening up and again at the end of observing in the morning. Thorium Argon (ThAr) exposures taken before and after dewar filling in the evening show no significant differences; however, biases have shown some changes when auto-filling occurs during exposures as illustrated in Figure 3.6.

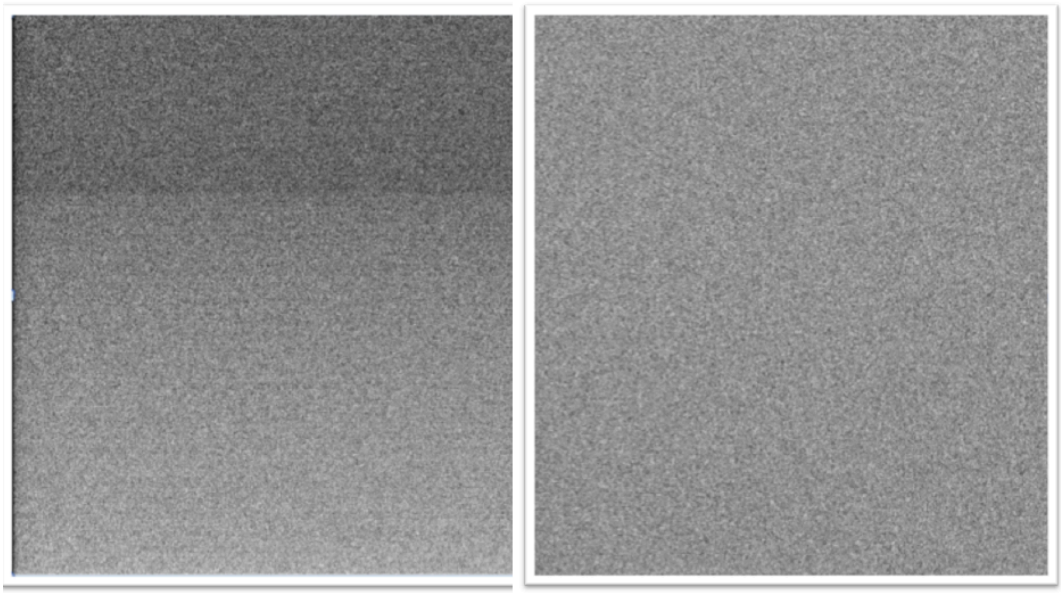

Figure 3.6: Example of Bias Frame affected by Dewar filling. The left hand frame was taken during an automatic dewar fill in 2012 and right hand frame an hour later.

The bias frame on the left was one of ten taken during filling of the dewar, and there is an obvious artefact to be seen. The one on the right was taken about 1 hour later. When this left hand bias was used as part of a master bias it causes major issues with initial data reduction - when the affected biases are removed from the combined files then the data reduction progresses as expected.

3.3 DI Instrument Requirements

Semel *et al.* (1993) and Donati *et al.* (2003b) have laid out a number of instrument requirements for undertaking successful DI. These include both high spectral resolution and a high SNR. High spectral resolution ensures capturing as many resolution elements over the surface of the star as possible, thus providing greater accuracy in the analysis. Since most DI targets observed are active young stars they are usually rapid or ultra-rapid rotators and it is necessary to have an exposure time which is a compromise between high SNR and ensuring exposures are no more than 1% or at the most 2% of the stellar rotation to prevent phase smearing.

3.3.1 Signal-to-Noise Ratio

The instrument needs to collect as much light as possible in order to minimise photon noise.This is the advantage of a larger telescope. The target stars for this project are bright rapid rotators. If the star is faint and so necessitates longer exposures to collect enough photons, then the problem of smearing the Doppler Image and consequently reducing the longitudinal resolution becomes an issue. Semel *et al.* (1993) made the recommendation that individual exposures should not be longer than 1–2% of the stellar rotation period. In the case of AB Dor, the star used to test the feasibility of using this telescope, it is bright at magnitude 6.06, with a rotation period of 0.51479 days or 44426 seconds – 1% of its rotation period is ∼445 seconds. However to get optimal light collecting and keep phase smearing to a minimum, a compromise exposure time of 600 seconds was selected which remains less than the 2% maximum recommended by Semel. A SNR of 50 at Hα has proven to be adequate to measure the required parameters although generally when weather was clear and seeing reasonable a SNR of ∼90-100 was easily achievable at Hα.

3.3.2 Spectral Resolution

In spectral resolution, the smallest scale of stellar feature depends upon the ratio of the rotational line broadening to instrumental broadening. The setup used is optimised to give as complete a coverage of the wavelength range as possible, a Point Spread Function (PSF) FWHM of 3.0 pixels and a resolution ∼24,000 or 0.02nm at 550nm. It was evident early on in the exercise that there was potential for imaging bright and ultra-rapid rotators and that the real challenge would be with rapid rotators and less bright targets.

3.3.3 Instrumental Errors

A key difference between the 2.3-m echelle spectrograph and UCLES on the AAT is that this spectrograph is not permanently mounted and may be removed and replaced between observing runs. This becomes an issue as all settings and adjustments are manual and it is not always a trivial exercise to get exactly the same set up between runs. This may lead to calibration issues. Each night the calibrations need tweaking in software as there are slight changes, whereas, at the AAT, the same calibration settings may be used from night to night, varying little from run to run.

3.4 Observing Methodology

3.4.1 Setup

For the survey and DI studies, the echelle was used in a standard grating configuration of echelle = 0.08 and dekker setting of 13. The 200-micron slit is 1.8 arc seconds wide and projects to 40 microns on the CCD, which is equal to 3 pixels The cross disperser grating of 316/7500Å which is near 6 degrees is used to allow collection of data of orders 57-34 or 3900-6720Å on the CCD. This was selected to allow the capture of the Hα (6562 Å), Li I (6707Å) and Ca II K (3934 Å) and Ca II H (3968 Å) lines. (Figure 3.7)

Appendix A lists the complete spectral format tables for the 2.3-m telescope echelle spectrograph showing the short spectral coverage per order as well as the order overlap. These settings give an almost complete coverage of the wavelength range, a Point Spread Function (PSF) Full Width Half Maximum of 3.0 pixels which matches the typical seeing at SSO and provides a resolution of ∼24,000. The spectra were not binned as readout time is quite fast for the CCD at 15 seconds.

Observations were taken over 16 runs on the telescope between August 2008 and January 2013 as shown in Table 3.1.

A number of runs were reduced to 2 nights due weather or telescope issues. The seeing at Siding Spring ranged between 2" to 5.5" with a resulting signal-to-noise on a single pixel of between 5 and 10 for each individual exposure.

3.4.2 Observing Strategy

Bias frames, Thorium Argon arcs and quartz lamp calibration exposures were taken for the process of data reduction.

A minimum of ten bias frames were also done both at the start and end of the night. These are combined to form a master bias. However, it was found that there were inconsistencies in some biases. These affected the reduction process when combined so biases were checked before combining and many more bias frames were taken to ensure there were sufficient to make a good quality master bias. The bias issue was discussed briefly earlier in this chapter.

The Thorium Argon (ThAr) arc lamp was used for wavelength calibration. A 45 second Thorium Argon arc exposure was taken at the start and end of the night and at least on two other occasions during the night to calibrate for

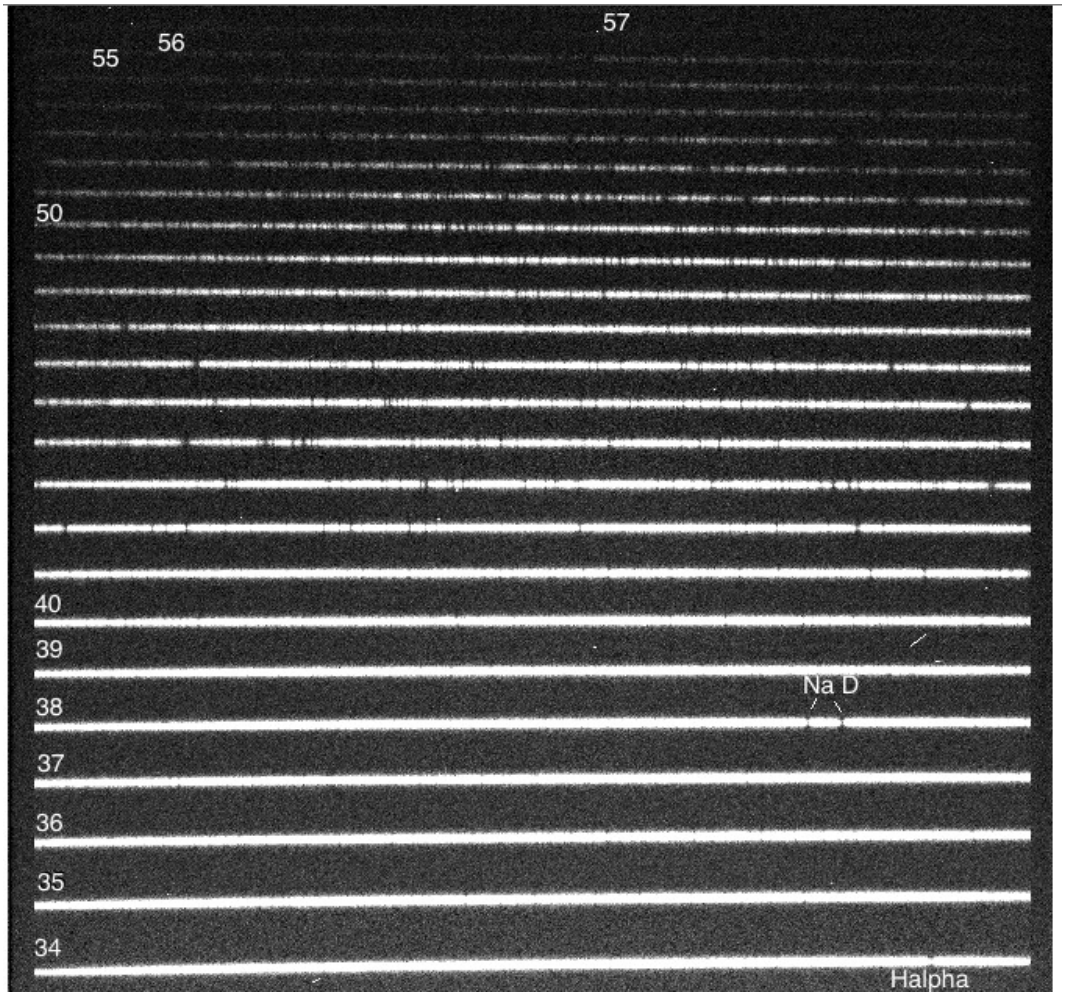

Figure 3.7: An echelle spectra showing orders 34 to 57 covering 3900Å to 6720Å allowing observations from Li 6707Å and CaHK.

possible drifts. Although, over the course of one night, these drifts did not seem significant, they were measurable over the length of run.

A series of ten quartz lamp flats were taken at the beginning and end of each night, and then combined to produce a master flat for the purpose of flat fielding. Exposures of 150-seconds were usually sufficient to obtain ∼25,000 counts, but there were times when exposures of up to 450 seconds were needed to get the requisite count. Although this happened on more than one occasion, no explanation for this anomaly has been found.

Table 3.1: Summary of Observing Runs

Date	Nights Allocated	% Usable Time	Seeing	Notes
Aug 12–18, 2008	7	45%	3-5"	Target Survey
Dec 23, 2008 - Jan 4, 2009	12	60%	3-5"	Target Survey
May 4-11, 2009	7	80%	2-4"	Activity Survey and follow up
June 6-11, 2009	6	0%		Weather issues
Sept 3-4, 2009	2	0%		Weather issues
Dec 24, 2009 - Jan 6, 2010	14	20%	3"	AB Dor Weather issues
Feb 26 - Mar 3, 2010	6	12%	3"-4"	Survey - weather issues
Mar 31- Apr 5, 2010	6	80%	2-4.5"	HIP43720
Aug 1-8, 2010	8	75%	3-4"	Follow up and snapshots
Sep 13-19, 2010	7	45%	3-4"	Survey and follow up
Dec 21- 29, 2010	9	40%	2-3"	AB Dor and follow up
Jan 21-23, 2011	3	90%	2-3"	AB Dor
June 21-29, 2011	9	65%	3-6"	Survey and follow up
Jan 11-15, 2012	5	20%	2-4"	AB Dor and survey
Apr 4 - 9, 2012	6	85%	2-5"	HD106506 and survey follow up
Dec 21, 2012 - Jan1, 2013	12	70%	2-6"	AB Dor, HIP43720 and follow up

The LSD profile is an excellent way of identifying a binary star (Waite *et al.*, 2004), as the LSD profile will often show both stars, unless the star is undergoing an eclipse or its companion is a much fainter star such as an M-dwarf. Hence the strategy to observe stars on more than one occasion in order to ensure, as far as possible, that the star was indeed single (Waite *et al.*, 2004).

All CCD exposures are affected by cosmic rays. The successful reduction of echelle data requires careful attention to be paid to the location and handling of cosmic-ray hits in the data. Reducing exposure length is one way of minimising the effects, and 1800 seconds is the longest exposure time used in order to minimise the numbers of cosmic rays during longer exposures. Calibrations frames need to be checked to ensure cosmic rays are removed prior to attempting reduction. It is particularly important that cosmic rays do not severely degrade the frame used for order tracing, otherwise the whole reduction will be unsuccessful.

Exposure times for DI are based on the rotational period of the star. For bright rapid rotators with a period of 0.5 days, such as AB Dor, 600 seconds was the maximum length of exposure, which although it does lead to some phase smearing it enables an optimum signal-to-noise. In the case of dimmer stars with longer periods, an exposure time of up to 1800 seconds was used to obtain suitable signal-to-noise as per the constraints discussed previously.

The wide wavelength coverage and high-resolution of the echelle allows the simultaneous examination of spectra for Hα emission, the presence of lithium at 6707Å and non-hydrogen emission lines such as Ca II H & K 3969/3933Å, Na I at 5890/5896Å, and He I at 5876/6678Å. Typical resolution at the Li 6708Å order is 0.2 Å/pixel. The echelle spectra collected on these stars which are listed in Appendix B will be useful to estimate stellar ages, metallicity and projected rotational velocity, radial velocity and chromospheric activity from measuring the equivalent width for the Hα spectral line.

3.5 Spectral Data Reduction, Extraction and Analysis with ESpRIT

ESpRIT is an acronym from "Échelle Spectra Reduction: an Interactive Tool". The code was developed by Donati and Collier-Cameron (1997) at the Observatoire Midi-Pyrenees. It is a dedicated pipeline processing software for the processing of both unpolarised and polarised echelle spectra. It performs an optimal extraction of echelle spectra, in spite of the highly nonlinear order shape and non parallel projection of the slit onto the CCD chip.

The software builds on the implementation of Horne (1986) and his principles of optimal extraction as revised by Marsh (1989). It was also generalised to retrieve polarimetric information from Echelle spectra with curved orders and tilted slits. The reshaping of lines in the spectrum due to the magnetic field is a very small effect. The strategy is to consider that this change to a line will have the same basis in all lines. So, instead of looking at one line, thousands of lines are combined. The result is that the detection is now measurable.

The code was extensively used in the 1980s for the extraction of spectropolarimetric and spectroscopic data obtained at the 3.9-m Anglo-Australian Telescope (AAT) with the UCLES spectrograph and SEMPOL polarimeter. It was written for the AAT and UCLES and has presented some interesting challenges in making the necessary modifications for use with 2.3-m data.

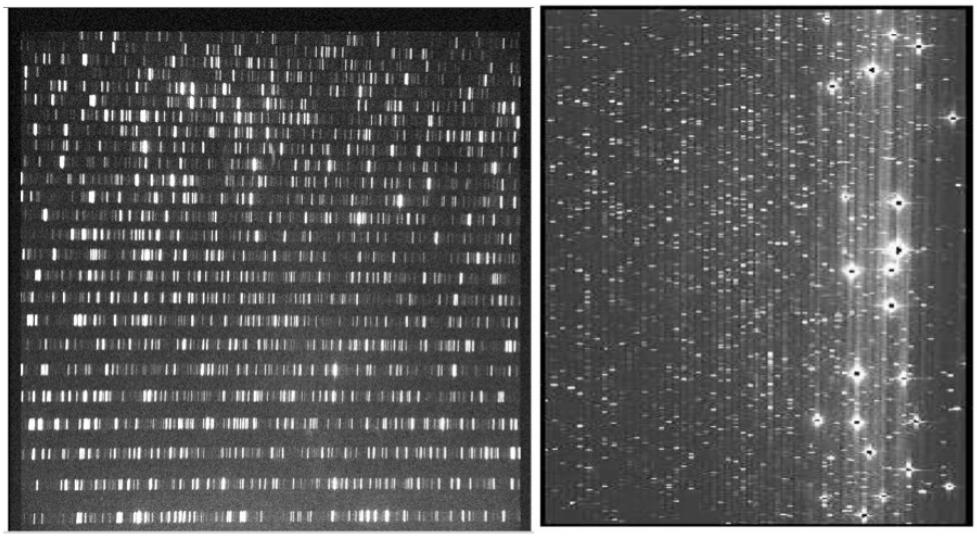

Figure 3.8: Comparison of a Thorium Argon Arc exposure from the 2.3-m echelle (left) and one taken on the AAT with UCLES (right). The lines are orders are horizontal on the 2.3-m arc and vertical on the AAT arc.

A listing of typical input files used in ESpRIT is given in Appendix C.

All raw frames of the observations were reduced using the modified version of ESpRIT to provide wavelength-calibrated spectra. The following subsections consider the various steps/processes involved in creating an LSD profile. Profiles are created each night, and each looked at to identify if there are any issues, low signal-to-noise or solar contamination. However, prior to being able to undertake the geometry and wavelength calibration steps, the fits headers for the 2.3-m data need to be modified as shown in Appendix C

3.5.1 Preparation of Data

- Headers are checked and corrected using the IRAF task - *fitsutil* package to correct for any entry errors.
- Files are then sorted in to Images, Flats, Arcs and Biases after corrections are complete using IRAF.
- The image file headers now can be updated with the IRAF tasks *astutil* and *asthedit* so that they will work with ESpRIT.
- After being updated the IRAF task *setjd* is run on the image files to set the Julian Date which is required by ESpRIT.

Now the files are ready to be used with ESpRIT.

3.5.2 Geometry Correction

The geometric calibration is carried out by a modified version of the routine *geometry*. The modified routine is *geometry_23m* which takes into account the differences between the long slit echelle and the fibre-fed UCLES.

Due to experiencing a number of issues with flats and biases which caused data reduction issues - each bias and flat were examined in DS9 prior to being added to the input file. The purpose of this script is to set up the geometry of the chip and to trace the echelle spectra on the detector, so the software knows where to find the information it needs.

Detector geometry data is manually entered via the *geom.in* file.

- From fits header for 2.3-metre data confirm that the CCD size is 1:2148, 1:2148 and the trimsize is 51:2148, 1:2148 making the bias section is 1:50, 1:2148.
- Using these and by measuring the part of the chip with usable data as shown in Figure 3.9;
- X values 55 2045 (210055=2045);
- Y values 1 2050 (The actual top of chip appears to be at Y= 2053 so use 2048);
- Count number of orders that are complete = 24;
- Next work out the mid point of the first order at x=1000;
- Record y value y=38;
- Subtract from each other (8538=47) then divide the answer by 2 and add to y value at the start of order (38+23.5=61.5);
- Next work out the midpoint of middle order at position X=1000 and Y=500 then measure the distance between rows by taking the value of Y at the start of a new row;

These are first approximations to be used in the *geom.in* file as shown in Appendix C.

The software then analyses the flat, bias and arc frames and generates polynomials for tracing on the spectral orders on the CCD and the output is written to the *geom.dat* file and utilised in the wavelength calibration as well as the intensity spectrum extraction process.

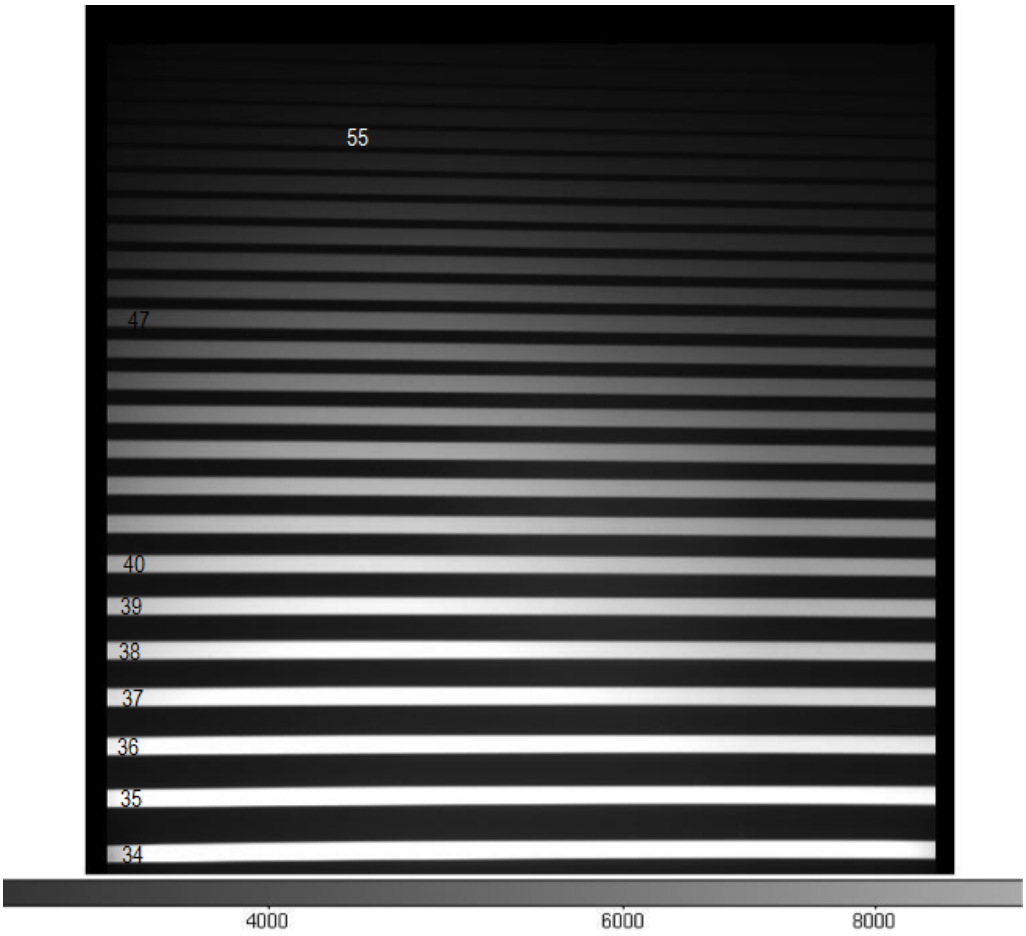

Figure 3.9: Flat File in SAOImage DS9 showing order numbers.

3.5.3 Wavelength Calibration

Light from a thorium-argon arc lamp is used to establish a wavelength scale. Two established lines from the lamp were recorded, and subtraction of wavelengths and pixel numbers gives dispersion in nm per pixel.

ESpRIT uses a polynomial applied to the wavelength to compensate for non-linearity in the spectra. Thus, the position on a pixel can be given a wavelength for the entire spectrum.

The next step is the wavelength calibration that is carried out by the routine *wcal_23m*. This requires similar input parameters to **geometry** including the starting order, the order increment and the first order to be calibrated which must be the same as previously input. The routine also requires an approximate starting wavelength (in nm) and dispersion measurement (in nm per pixel), for the first order. This enables it to perform an initial calibration

of the first order and compare it to a list of known lines in a ThAr atlas.

Calibration of the remaining orders is then completed. The calibration information is then saved to an output file (*calib.dat*) to be used in the intensity spectrum extraction process. The script *wcal_23m* takes the information manually specified in the *wcal.in* file and then generates polynomials that represent the wavelength calibration for each spectral order. After *wcal_23m* has run for the first time, a visual check is carried out for best fit curves and lowest root mean square (RMS). The routine should then be be run again with changes as necessary to approximate λ and dispersion figures until the optimal result is achieved. The goal is to achieve consistency in the smoothness and RMS for each order and to maximise the number of lines recognised. The minimum preferred is 1,000 lines.

This process is done each night with calibration exposures taken prior to observing. Running the *wcal_23m* with different ThAr arcs can get very different results showing that, over the night, there are variations. This also is a point of difference with reducing AAT/UCLES data as there is no variation. This is because UCLES is a bench-mounted spectrograph in the East coude room at the AAT and the 2.3-m echelle is on the telescope itself and is subject to movement and temperature variations during the night.

3.5.4 Intensity Spectrum Extraction

Extraction of the intensity spectra is performed by the the ESpRIT routine *extract_23m*. This routine utilises the output data files produced by *geometry_23m* (*geom.dat*) and *wcal_23m* (*calib.dat*), as well as a flat field and a bias exposure.

In conjunction with the stellar exposures, *extract* subtracts the bias from all exposures and divides the stellar exposures by the flat field to correct for pixel-to-pixel sensitivity differences.

For intensity analysis all the frames have any bias subtracted and a correction is made for differences in sensitivity between pixels by comparison with the relevant pixels when exposed to the flat field. Cosmic ray bombardment is responsible for some pixel measurements deviating from the average intensity of the order. These are discarded if they are beyond a set threshold.

Extract takes one star FITS file and produces an output spectrum typically called *spectrum.dat* but can be named with any preferred naming convention.

3.5.5 Instrumentation Shift Correction

During the night, there can be small variations in the spectrograph, as a result of temperature changes from the dewar refill or from very slight mechanical or thermal changes within the instrument or components.

This slight instrumental shift need to be corrected for and that is achieved by the wavelength calibrated spectra being shifted with respect to the LSD profile of the telluric lines within the spectrum. This is important to reduce errors in radial velocity measurements. Telluric lines are only found in the Earth's atmosphere have no radial velocity. The procedure of Donati *et al.* (2003b) is used with the ESpRIT code for data analysis and correction. Atmospheric water or telluric lines are extracted from the wavelength calibrated extracted stellar spectra and then corrections are made to remove the small instrumental shifts. This process is achieved using an automated script called *cvel* and can reduce errors due to instrumental shift to less than 0.1 km s^{-1} (Mengel, 2005).

Heliocentric velocity corrections are applied when the wavelength calibration of the extracted spectra is performed using a shell script called *autoextr*.

3.5.6 Summation of the Line Profiles using Least Square Deconvolution

Running the routine, *sum*, enables a summation of line profiles using Least Square Deconvolution (LSD) to produce an LSD profile from the spectrum, which has been corrected for radial velocity changes.

Successfully creating a LSD profile requires a list of lines and their relative weightings for a normalised spectrum. Donati and Collier-Cameron (1997) generated line lists from a full LTE spectral synthesis using the ATLAS9 model atmospheres and SYNTHE routines of Kurucz (1993) and Table 3.2 shows the list of Spectral types available in ATLAS. These line lists were used for all data reduction in this thesis relating to DI.

The next step is to create a postscript of the LSD profile using the script *Disp* and then to extract the Heliocentric Julian Date (HJD) from the header files, given that the header files have been updated to show the HJD as discussed in 3.5.1. Each of these scripts can be combined into a single script, and once all the correct parameters are identified a script can be run to create the profiles for all targets on each night.

Table 3.2: Table of Spectral Types available in ATLAS

A0	A1	A2p	A4	A5	A6p	AB
B1	B2	B4	B6	B8p		
F1	F1p	F6				
G2	G7					
K0	K1	K5				
M0						
O7						

However, because of the issues with the 2.3-m echelle variations between nights these scripts need to be adjusted each night. However, the geometry and wavelength calibration can be done after the calibrations are finished early in the evening. This can be suitable to create rough LSD profiles, on the fly, during the night to check for solar contamination, poor signal-to-noise or other issues with the observations. Later, new geometry and wavelength calibration files can be created for each arc taken and used for reducing the data taken in the relevant time frame.

3.5.7 Least Square Deconvolution

To detect the signatures of the spots on the line profile, the software utilises the mathematical technique called Least-Squares Deconvolution (LSD). Donati and Brown (1997) combined lines using this cross-correlation technique, which enables the computing of average profiles simultaneously from thousands of spectral lines and is used to produce a high signal-to-noise mean profile of all the spectral lines in each spectrum. With the echelle spectrograph having overlap in a number of orders the number of lines used in the LSD extraction is greater than the actual number of lines in the spectrum. This works because the presence of spot features in the photosphere of the star affects all these lines in a similar way. The result is a significant increase of up to 10 to 15 times in the SNR when compared to a single line. While many of the lines appear twice they are treated as individual lines increasing the signal-to-noise.

LSD is used to increase the signal-to-noise in the intensity data while still retaining the intensity information in the spectrum. For intensity signatures (Stokes I) the multiplex gain is usually significantly less than this (Donati and Brown, 1997). This technique is not that different from other cross-correlation

techniques but does vary in the way it cleans the cross-correlation profile from the auto-correlation profile of the line pattern to yield a profile which has the requisite high SNR necessary for image reconstruction.

According to Waite *et al.* (2004) the technique of LSD provides a method of obtaining an accurate $v\sin i$ measurement and through the distortions visible in the profile which are due to changes in surface brightness which indicate the presence of surface inhomogeneities such as a dark spot feature.

These measurements can be made to a high level of accuracy in moderate to ultra-rapid rotating stars. Even though the typical variations in intensity amplitude are very small in the order of ≈1% this technique works on the premise that a very small effect, when compounded across thousands of lines will produce a discernible signal.

Since the photospheric lines in the spectrum are assumed to be all affected in the same way by the presence of spots in the stellar photosphere, the observed profile of these lines must be equal to a basic line pattern (M) convolved with the spot signature (Z) from the spots. Therefore the observed intensity spectrum of the star **I** can be written as:

$$I = M * Z \tag{3.1}$$

where **M** is the line pattern (or line mask) of the spectrum with a weighted mean of all the lines selected for analysis. For AB Dor this line mask was created for a K1-type atmosphere based on the Kurucz atomic database and ATLAS9 atmospheric models (Kurucz, 1993), while for HIP43720 a G2 line mask was created. **Z** is then found through a least-squares solution:

$$Z = ({}^tM \cdot S^2 \cdot M)^{-1}\ {}^tM \cdot S^2 \cdot I \tag{3.2}$$

Where, **S** is a square diagonal matrix in which element S_{jj} is the inverse error bar $(1/\sigma_j)$ for pixel *j*. This deconvolves the raw cross-correlation function (stored in ${}^t\mathrm{M} \cdot \mathrm{S}^2 \cdot$ I) from the autocorrelation profile (stored in ${}^t\mathrm{M} \cdot \mathrm{S}^2 \cdot$ M) and is known as least-squares deconvolution. Further information on LSD can be found in Wade *et al.* (2000) and Donati and Brown (1997).

The software for both the production of the profiles and imaging used were provided by J-F Donati.

3.5.8 Producing the Doppler Image Map

This step takes the data and rearranges it into a form suitable for the imaging code to be able to process. It can also combine any photometric data that is available for the particular star. In the case of both AB Dor and HIP43720, no photometric data was available.

There are a number of methods used to produce Doppler Image maps of cool stars. The various methodologies use either a Fourier filtered back-projection algorithm (FFB) or a maximum-entropy minimisation technique (MEM) (Schwope, 2001). The Doppler Image maps of AB Dor and HIP43720, in this thesis, used a maximum-entropy minimisation technique.

The maximum-entropy minimisation technique uses spectral line inversion to compute the minimum spot features that would produce the observed spectroscopic features. A reconstruction is then built based upon the contribution of each pixel to a cool spot on the surface of the star. The photosphere and spots are matched against the synthetic Gaussian profiles as used in Petit *et al.* (2002). This gives consistency to the results as well ensures adequate convergence. In the mapping of brightness, a filling factor is used. This filling factor is based on 0 for no spot and 1 for a total spot convergence (Collier-Cameron, 1992). The data are then fitted to the desired accuracy, which is usually the level of noise.

3.5.9 Maximum Entropy Reconstruction

Maximum entropy reconstruction generates images, which contain the minimum information (surface features) required to produce the observed spectroscopic variations. By observing a star at different phases in its rotation, obtaining high-quality LSD profiles for both intensity and magnetic signatures, maximum entropy reconstruction is able to infer the surface topology of the star.

The code used for the DI in this thesis is that of Brown *et al.* (1991) and Donati and Collier-Cameron (1997), which implements the algorithm of Skilling and Bryan (1984) for maximum entropy optimisation.

The mapping of surface spot features uses the two-component brightness model (one for the spot and the other for the photosphere) from Collier-Cameron (1992). In this model the local relative area occupied by cool spots for each pixel on the stellar surface is reconstructed (Marsden *et al.*, 2005).

Donati *et al.* (2000) used LSD profiles of standard stars to represent the spot and photosphere temperatures of the targets. Petit *et al.* (2002, 2004) and Marsden *et al.* (2005) used synthetic Gaussian profiles as this provides consistency and adequate convergence. The results of Unruh and Collier-Cameron (1995) and Marsden *et al.* (2005) demonstrate that Doppler Images reconstructed from a Gaussian line are almost identical to those obtained using the profile generated from a standard star. Hence, in this work Gaussians profiles were used.

In the image reconstruction code the form of entropy used is:

$$S[f,m] = S_1[f,m] + S_1[(1-f),(1-m)] \tag{3.3}$$

where

$$S_1[f,m] = \sum_i [f_i(\log(\frac{f_i}{m_i} - 1) + m_i)] \tag{3.4}$$

and

$$S_1[(1-f),(1-m)] = \sum_i [(1-f_i)(\log(\frac{(1-f_i)}{(1-m_i)} - 1) + (1-m_i))] \tag{3.5}$$

In this case **f** is the photosphere filling factor and **m** is the default unspotted filling factor (set to 0.9999).

The values for the filling factors are interactively adjusted to maximise:

$$Q = S(f,m) - \lambda\chi^2(f,m) \tag{3.6}$$

Where λ is the Lagrange multiplier and χ^2(f,m) measures the accuracy of the fit and is determined by:

$$\chi^2(f,m) = \sum_k (\frac{F_k - D_k}{\sigma_k})^2 \tag{3.7}$$

where F_k is the modelled data, D_k is the observed data, and σ_k is calculated from an estimate of the error in the LSD and photometric profile.

The data is then fitted within a desired accuracy of $\chi^2 = \chi^2_{aim}$.

The level of ${\chi^2}_{aim}$ to which to fit the data should normally be 1.0 which is equivilant of the the noise level.

If a ${\chi^2}_{aim}$ value of less than one is obtained it means that the error bars have been overestimated.

The error bars in the Doppler Imaging code used here are estimated by scaling the following formula:

$$E = \sum_k \frac{((M * Z)_k - S_k)^2}{\sigma_k^2} \tag{3.8}$$

where, **M**, **Z** and **S** are as in the previous subsection; and σ is the error.

If E $>$ 1 the error bars are scaled by $\sqrt{E}$. This has the effect of usually overestimating the error bars but has no effect on the images produced.

3.5.10 Reformat

Reformat generates the .dat file which is required for *ZDICam* to be able to generate the map. *Reformat* takes the data from *sum* and rearranges (reformats) it for input to the imaging code. It can also make use of photometry if available.

Creating the reformat.in file requires the following information:

- Epoch is calculated by subtracting the Heliocentric Julian Date (HJD) of first observation from the HJD of the last observation.
- Phase 0 can either be the first observation or it can be set at the midpoint of the run. If the latter, then to obtain Phase 0, add half the epoch to HJD of first observation. Using the midpoint of the run is usual when doing differential rotation measurements.
- Phase = (HJD − Epoch)/period.
- Signal-to-noise values for each LSD profile are obtained from *sum.log*.
- Spectral Resolution is extracted from the *wcal.out* file.
- From the LSD profile of the star identify the defined edges of the wing and select a point on either side of the wing shoulder to obtain a mean value of $v\sin i$.
- Initial radial velocity input may be obtained from literature.

Table 3.3: Input Table for use in Reformat.in

Filename	Number of profiles	Type of obs	phase	SNR	resolution
ABDor110121014.lsd	1	I	0.0000	857	24000
ABDor110121015.lsd	1	I	0.0138	854	24000
ABDor110121017.lsd	1	I	0.0746	854	24000
ABDor110121018.lsd	1	I	0.0884	849	24000
ABDor110121019.lsd	1	I	0.1022	845	24000
ABDor110121020.lsd	1	I	0.1160	840	24000
ABDor110121021.lsd	1	I	0.1300	846	24000
ABDor110121022.lsd	1	I	0.1437	848	24000
ABDor110121023.lsd	1	I	0.1575	846	24000
ABDor110121024.lsd	1	I	0.1715	844	24000
ABDor110121025.lsd	1	I	0.1853	839	24000
ABDor110121026.lsd	1	I	0.1991	800	24000
ABDor110121027.lsd	1	I	0.2129	836	24000
ABDor110121028.lsd	1	I	0.2269	833	24000
ABDor110121029.lsd	1	I	0.2413	825	24000

A list of all the profiles and the other information either calculated or known is then used to create an input file such as the one shown in Table 3.3. The number of profiles is usually 1, while the type of observation is **I** for Intensity Profile when doing DI.

The values of radial velocity, continuum and right and left span can be modified. Each time a change is made, however, the code needs to be rerun to refine it and obtain the best quality Doppler Image map.

3.5.11 *GScale*

GScale takes the information from *reformat.s* to make create *reformat.rs*. It normalises the equivalent width (EW) of all LSD Profiles to the first LSD profile in the list. By normalising the EW, it flattens out the wings of the profile, which allows a better fit to the model data.

When run, this script produces a graph of Equivalent Width (EW) against signal-to-noise Ratio (SNR).

3.5.12 ZDICam

ZDICam is the maximum entropy code used for the Doppler Imaging of the targets in this project. It produces modelled fits to the observed profiles which are then fitted to the minimum reachable ${\chi^2}_{aim}$.

The stellar parameters, such as radial velocity, $v\sin i$, and inclination angle can be determined using the maximum entropy reconstruction code. The ${\chi^2}_{aim}$ is important as it contributes to the calculation of spot coverage.

To determine each of these parameters, successive runs of *ZDIcam* are done until a minimum ${\chi^2}_{aim}$ is reached for each particular stellar parameter. This derived value is then used in subsequent runs to continue to minimise the ${\chi^2}_{aim}$ for the next parameter until a favourable combination of all stellar parameters produces the lowest ${\chi^2}_{aim}$ (Rice, 2002).

3.6 Limitations of Doppler Imaging

The Doppler Imaging technique has limitations associated with its usage. In his review, Rice (2002) gives an overview of the limitations which can have an impact upon undertaking successful Doppler Imaging.

These issues affect the area of spot coverage, which can be resolved on the stellar surface.

These issues include:

- inadequate phase coverage;
- too much phase overlap;
- inadequate SNR;
- insufficient spectral and spatial resolution; and
- incorrect initial stellar parameters.

Petit *et al.* (2002) addresses the issue of phase coverage and overlap as it is a common problem.

To reconstruct a complete and accurate spot occupancy map, there needs to be as full a phase coverage as possible. Only small gaps are desirable. Phase overlap generally is not a problem in the fastest rotators as the issue only occurs where there has been spot movement in the time between successive phase observations. It can be an issue with slower rotators where observations are collected over weeks or months.

Phase overlap is a more significant issue when attempting differential rotation measurement, as it is preferable to have as many sections of the stellar surface visible at as many phases as possible.

Spectral resolution and SNR are equipment limitations and affect the resolvability of the surface features particularly for faint targets. These limitations are minimised to some degree through the use of LSD which enables the production of high SNR profiles.

Spatial resolution, particularly in the case of targets with low $v\sin i$ values, is a critical factor in the percentage of spot coverage measurable. Piskunov *et al.* (1990) concluded that the analysis of a target with a $v\sin i$ of 15 km s^{-1} was unable to resolve the detail that was able to be resolved on a target of $v\sin i$ of 30 km s^{-1} with the same spatial resolution. For a telescope and lower resolution spectrograph, such as the 2.3-m and its echelle, this imposes a limitation of observing only brighter stars or those with very high $v\sin i$.

It is necessary to consider the above limitations, when making conclusions about the resulting spot occupancy maps and differential rotation measurements and DI maps should always be interpreted with care.

3.7 Discussion

Doppler Imaging is a robust procedure, especially at higher signal-to-noise ratios, which result in greater detail being produced in the reconstructed images. Obtaining the correct parameters is essential and even more so important if a differential rotation measurement is required from cross-correlation of constant latitude strips between observations at two different epochs.

Using the instrumentation, observations and analysis described in this chapter the results of Doppler Imaging of two stars AB Dor and HIP43720 are presented in Chapters 4 and 5.

Chapter 4

Testing the Suitability of the 2.3-metre Telescope for Doppler Imaging Studies Using AB Dor

4.1 Introduction

Magnetic activity on solar-type stars can be readily observed using starspots, which can be seen in the photometric modulation of the light from the star. The advent of Doppler Imaging has made it possible to map the location of spot features on rapidly rotating ($v\sin i \geq 20$ km s^{-1}) stars. Such stars are predominantly young, active, and show significant starspot features which makes them well suited to being studied with this technique.

The primary purpose of this project is to determine the suitability of the ANU 2.3-m telescope and its echelle spectrograph to undertake scientifically useful Doppler Imaging studies of active young solar analogues. This chapter presents the first outcome of the feasibility study, which includes preliminary results for the Doppler Imaging (DI) of AB Dor. This rapidly rotating K0 dwarf, AB Dor (HD36705), was chosen because it has been well studied by the techniques of DI and ZDI in the past. Its youth is indicated by strong lithium absorption, and it has a rotational period of ∼0.51 days (Hussain *et al.*, 2001). So, with a $v\sin i$ of ∼89 km s^{-1} and well placed in the southern sky it was an excellent target to test the capabilities of the telescope/instrument setup.

4.2 AB Doradus

AB Dor is an excellent example of the group of very active, rapidly rotating cool stars that are just evolving onto the main sequence. Its rapid rotation, and ∼0.51479 day period makes it an ideal candidate for high-resolution spectroscopic techniques such as Doppler Imaging. Surface maps of this star have been obtained since 1992 with UCLES on the Anglo-Australian Telescope (AAT).

AB Dor has been observed across most of the electromagnetic spectrum, and its activity studied in detail in the X-ray band (García-Alvarez *et al.*, 2005; Hussain *et al.*, 2005; Maggio *et al.*, 2000). More relevant to the current project is that AB Dor has been extensively observed using both Doppler Imaging and Zeeman-Doppler Imaging (ZDI) at the AAT (Donati and Semel, 1990; Donati and Landstreet, 2009). The Zeeman Doppler Imaging technique has been used to map the surface magnetic field of AB Dor (Donati and Collier-Cameron, 1997; Donati *et al.*, 1999; Hussain, 2002), as well as to study its possible stellar cyclic activity and surface differential rotation (Collier-Cameron and Donati, 2002; Donati and Collier-Cameron, 1997; Jeffers *et al.*, 2006). Järvinen *et al.* (2005) also used Doppler Imaging to investigate the possibility of stellar cycles on AB Dor.

AB Dor is a quadruple, pre or zero main sequence, stellar system with AB Dor A being the main component. The system consists of two binary systems; AB Dor A/AB Dor C and AB Dor Ba/AB Dor Bb. AB Dor A has a low-mass companion, AB Dor C, which induces a reflex motion first detected by very-long-baseline-interferometry (VLBI) and the HIPPARCOS satellite (Guirado *et al.*, 1997). The other physical component is a dM4e star AB Dor B (Rst137B) which is also a rapid-rotator with a 0.38 day period. The separation between AB Dor A and AB Dor B is 9" (Lim *et al.*, 1994). According to Close *et al.* (2005), based on their young age, common proper motions, and common radial velocities (Innis *et al.*, 1986) both stars are believed to be associated. Close *et al.* (2005) found that AB Dor B was also a close binary system comprising of AB Dor Ba and AB Dor Bb separated by 0.07". The effect of AB Dor being a multiple system is seen in the variations in radial velocity as the orbits of each part of the system impact on each other.

Close *et al.* (2005) obtained a near-infrared image of AB Dor C, using the NACO SDI camera on the European Southern Observatory(ESO) 8.2-metre VLT.

Figure 4.1 shows this enhanced false colour infrared image of AB Dor A and

C. The faint companion, AB Dor C can be seen, as a pink dot at 8 o'clock and is 120 times fainter. It was able to distinguish it as a "redder" dot surrounded by the "bluer" light from AB Dor A at a distance of 0.156". The computed orbit of the companion around the primary is shown.

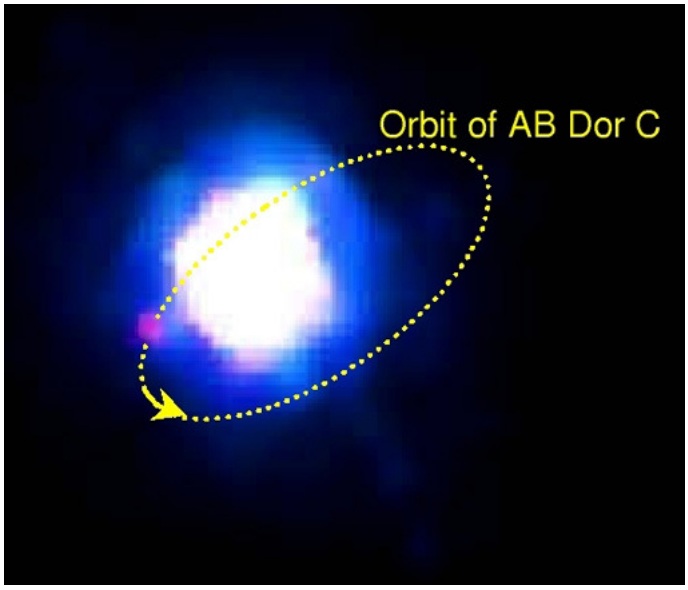

Figure 4.1: Infra-red false colour image of AB Dor A and its close companion AB Dor C taken with the VLT in Chile. (Picture: Steward Observatory, University of Arizona) (Close *et al.*, 2005)

4.3 AB Dor: Fundamental Stellar Parameters

AB Dor is the most active star in the solar neighbourhood. It is a young rapidly rotating K0 dwarf with a $v\sin i$ of 89 km s^{-1} and a 0.51479 day rotational period (Zuckerman *et al.*, 2011). The distance to the star of 14.9 pc, measured by HIPPARCOS, combined with the brightest state so far observed of V=6.75 (Amado *et al.*, 2001) leads to the absolute magnitude M_v of 5.89.

It is a member of the AB Doradus Moving Group, a loose stellar association of about 30 stars, at a distance of ∼15.17 pc (Koen *et al.*, 2010).

It has a visual magnitude of 6.99 and has an age of 50 Myr (Luhman *et al.*, 2005). The fundamental physical parameters of AB Dor are listed in Table 4.1.

Table 4.1: Listing of Fundamental Stellar Parameters for AB Dor from Literature.

Parameter	Value	Ref
Stellar axial Inclination, i	60°	(Donati *et al.*, 2003a)
Projected equatorial rotation velocity, $v\sin i$	89 km s^{-1}	(Donati *et al.*, 2003a) heightPhotospheric
Temperature	5,000 K	(Donati *et al.*, 2003a)
Spot temperature	3,500 K	(Donati *et al.*, 2003a)
Radial Velocity	29.5 km s^{-1}	(Torres *et al.*, 2006) (Strassmeier, 2009)
Rotational Period	0.51479 days	(Zuckerman *et al.*, 2011) (Innis *et al.*, 1988)
Spectral Type	K1	(Scholz *et al.*, 2007)
Mass	0.76 M$\odot$	(Zuckerman *et al.*, 2011)
Radius	0.86R$\odot$	(Maggio *et al.*, 2000)

4.4 Observations January 2011 - AB Dor

Observations were taken of AB Dor over the period 21-23 January 2011 inclusive using the ANU 2.3-metre telescope and high-resolution spectrograph. Over the course of the January 2011 observing run, potentially 54 usable exposures were taken of AB Dor.

The exposure time for each AB Dor observation was 600 seconds. This allows sufficient light to be collected to obtain a high enough signal-to-noise to successfully be able to undertake effective Doppler Imaging of the target ($V\_mag = 6.99$) (Koen *et al.*, 2010) without generating rotational spot smearing due to the rapid rotation of the star. (89 km s^{-1}) (Jeffers *et al.*, 2006)

The run was affected by high cloud on each night with seeing ranging from 2.5" to 5.0". A log of the January 2011 AB Dor observations can be seen in Table 4.2. A total of 54 exposures of the star were taken, with a subset of only 50 exposures used here as the other 4 had too low a signal-to-noise value to be useful having been taken through thickening clouds.

In Table 4.2, the first two columns list the observation date in Universal Date and exposure number. The exposure numbers are not necessarily in consecutive order as other stars and calibration frames were also observed during these nights. Columns 3 and 4 show the Universal Time (UT) start time and

end time of the exposures, respectively, while the last two columns list the exposure time in seconds, and the phase at which the target was observed.

Rotational phases were calculated using an orbital period of $P_{orb} = 0.51479$-d (Innis *et al.*, 1988; Zuckerman *et al.*, 2011).

The zero or starting phase (P_0) was set to the middle of the run;
The starting time of the observations of the target star in Heliocentric Julian Date (HJD_{start}) was 2454830.059801; and
the end time of the observations of the target star in Heliocentric Julian Date (HJD_{end}) was 245836.1368712.

The calculations are:

$$Phase(E) = HJD + \left(\frac{\frac{HJD_{end} - HJD_{start}}{2}}{P_{orb}} \right) \tag{4.1}$$

$$Phase(E) = HJD + \left(\frac{(2454836.136871 - 2454830.059801)/2}{0.51479} \right) \tag{4.2}$$

$$P_0 = 2454830.059801 + 3.0385351 = 2454833.098336 \tag{4.3}$$

This translates to a time between runs 46 and 47 on January 22, 2011.

The time of P_0 can be set to the first observation of the target on a run; to the mid-point of the observing run or according to a predefined ephemeris. If comparing data from runs separated in time and if the actual observation times of the previous runs are available using the latter would be the usual method. However there was no access to the observing logs for the 2002 data that was used to produce the comparison map so it was not possible to set then to similar phases for comparison purposes. A P_0 set to the middle of a specific observing run is usually used when doing differential rotation measurements. The P_0 set to the mid-point of the run was used as a convention for these observations as well as for those of HIP43720 in Chapter 5.

Table 4.2: Log of Observations for AB Dor - Jan 21-23, 2011

UT Date	Exposure Number	Exposure Time	UT Start	UT End	Phase	SNR
2011Jan21	14	600	12:22	12:32	-1.98456	856
2011Jan21	15	600	12:32	12:42	-1.97073	853
2011Jan21	17	600	13:17	13:27	-1.91001	854
2011Jan21	18	600	13:27	13:37	-1.89618	850
2011Jan21	19	600	13:38	13:48	-1.88235	846
2011Jan21	20	600	13:48	13:58	-1.8685	842
2011Jan21	21	600	13:59	14:08	-1.85468	848
2011Jan21	22	600	14:09	14:19	-1.84085	849
2011Jan21	23	600	14:19	14:29	-1.82693	847
2011Jan21	24	600	14:29	14:39	-1.81308	846
2011Jan21	25	600	14:40	14:50	-1.79926	841
2011Jan21	26	600	14:50	15:01	-1.78543	835
2011Jan21	27	600	15:01	15:11	-1.7716	838
2011Jan21	28	600	15:11	15:21	-1.75775	833
2011Jan21	29	600	15:21	15:41	-1.74334	827
2011Jan21	30	600	15:41	15:52	-1.72951	831
2011Jan21	31	600	15:52	16:02	-1.71566	830
2011Jan21	32	600	16:02	16:12	-1.70184	842
2011Jan21	33	600	16:12	16:22	-1.68801	846
2011Jan21	34	600	16:23	16:33	-1.67418	848
2011Jan21	35	600	16:43	16:53	-1.65889	849
2011Jan21	36	600	16:54	17:04	-1.64507	845
2011Jan22	33	600	10:07	10:17	-0.22428	857
2011Jan22	34	600	10:17	10:27	-0.21038	858
2011Jan22	36	600	11:00	11:10	-0.15258	824
2011Jan22	38	600	11:20	11:30	-0.11099	785

Continued on next page

Table 4.2 – *Continued from previous page*

UT Date	Exposure Number	Exposure Time	UT Start	UT End	Phase	SNR
2011Jan22	39	600	11:31	11:41	-0.09696	792
2011Jan22	42	600	12:01	12:12	-0.06861	832
2011Jan22	43	600	12:12	12:22	-0.05478	846
2011Jan22	44	600	12:22	12:32	-0.04091	855
2011Jan22	45	600	12:33	12:43	-0.02706	848
2011Jan22	46	600	12:43	12:54	-0.0128	852
2011Jan22	47	600	12:54	13:04	0.00102	840
2011Jan23	24	600	12:26	12:36	3.7013	849
2011Jan23	25	600	12:42	12:52	3.7153	854
2011Jan23	26	600	13:06	13:16	3.7291	851
2011Jan23	27	600	13:16	13:26	3.7429	863
2011Jan23	29	600	13:26	13:36	3.8029	864
2011Jan23	30	600	13:37	13:47	3.8169	862
2011Jan23	31	600	14:21	14:31	3.8307	864
2011Jan23	32	600	14:31	14:41	3.8445	860
2011Jan23	33	600	14:42	14:52	3.8583	855
2011Jan23	34	600	15:52	16:02	3.8721	858
2011Jan23	35	600	16:02	16:12	3.8861	858
2011Jan23	36	600	16:12	16:22	3.8998	858
2011Jan23	37	600	16:23	16:33	3.9138	833
2011Jan23	38	600	16:33	16:43	3.9276	825
2011Jan23	39	600	16:43	16:53	3.9414	831
2011Jan23	40	600	16:54	17:04	3.9552	859
2011Jan23	41	600	17:04	17:14	3.9692	840

4.5 Determining Stellar Parameters Using Maximum Entropy Reconstruction

Although the determination of most stellar parameters should not change between observing runs, there are some, however, which may be affected by aspects of the observing such as phase coverage or improvements in data analysis methodologies. Those which may be affected include the values of $v\sin i$, radial velocity, inclination angle (i), and the equatorial rotational period. Except for the rotational period, the process to determine these parameters, either to confirm previous results or to find new values, is that of Barnes *et al.* (2002) through the use of χ^2-minimisation, where the parameter that produces the lowest ${\chi^2}_{aim}$ value is selected to be used to obtain the value of the next parameter.

To determine the correct stellar parameters (i.e. radial velocity, $v\sin i$and inclination angle i) to use when creating a DI map, the maximum entropy reconstruction code, *ZDICam* can be utilised. Radial velocity, $v\sin i$ and the inclination angle (i) can all be identified in this way.The equatorial rotational period used was taken from the literature.

Establishing these parameter values require identifying an initial 'best guess' value for each parameter and then undertaking successive runs of the code until a minimum ${\chi^2}_{aim}$ value is reached. The first parameter identified, which was, in this case, radial velocity, is then used in subsequent runs until all three parameters are identified by continuing on and obtaining the lowest ${\chi^2}_{aim}$ value for each parameter until they all converge producing the lowest ${\chi^2}_{aim}$ value as per Rice (2002). Once all of the stellar parameters have been determined, the process is run again to check the values.

4.5.1 χ^2-Minimisation Plot for Radial Velocity

As previously noted AB Dor A is part of multiple star system with the radial velocity being affected by the orbit of its close companion AB Dor C. From previous observations, in particular Jeffers *et al.* (2006), there can be a variation of up to 3.4 km s^{-1}.

The radial velocity can be derived from the LSD profile since it is offset from the 0 km s^{-1} position by an amount equivalent to the radial velocity.

The derived value by this method was $\sim$30 km s^{-1} and this was used as

the starting value for the χ^2-minimisation determination of stellar parameters.

The impact of the multiplicity of AB Dor is most obvious in the variations of its radial velocity measurements over time. Table 4.3 shows the radial velocity measurements for AB Dor from DI studies between 1988 and 2011. The data comes from (Jeffers *et al.*, 2006) and from the 2.3-m data collected in 2009 and 2011 and presented in this thesis.

Table 4.3: AB Dor: Radial Velocity Measurements for Epochs from 1988 - 2011. Table adapted from (Jeffers *et al.*, 2006) with 2010 and 2011 2.3-m data appended.

Epoch	Radial Velocity (km s^{-1})
1988 December 16	32.2
1988 December 19	32.2
1992 January	31.2
1992 December	28.8
1993 November	29.7
1994 November	29.9
1995 December	31.4
1996 December	31.4
1998 January	31.5
1998 December	31.6
1999 December	31.8
2000 December	32.1
2001 December	32.7
2002 December	32.9
2010 January	29.8
2011 January 21-23	30.9

Using the χ^2-minimisation, as described by Petit *et al.* (2002) an initial value of 30.0 km s^{-1} was selected as based on the offset in the LSD profile and checked against previous values from Table 4.3. The radial velocity values from Jeffers *et al.* (2006) ranged from 28.8 to 32.9 km s^{-1}.

Figure 4.2 shows the χ^2-minimisation plot for the radial velocity of AB Dor for these observations, while Table 4.4 shows the list of the range of values used.

The minimum χ^2 gave a value of 30.9 km s^{-1} which is consistent with previous results for the star and errors of ± 0.5 km s^{-1} but is different from

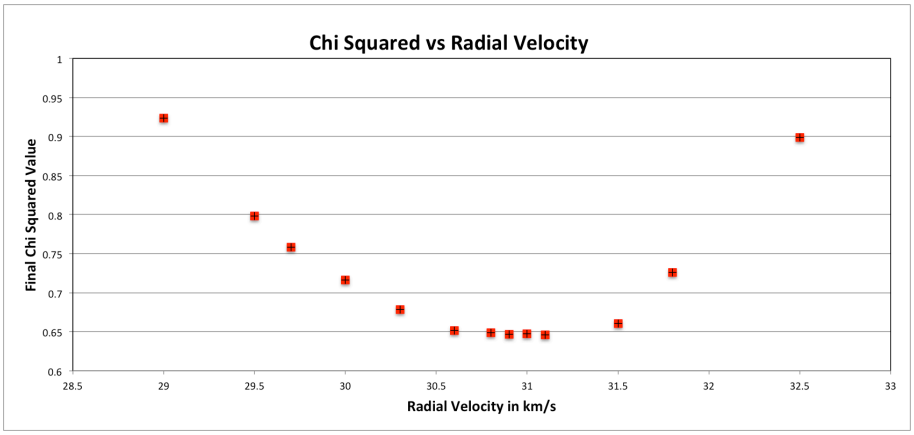

Figure 4.2: χ^2-minimisation-Plot for Radial Velocity for AB Dor Jan 2011 Observations showing 30.9 km s^{-1} as the minimum and hence the selected radial velocity.

Table 4.4: χ^2-minimisation Values for a range of Radial Velocity Values for AB Dor

Radial Velocity in km s^{-1}	29.0	30	30.6	30.8	30.9	31	31.1	31.5	32.5
Chi Squared	0.923	0.716	0.651	0.648	0.646	0.647	0.646	0.660	0.899

the value used by Jeffers *et al.* (2006).

4.5.2 χ^2-minimisation Plot for $v\sin i$

Using the χ^2-minimisation technique to refine this value produces the results in Table 4.5 and graphed in Figure 4.3. The value for the $v\sin i$ from the graph is 89.5 km s^{-1}. This is slightly higher than that used by Jeffers *et al.* (2006) but within standard error bars.

Table 4.5: χ^2 Values for a range of $v\sin i$ Values for AB Dor

$v\sin i$	88.5	88.9	89	89.2	89.3	89.5	89.6	90	91.5
Chi Squared	0.924	0.716	0.678	0.652	0.649	0.646	0.647	0.660	0.899

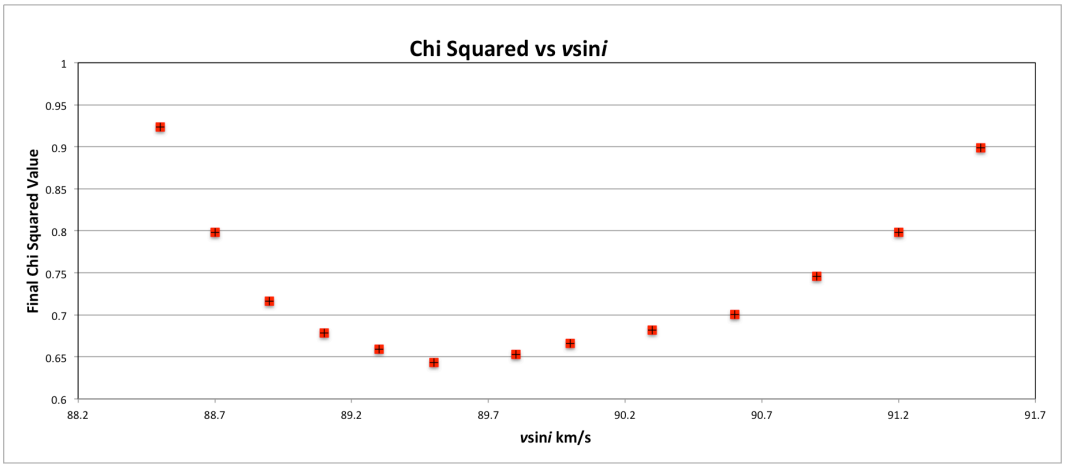

Figure 4.3: χ^2-minimisation for the $v\sin i$ for AB Dor Jan 2011 Observations

4.5.3 χ^2-minimisation Plot for Stellar Inclination Angle (i)

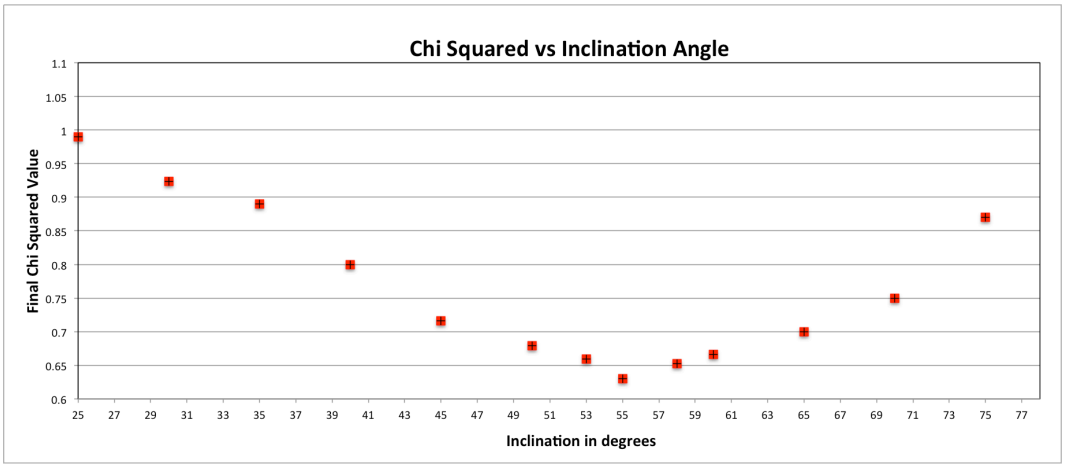

Figure 4.4: χ^2-minimisation for the Stellar Inclination Angle (i) Values for AB Dor Jan 2011 Observations giving a minimum value of 55°.

Table 4.6: χ^2-minimisation Values for a range of Stellar Inclination Angle (i) Values for AB Dor

Inclination Angle	25	35	40	45	50	55	60	65	75
Chi Squared	0.99	0.89	0.83	0.72	0.68	0.63	0.67	0.705	0.87

4.6 Calculating Values for Stellar Parameters Using Radius and Period

4.6.1 Calculating $v\sin i$ using the Stellar Radius and Period

$v\sin i$ can be calculated using the formula:

$$v \sin i = \frac{2\pi R}{P} \tag{4.4}$$

Where: R = the stellar radius (in solar radii); P = Period of the star = 0.51479 days and R$\odot$= 6.955 $\times$ (10^5 km.)

There are 2 values for the radius of AB Dor A in literature: 0.86 $R_\odot$ and 1.1 $R_\odot$. Jeffers *et al.* (2006); Strassmeier (2009) suggest AB Dor A has a radius of 1.1 $R_\odot$.

$v\sin\ i = ((2\pi) \times (1.1) \times (695500))/((0.51479) \times (86400))$

$v\sin\ i = (4806950.9192)/(44477.856)$

$v\sin\ i = 108.08$ km s^{-1}

This value is obviously very high and does not match up with any other measurements. Since $v\sin i$ can also be estimated from the line span logs and measuring the LSD profile. Both these methods do not validate the above result.

Maggio *et al.* (2000) suggest AB Dor A has a radius of 0.86 $R_\odot$.

$v\sin i = ((2\pi) \times (0.86) \times (695500))/((0.51479) \times (86400))$

$vsini = (3758161.6279)/(44477.856)$

$vsini = 84.49 kms^{-1}$

This value is more realistic and fits in with both the LSD profile and previous results from literature and would also suggest that the radius of AB Dor is the lower of the two values and not that put forward in Torrees et al (2006) and Strassmeier et al (2009).

Using the χ^2-minimisation technique to refine the value produces the results in Table 4.5 and graphed in Figure 4.3. The value for the $v\sin i$ from the graph is 89.5 km s^{-1}. This is slightly higher than that used by Jeffers *et al.* (2006) but within standard error bars.

4.6.2 Calculating Inclination Angle (i) from $v$sini, Stellar Radius and Period

$$i = \arcsin \frac{P.vsini}{2\pi R} \tag{4.5}$$

Where: i is the inclination angle ;
P is the rotational period;
$v\sin i$ is the rotational velocity; and
R is the stellar radius.

Using the equation again with the values:
P = 0.51479-d
$v\sin i$=84.5 km s^{-1}
R = 0.86R$_\odot$ and

$$i = \arcsin(((0.51479) \times (86400) \times (84.49))/((2\pi) \times (0.86) \times (695500)))$$
$$i = \arcsin((3757934.05344)/(3758161.6279))$$
$$i = 57.3^\circ$$

This is well within error bars and also is close to the 55° which was the result of the χ^2-minimisation technique.

4.7 Summary of Derived Stellar Parameters

It can be seen from Figures 4.2, 4.3 and 4.4 that the χ^2 values are reasonably parabolic. The plots show a minimum, which is the most suitable value for the derived parameter to produce the best modelled fit to the observed data.

The final values for the stellar parameters using the χ^2-minimisation technique are:
Radial velocity: 30.9 km s^{-1}
$v\sin i$: 89.5 km s^{-1} and
Stellar Inclination Angle i: 55°.

These compare well to the values from the literature (Table 4.7). The $v\sin i$ and i value are within the standard error bars, while the radial velocity value is within the range of radial velocities for this star (Table 4.3).

4.8 AB Dor Surface Features

4.8.1 2.3-m Map

The surface brightness images used in this thesis are reconstructed using the maximum entropy code of Brown *et al.* (1991) and Donati and Collier-Cameron (1997) which incorporate the brightness model of Collier-Cameron (1992) and the spot occupancy model where each point on the stellar surface is quantified by the local fraction of the stellar surface occupied by spots. The range of spot occupancy is from 0, where there are no spots present, to 1, where there is maximum spottedness (Collier-Cameron, 1992).

The surface features of AB Dor here have been derived using the maximum entropy code *ZDICam* as described in Section 3.5.12

The software reconstructs the minimum amount of features to fit the observed data, which can lead to a slight underestimate of the spot occupancy. Observations that have a low spectral resolution can possibly have less reconstructed spots and this is potentially an issue with the 2.3-m and its echelle spectrograph with its much lower resolution than the AAT. This problem can be minimised, however, by having data with a high signal-to-noise.

To minimise the issue noted by Marsden *et al.* (2005) and Mengel (2005), where the software introduces artefacts into the final map in the case of incomplete phase coverage the three nights of data are combined into a single dataset.

The phase coverage of the map from the 2.3-m has no observations between phases 0.35 and 0.70 which is ∼33% of the rotational period.

4.8.2 AAT Map

The 2002 AAT maps (Figure 4.12 and 4.13) that are being used for comparison are only missing the phases between 0.05 and 0.22 with multiple exposures for the rest of the phases.

This 2002 DI map is the closest epoch map that was available from any source we could find. Even though the map is more than ten years old, it is still useful for the purposes of comparison. Since, AB Dor has been studied for many years and has been the target of DI on a number of occasions its surface features have been well documented.

In Jeffers *et al.* (2006), the temporal evolution of star-spots and differential rotation on AB Dor from 1988 to 1994 is considered but also includes data that was collected up until 2002. Using the details included in Jeffers *et al.* (2006), the 2002 AAT map and the many publications relating to AB Dor there are a number of common and consistent features across all epochs.

The first constant feature in all AB Dor observations, with the exception of the 1988.96 epoch, is that there has always been a strong polar spot. The 1988 dataset consisted, however, of 2 nights of observations and the data had quite poor signal-to-noise. Spot coverage ranges from 6.25% to 9.25% over the documented epochs. Spot coverage in the 2.3-m map (Figure 4.7) is 6.8%.

It is difficult to compare exact features due to the signal-to-noise difference, and all of the DI maps in literature are from the 3.9-m AAT, but on many of the images from literature there are numerous low-latitude spot features.

4.9 Maximum Entropy Brightness Images for AB Dor

Table 4.7 compares the stellar parameters from literature - specifically in column 1 from (Jeffers *et al.*, 2006), while in column 2 are the results of the χ^2-minimisation technique from Section 4.5 and the final column uses the derived or calculated figures from Section 4.6.

The maximum entropy images in Figures 4.7 and 4.8 use the figures from the χ^2-minimisation technique and have produced the best results. Figures 4.5

Table 4.7: Comparison of Stellar Parameters taken from Literature; from using the χ^2-minimisation technique and derived from the Stellar Parameters of Radius and Period.

Parameter Derived from	Literature Value	χ^2 χ^2-minimisation	Calculated Radius and Period
Inclination, i:	60°	55°	57.3°
$v\sin i$:	89 km s^{-1}	89.5 km s^{-1}	84.6 km s^{-1}
Photospheric Temp:	5,000 K		
Spot temperature:	3,500 K		
Radial Velocity:	29.5 km s^{-1}	30.9 km s^{-1}	30.9 km s^{-1}

and 4.6 use the input parameters from literature, while Figures 4.9 and 4.10 are the result of the derived and calculated values.

They all show a polar spot and spot features at phases 0.00, 0.10-0.35 0.75-0.80. This would indicate that these features are mostly likely real unlike the features phase 0.60 and 0.70 since there were no observations for these phases.

Comparing Figures 4.7 and 4.8 with the AAT maps (Figures 4.12 and 4.13) they are structurally very similar, with a polar cap and/or high-latitude spots, and with varying degrees of low-latitude spots. The polar spot in the 2.3-m maps is less intense but is still present. With over ten years between the maps and no information as to phase times. It is difficult to align the phasing of the maps. In the 2.3-m map there is no coverage of phases 0.34 to 0.70 and the AAT map is missing phase coverage from 0.05 to 0.22. In the other maps in the literature, over time spot features occur consistently at phases 0.15, 0.28 and 0.75, and a large unspotted area at phase 0.35. The 2.3-m maps appear to have similarly located features phasing in the various maps may differ.

In the 2.3-m image reconstructions in this section, the polar spot is not as strong and is less fragmented than those from the 2002 AAT observations. AB Dor is known to vary in the strength of its polar spot. The coverage as shown by the ticks on the outside of the polar projection map show the difference in phase coverage between both maps.

The 2.3-m image seems to have a weaker polar spot but does have some intermediate and low-latitude spot features. There are obvious spot features at phases 0.1-0.35 and 0.75-0.95. There are also similar spot grouping at the phases between 0.4 and 0.7 even though there are no tick marks above the plot and so here is no phase coverage in this region. These features between 0.1 and 0.35 phase and phase 0.75 and 0.95 as well as the small low latitude spot seem

to remain through all the testing with changing of stellar parameters which mean they are most likely real.

This first AB Dor Maximum Entropy Brightness Image map for the 2.3-m data, Figure 4.5, uses the parameters from Jeffers *et al.* (2006) and listed in the first column of Table 4.7

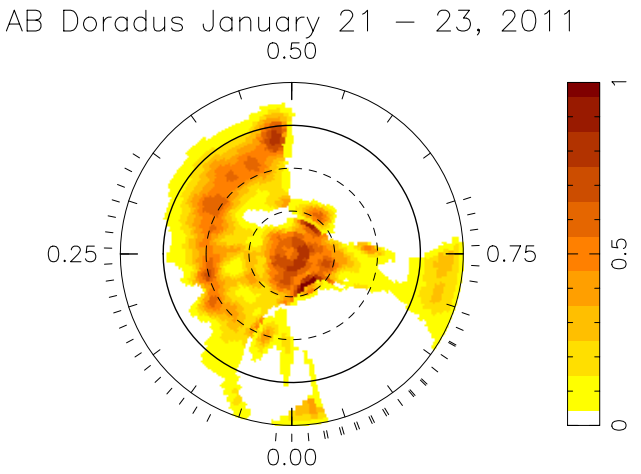

Figure 4.5: Maximum Entropy Brightness Map for AB Dor - 2.3-m - Jan 2011. The image is a flattened polar projection that extend down to -30° latitude with the thick circle as the stellar equator. The numbers and ticks surrounding the flattened stellar image represent the rotational phase and phase coverage of the data.

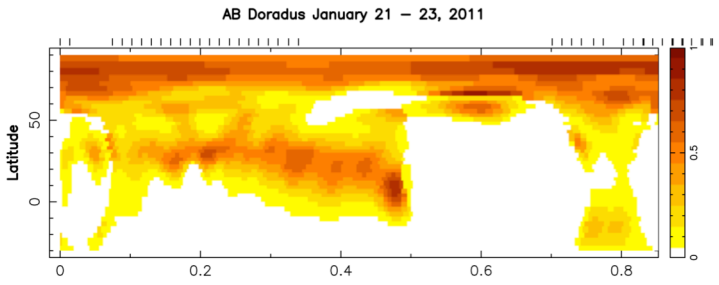

Figure 4.6: Rectangular Doppler Imaging Spot Occupancy Map - 2.3-m Jan 2011. Using parameters from the literature listed in Column 1 in Table 4.7 for AB Dor Jan 2011 Observations

This set of AB Dor Maximum Entropy Brightness Image maps for the 2.3-m data, Figures 4.7 and 4.8, use the parameters from χ^2-minimisation technique listed in Column two of Table 4.7

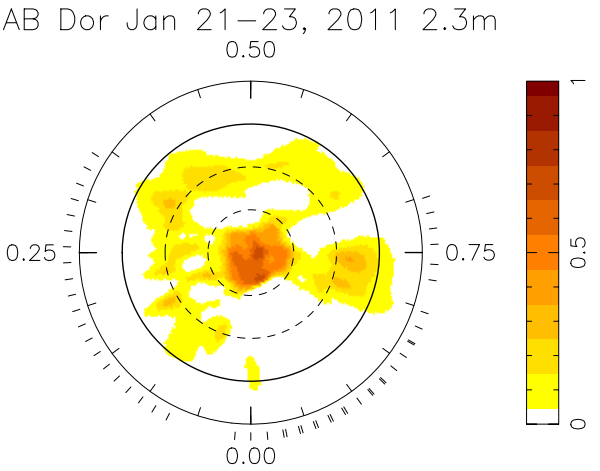

Figure 4.7: Maximum Entropy Brightness Map for AB Dor - 2.3-m - Jan 2011 using Stellar Parameters from χ^2-minimisation technique.

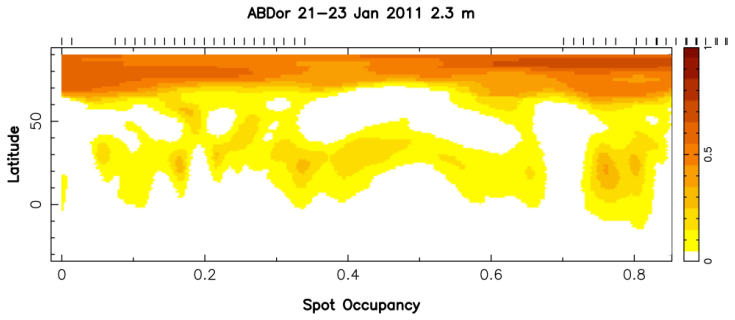

Figure 4.8: Rectangular Doppler Imaging Spot Occupancy Map - 2.3-m Jan 2011.Using Stellar Parameters from should not change between. AB Dor Jan 2011 Observations

This set of AB Dor Maximum Entropy Brightness Image maps for the 2.3-m data, Figures 4.9 and 4.10, use the parameters from Column 3 of Table 4.7

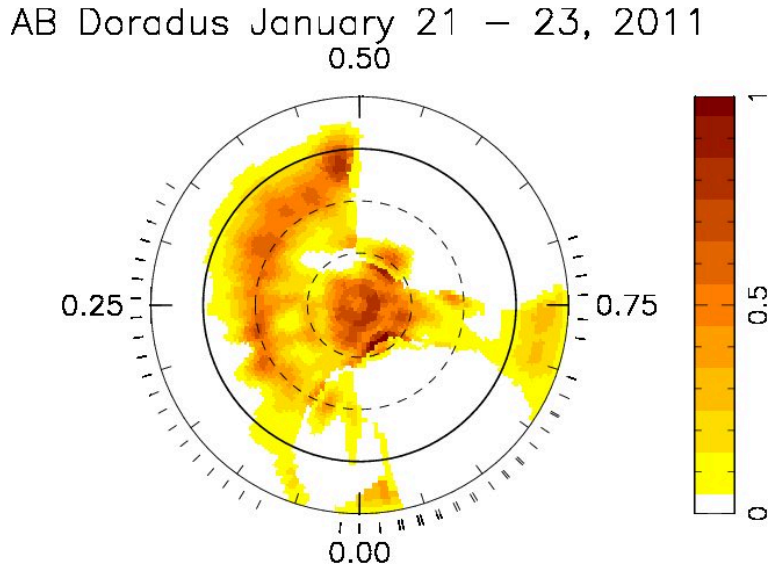

Figure 4.9: Maximum Entropy Brightness Map for AB Dor - 2.3-m - Jan 2011. The image is a flattened polar projections that extend down to -30° latitude with the thick circle as the stellar equator. The numbers and ticks surrounding the flattened stellar image represent the rotational phase and phase coverage of the data.

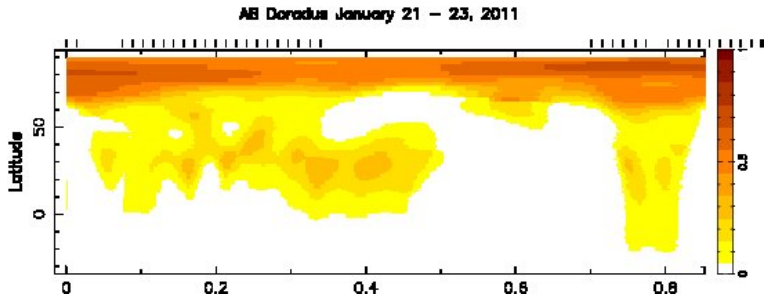

Figure 4.10: Rectangular Doppler Imaging Spot Occupancy Map - 2.3-m Jan 2011. Using parameters from Column 3 in Table 4.7 for AB Dor Jan 2011 Observations

Figure 4.11 shows the resulting modelled fits (thick line) to the observed LSD profiles (thin line). These fits are the 2.3-m data and for the map (Figure 4.7) which uses the input parameters determined from using the χ^2-minimisation technique

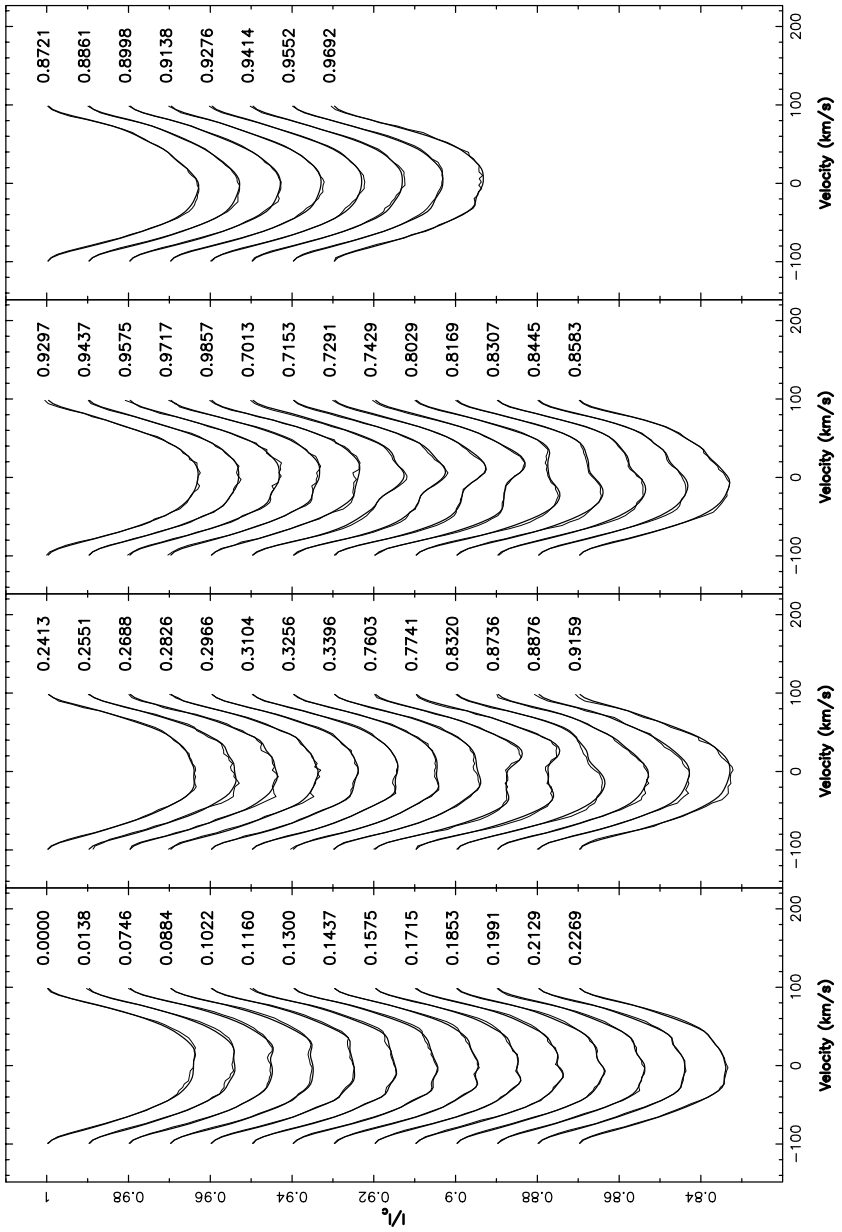

Figure 4.11: Maximum Entropy Fits to the LSD Stokes I profiles of AB Dor for January 2011.The thin lines are the observed LSD profiles, and the thick lines are the modelled profiles. The rotational phasing of each observation is listed to the right of each profile. Each successive image is shifted for graphical purposes. The fits are equivalent to a $\chi^2{}_{aim}$ of 0.3.

4.9.1 AAT Maximum Entropy Brightness Map for AB Dor

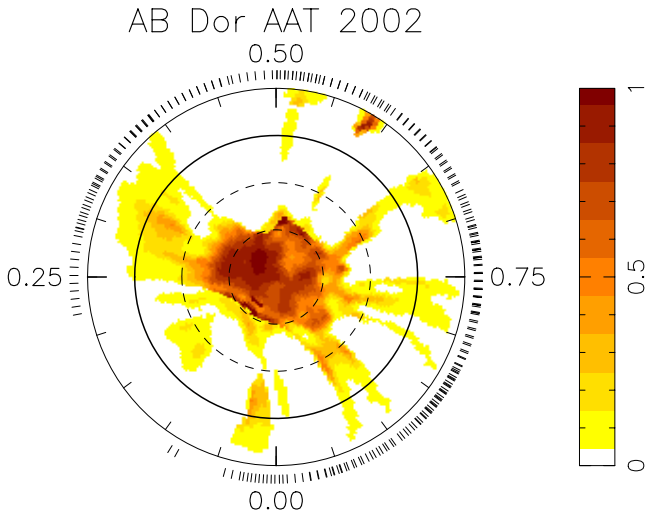

Figure 4.12: Maximum Entropy Brightness Map for AB Dor - AAT-2002. The image is a flattened polar projections that extend down to -30° latitude with the thick circle as the stellar equator. The numbers and ticks surrounding the flattened stellar image represent the rotational phase and phase coverage of the data.

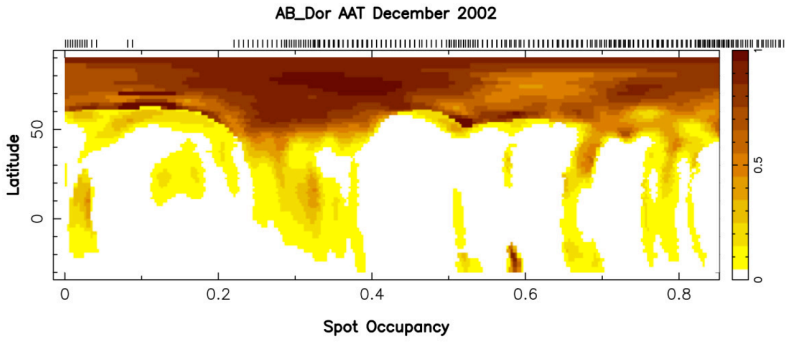

Figure 4.13: A Rectangular Doppler Imaging Spot Occupancy Map for AB Dor - AAT-2002

4.10 Fractional Spottedness

The observed distribution of spot features with latitude on active young stars provides for a comparison with the predictions of stellar dynamo theory. Certainly, the evidence from literature and from these results suggest that active young stars show evidence of a polar spot as well as detectable lower latitude features. The presence of polar spots has proven to be a challenge for dynamo theories. There are currently two main theories as to their cause. The first is the presence of an interface-layer dynamo, such as that believed to be operating in the Sun today, but with a significantly stronger element of meridional flow primarily due to the rapid stellar rotation. The second theory is the idea that there exists a distributed dynamo that is acting across the entire stellar convection zone. Marsden *et al.* (2011) suggests that it is possible that a combination of both these two processes may be occurring. The precise distribution of spot size and latitude on the star offers a way to help decide between the above interface-layer and distributed dynamo models. Therefore, a plot of spottedness with latitude will be useful in this regard. Here, this plot has been presented in two ways. Figure 4.14 shows a rectangular plot of the spot occupancy map for the 2.3-m data which show the latitudes at which the spot occupancy of the targets are most evident and Figure 4.15 which shows a plot of spottedness versus latitude to numerically show the extent of the percentage spottedness over the surface of the stars.

It can be seen clearly that the majority of the spot occupancy is confined to the polar region from around 60-80°. Lower latitude features are also seen to appear at approximately 10-30°.

Fractional spottedness is the variation of spot occupancy with stellar latitude. From Marsden *et al.* (2005) it is defined as:

$$F(\theta) = \frac{S(\theta)\cos(\theta)d(\theta)}{2} \tag{4.6}$$

Where S(θ) is the average spot occupancy;θ is the latitude; and d(θ) is the latitude width of each latitude ring.

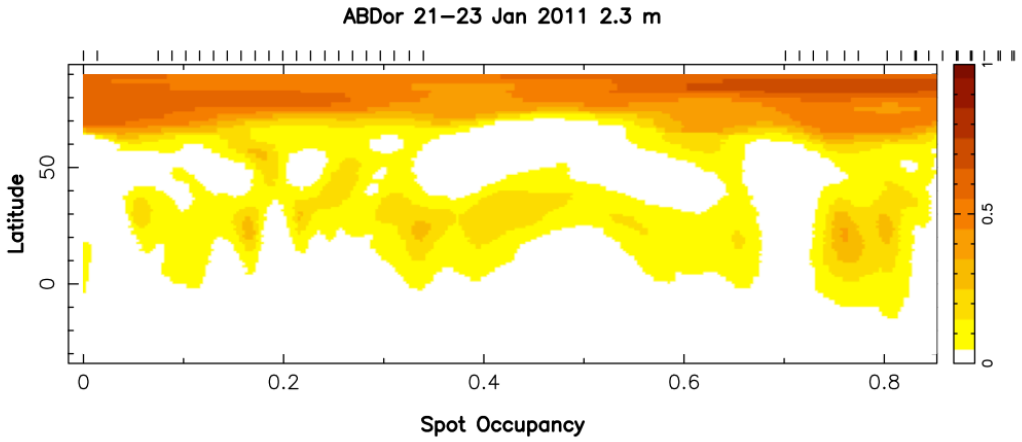

Figure 4.14: Rectangular Doppler Imaging Spot Occupancy Map - 2.3-m Jan 2011. It can be seen clearly that the majority of the spot occupancy is confined to the polar region. Lower latitude features are also seen to appear at approximately 10-30° for AB Dor Jan 2011 Observations

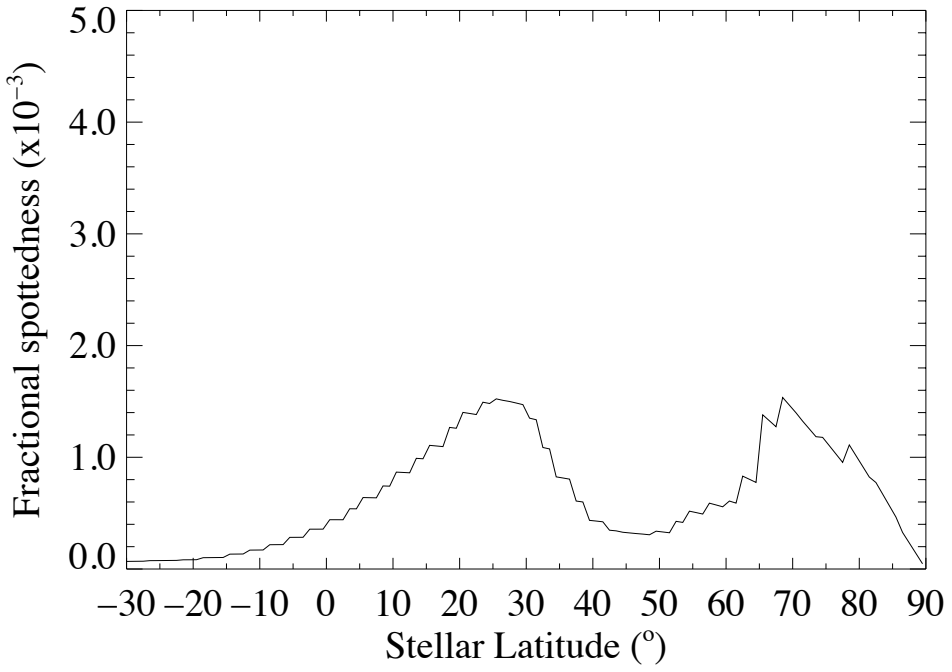

Figure 4.15: Plot of surface spot occupancy as a function of latitude for AB Dor January 2011 dataset. Seen here are the two maxima in spot occupancy at latitude 10-30° and near the pole of the star 60-80° that are also visible in Figure 4.8. The fractional spottedness for both these two maxima corresponds to ∼0.12% each.

4.11 Tests of Robustness

The following Figures 4.16, 4.17 and 4.18 provide a graphical representation of the importance of getting the stellar input parameters correct. The stellar parameters of radial velocity, $v\sin i$ and inclination angle are presented on spot occupancy maps that have been reconstructed for the January 2011, AB Dor data using ZDICam.

The purpose of the exercise is to demonstrate what happens to the result when incorrect inputs of the stellar parameters are used. The variation of the parameters are given within the error bars of the original values, where radial velocity is 29.5±1.5 km s^{-1}, and $v\sin i$ is 89.0±1.0 km s^{-1} and inclination angle 60°±5°. By considering the effect on the resulting spot occupancy map of the determined stellar parameters of radial velocity and $v\sin i$ as well as inclination angle, the accuracy of the values as well as the maps, can be established.

In all three figures map (b) is the original map with the parameters determined through the χ^2-minimisation technique. It is evident in the figures that both the radial velocity and the $v\sin i$ values alter the structure of the resulting spot occupancy maps, however the radial velocity affect on the stellar surface features is minimal.

The $v\sin i$ values change the appearance of the reconstructed spot occupancy maps.(Figure 4.17) In particular, equatorial smearing of the spot features becomes apparent when the $v\sin i$ value is at its upper limit.

What is apparent is that the features in the original map such as the polar spot, the large equatorial feature at phase 0.75-0.80, the small low latitude feature near phase 0 and the feature at phases 10-20 are there in all the variations. This demonstrates the robustness of the technique and that these features are most likely real and not artefacts. The feature, however, at phase 60-70 is most likely an artefact as there were no observations for that time and as such it is difficult to reconstruct spots at such a phase. Figure 4.16 is a graphical representation of the effect that varying the radial velocity values on the AB Dor spot occupancy maps reconstructed using *ZDICam*. Note that there is little effect on the resultant spot occupancy map due to the varying radial velocity value in coverage but the lower radial velocity value differs in intensity.

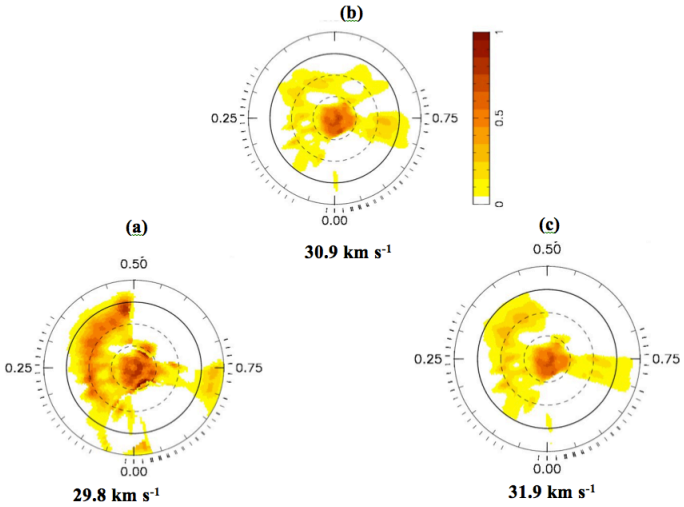

Figure 4.16: Spot Occupancy Maps of AB Dor for Radial Velocity (a) 29.8 km s^{-1}, (b) 30.9 km s^{-1}, and (c) 31.9 km s^{-1}. The images are flattened polar projections that extend down to -30° latitude with the thick circle as the stellar equator. The numbers and ticks surrounding the flattened stellar images, respectively, represent the rotational phase and phase coverage of the data.

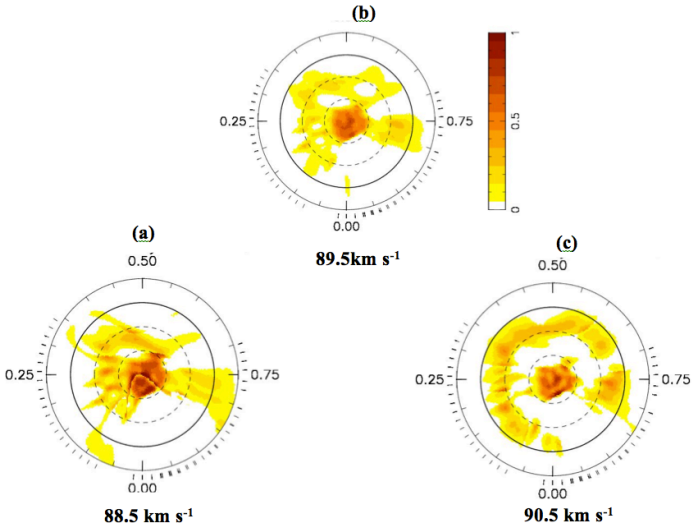

Figure 4.17: Spot Occupancy Maps of AB Dor for $v\sin i$ measurements (a) 88.5 km s^{-1}, (b) 89.5 km s^{-1}, and (c) 90.5 km s^{-1}. The images are flattened polar projections that extend down to -30° latitude with the thick circle as the stellar equator. The rotational phase and phase coverage of the data are represented by the numbers and ticks surrounding the flattened stellar images, respectively. Note the effect that the $v\sin i$ has on the resultant spot occupancy map, where the higher the $v\sin i$ the more spots the code uses to fit the observed data. It is also seen that when the$v\sin i$ is increased, that equatorial smearing becomes apparent.

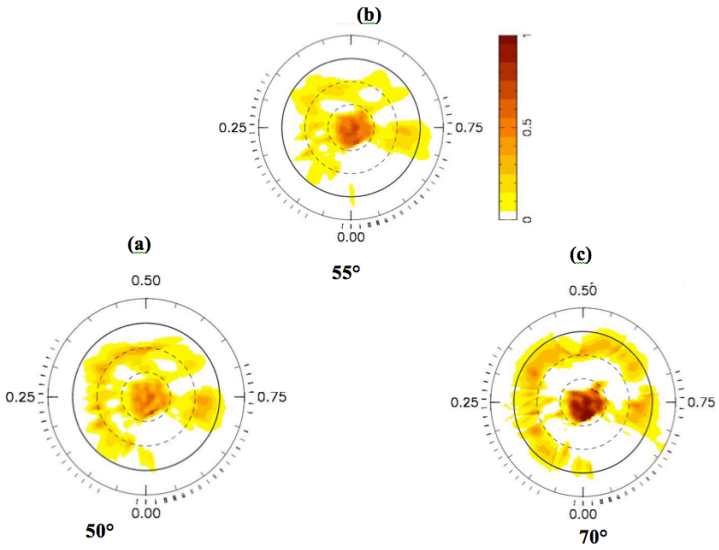

Figure 4.18: Spot Occupancy Maps of 2.3-m AB Dor data for inclination angles (a) 50° (b) 55°, and (c) 70°. The images are flattened polar projections that extend down to -30° latitude with the thick circle as the stellar equator. The numbers and ticks surrounding the flattened stellar images, respectively, represent the rotational phase and phase coverage of the data. Note the effect that the inclination angle has on the resultant spot occupancy map.

In Figure 4.17 (c) a small amount of equatorial smearing of the lower latitude features is present when the $v\sin i$ is increased.

Figure 4.18 presents an inclination angle comparison illustrating the effect that varying the inclination value has on the resulting Doppler Imaging map. These spot occupancy maps of AB Dor's stellar surface for inclination angles of (a) 50° (b) 55° (from χ^2-minimisation technique), and (c) 70°. All reconstructed images produce similar outputs, with an increase in spot numbers with an increase in inclination angle. It is clearly seen here that the higher the inclination angle, the more spots are fitted to the observed data, especially at the lower latitudes. Also, the higher the inclination angle, the more the polar spot feature appears filled in. This is due to the amount of filling required by the model to fit the data as the star is rotated more pole-on to the line of sight of the observation.

Consistent features throughout all three inclination angles are the polar spot, mid to low latitude features at phases 0.10-0.20 and 0.75-0.80 and the individual lower latitude feature at $\sim$ 0.00.

These previous examples show what happens to the result determined

through the Doppler Imaging method when incorrect inputs of the stellar parameters are used. It is evident in the figures that entering incorrect stellar inclination, radial velocity or $v\sin i$ values alter the structure of the resulting spot occupancy maps, however radial velocity has the least effect on the stellar surface features while Stellar inclination angle has the most effect.

4.12 Conclusions

The surface features of AB Dor have been examined and compared to those in the 2002 AAT DI map as well as to others in literature. There are sufficient common features between the two and between the 2.3-m map and other maps in the literature so show the 23-m is capable of doing Doppler Imaging.

Piskunov *et al.* (1990) suggest that to accurately compare the spot coverage, the spatial resolution is important. The smaller aperture and echelle spectrograph with less resolution means that the maps created from this data will have less spots resolved than those from the AAT or in literature.

Other factors also impact the level of spottedness. For example, the southern hemisphere of a target is very difficult to reconstruct due to the limb darkening effect that masks all but very dark or large features. Also, features below $\sim -60^{\circ}$ cannot be seen at all due to the inclination angle of the star. Yet another reason for the underestimation of the spot coverage output from Doppler Imaging is the inability of the software to resolve uniform spot distributions since it is only sensitive to large asymmetric spot distributions.

So, overall the level of spottedness which is possibly only different by 1-1.5% in the 2.3-m data is not a critical issue in whether or not the 2.3-m can do scientifically useful DI work. The 2.3-m has produced a DI map of AB Dor that shows all major features which have been consistent over the many years of observations of this active young star. It not only shows the prominent polar spot but lower latitude features as well. In the future, with ongoing studies of this star, differential rotation measurements and monitoring for possible cycles will add to the knowledge of how dynamos work in these active young solar analogues. Thus the 2.3-m is useful for DI.

Chapter 5

Simultaneous Doppler Imaging of HIP43720 (HD76298) with the ANU 2.3-metre Telescope and the AAT

5.1 Introduction

In April 2010, time was allocated on the AAT for a ZDI program looking at various stars including HIP43720. Time on the 2.3-m was applied for to allow contemporaneous observing of this G1 star (a suitable target for the 2.3-m). This was to enable a direct comparison of Doppler Map observations of the same star taken with the different telescopes at the same time.

As discussed in Chapter 4, Doppler Imaging of a bright, rapidly-rotating target such as AB Dor was considered to be possible with the 2.3-m telescope. However, to understand how scientifically useful the telescope and its echelle spectrograph would be in an ongoing project to undertake stellar dynamo surveys using DI, it was important to test the setup further. HIP43720 is a star which was considered to be at the theoretical limits for the 2.3-m telescope. This star would present a greater challenge as it has a fainter magnitude and lower rotational velocity, $v\sin i$, although its longer rotational period would be beneficial as it allows for longer exposures to counter the fainter magnitude. The application for time was successful and simultaneous observations on both the AAT and 2.3-m telescope were undertaken on April 1-5. 2010.

5.2 2.3-metre Observations

Observations of HIP43720, using the 2.3-m were taken on April 1–5, 2010 inclusive. No data from April 4th was included due to the observations having been taken through cloud resulting in the signal-to-noise being too low to be usable.

Over the rest of the observing run, 32 usable 1800-second exposures of HIP43720 were taken. The exposure time, of 1800 seconds is approximately 2.4% of the rotation period. This length of exposure was necessary to get a high enough signal-to-noise value to undertake effective Doppler Imaging of this faint target with a $V_{mag} = 9.09$ (Hog *et al.*, 2000) on the smaller aperture telescope.

As discussed previously, for effective DI it is preferable to keep exposures to a time period of no more than 2% of the rotational period. It is a compromise, balancing the need for longer exposures against the need to reduce phase smearing due to the stellar rotational rate.

One potential issue for the observations was the lower $v\sin i$ at 39 km s^{-1}. This is important as it affects the ability to resolve spatial elements on the stellar surface. So, although it had been ascertained that DI could be carried out on the brighter, faster AB Dor, HIP43720 with its lower $v\sin i$ would present a real test of the telescope and instrument capabilities in this field due to the low resolution of the echelle.

The setup of the 2.3-metre telescope and the echelle instrument is discussed in detail in Chapter 3.4. The mean pixel resolution of the 2.3-m spectra was determined to be 4.110 km s^{-1} pixel^{-1}. Seeing during the 5 night run ranged from 2.5 to 4.5 arc seconds. The log of the of the 2.3-m observations is shown in Table 5.1.

5.3 Anglo-Australian Telescope (AAT)

The 3.9-m Anglo-Australian Telescope (AAT), also located at Siding Spring Observatory, was used to obtain the comparison set of observations on HIP43720.

Table 5.1: HIP43720 - Observation Log 2.3-m Telescope April 2010. The phase is based on a rotational period of 3.14 days with the zero phase set to the middle of the run. The observations therefore spanned over just over 1 complete rotation of HIP43720.

UT Date	Exposure Number	Exposure Time	UT Start	Phase	LSD SNR
2010, Apr 01	34	1800	09:22:59	-0.6602	904
2010, Apr 01	35	1800	10:02:46	-0.6514	901
2010, Apr 01	36	1800	10:32:45	-0.6447	896
2010, Apr 01	37	1800	11:03:09	-0.638	900
2010, Apr 01	38	1800	11:33:25	-0.6313	902
2010, Apr 01	41	1800	12:56:06	-0.613	895
2010, Apr 01	42	1800	13:26:23	-0.6063	930
2010, Apr 02	23	1800	08:56:36	-0.3475	908
2010, Apr 02	24	1800	09:27:31	-0.3407	900
2010, Apr 02	25	1800	09:57:47	-0.334	913
2010, Apr 02	26	1800	10:28:22	-0.3272	902
2010, Apr 02	27	1800	10:58:37	-0.3205	911
2010, Apr 02	28	1800	11:30:37	-0.3134	912
2010, Apr 02	29	1800	12:00:54	-0.3067	910
2010, Apr 02	32	1800	13:34:44	-0.286	907
2010, Apr 02	33	1800	14:05:01	-0.2793	904
2010, Apr 03	39	1800	08:52:54	-0.0299	670
2010, Apr 03	40	1800	09:23:13	-0.0232	753
2010, Apr 03	41	1800	09:53:35	-0.0164	693
2010, Apr 03	42	1800	10:23:49	-0.0098	708
2010, Apr 03	43	1800	10:54:09	-0.003	692
2010, Apr 03	44	1800	11:24:25	0.0036	671
2010, Apr 03	45	1800	12:01:09	0.0117	690
2010, Apr 03	46	1800	12:31:25	0.0184	772
2010, Apr 03	49	1800	13:49:46	0.0357	765
2010, Apr 05	25	1800	09:51:41	0.62	848
2010, Apr 05	26	1800	10:02:46	0.6267	878
2010, Apr 05	27	1800	10:52:15	0.6334	869
2010, Apr 05	28	1800	11:22:32	0.6401	869
2010, Apr 05	29	1800	11:52:48	0.6467	842
2010, Apr 05	30	1800	12:23:12	0.6535	861
2010, Apr 05	31	1800	12:53:28	0.6601	864

5.3.1 Telescope Instrumentation

The high resolution spectrograph used was the University College London Echelle Spectrograph (UCLES), which is a Coudé Echelle Spectrograph. The combination of the AAT and UCLES has the ability to yield spectral resolutions as high as 100,000, however this is reduced when using the Semel Polarimeter, a visitor instrument mounted at the f/8 Cassegrain focus (Semel, 1989; Donati *et al.*, 2003a). UCLES receives light from the telescope via a fibre feed and operates at the f/36 coudé focus (Waite *et al.*, 2011).

UCLES is a high resolution spectrograph that provides the wavelength coverage needed for Doppler Imaging. For the April 2010 data set, the detector used was the English Electric Valve (EEV2) Charge Coupled Device (CCD). The EEV2 has a pixel array of 2048 (horizontal) x 4096 (vertical) 13.5 µm square pixels. A grating of 31.6 groove mm^{-1} was used for all runs. This ensures full wavelength coverage on the reduced window of the CCD in a single exposure, typically covering 46 orders (orders #84 to #129). The central wavelength was 5220.02Å with full wavelength coverage from 4377.1Å to 6815.6Å. The dispersion of ∼0.04958Å at order# 129 was achieved giving an approximate resolution across the detector of ∼71000. Waite *et al.* (2011)

For a more detailed explanation of the instrumental setup for Zeeman Doppler Imaging at the AAT see (Donati and Collier-Cameron, 1997; Donati *et al.*, 1999, 2003a).

5.3.2 AAT Observations

Spectropolarimetric observations of HIP 43720 were obtained over a 10 night period from the 25th of March - 5th of April, 2010.

The data from the AAT was kindly supplied by Ian Waite. Ian also undertook the calibration and data reduction of the AAT data, using the ESpRIT package and produced the spot occupancy maps for comparison use here.

A log of the observations are included in Table 5.2. The nights of April 1-5 coincide with the 2.3-m observations. Two sets of Maximum Entropy Brightness Images are produced. The first set covers the part of the AAT run which was undertaken on the same nights as the 2.3-m data and the second set with all nights included for comparison purposes. Exposure times were 800 seconds each and were done in sequences of 4 × 800 secs.

Table 5.2: Log of Spectropolarimetric Observations of HIP43720 - 3.9-m AAT - March 25-April 5, April 2010 (Waite *et al.*, 2012). The UT end is the time when the final exposure for HIP 43720 was completed. Each sequence consisted of 4 × 800 seconds exposures except for the final sequence on March 28th which was only 2 × 800 seconds.

UT Date	UT Begin	UT End	Number of usable Sequences
2010 March 25	10:17:59	11:15:36	1
2010 March 26	09:18:28	13:34:18	2
2010 March 27	08:45:16	14:19:41	2
2010 March 28	08:34:42	13:59:52	6
2010 March 29	09:02:47	11:40:03	2
2010 March 31	10:37:07	12:34:17	1
2010 April 01	08:58:00	09:55:44	1
2010 April 02	08:39:07	11:27:03	2
2010 April 03	08:43:34	12:30:24	2
2010 April 04	12:46:21	13:34:05	1
2010 April 05	08:31:28	09:29:14	1

The mean pixel resolution of the AAT spectra was determined to be 1.689 km s^{-1} $pixel^{-1}$.

5.4 HIP43720: Stellar Parameters

HIP43720 is a single G1V sub giant pre-main sequence star in Pyxis with a $v\sin i$ of 39.5 km s^{-1} and a rotational period of 3.14 d (Waite *et al.*, 2011).

The physical parameters, given by Waite *et al.* (2012) for HIP43720 and listed in Table 5.3 were used initially to create a map to verify if it could be done. After confirming that a DI map could be made then it was decided to identify what parameters could be determined from the 2.3-m data and compare them with those found with AAT data.

Figure 5.1 is an AAT/SDSS image from the Simbad Astronomical database used as a finder chart for HIP43720.

Table 5.3: Table of the Parameters of HIP437200 (Waite *et al.*, 2012)

Equatorial Period	3.14±0.1 days
Inclination Angle(i)	55±5°
Projected Rotational Velocity ($v\sin i$)	39.5±0.5 km s^{-1}
Photospheric Temperature (T_{phot})	6000±30 K
Spot Temperature, (T_{spot})	4100±30 K
Radial Velocity, v_{rad}	2.4±0.1 km s^{-1}
Stellar radius	3.0R$\odot$

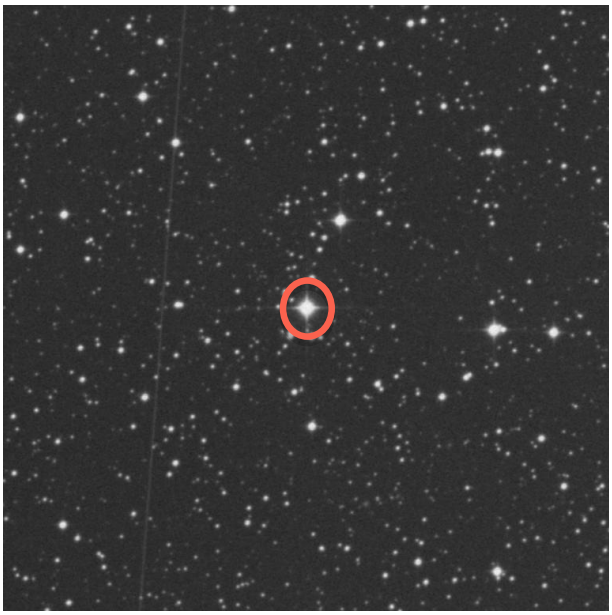

Figure 5.1: Finder Chart for HIP43720.

5.5 Surface Features

As discussed in Chapter 4.5, a χ^2-minimisation technique was employed, to determine the parameters to be used in the maximum entropy reconstruction Barnes *et al.* (2000).

For the purpose of the comparison of the AAT and 2.3-m data the same parameters as listed in Table 5.3 have initially been used. The maps in Figure 5.2 and 5.3 are surface temperature maps presenting as a maximum entropy brightness image from the combined April 1-5, 2010 data. The image is presented as a flattened polar projection.
The radial ticks outside the plot give the phases of observation. The dotted circles from the centre are latitudes of $+60°$ and $+30°$, the solid circle is the equator and the outside circle extends to $-30°$. The coloured bar indicates a gradation of spottedness with 0 (absent) to 1 (complete spots).

The resultant maximum entropy image reconstruction of the spot distribution of HIP43720 is shown in Figure 5.2. This image is based on data from the 1^{st} to 5^{th} of April 2010 inclusive.

This is then compared to maximum entropy brightness image for the observations undertaken at the AAT (Figure 5.3). Since the question this thesis is attempting to answer is whether the ANU 2.3-m telescope and echelle spectrograph can do scientifically useful Doppler Imaging work, the results of these comparisons are important.

5.6 Comparison Maps for HIP43720 - using the AAT and 2.3-m

The first set of AAT results, i.e. those in Figure 5.3 contain only those observations, twelve in total, which were taken during the same time span as the 2.3-m observations (i.e. 1-5 April, 2010). The observations on the AAT are 800 second exposures as the AAT is a 3.9-m telescope as opposed to a 2.3-m telescope with a poor throughput echelle spectrograph. However, there is sufficient detail in each map to see that they do correlate well, at least for the major features with the 2.3-m map showing a similar polar spot and lower latitude detail.

As a further comparison, Figure 5.5 shows a rectangular Doppler Imaging Spot Occupancy Map of the AAT reduced data set as in Figure 5.3 displayed from a different projection. It can be seen clearly that the majority of the spot occupancy is confined to the polar region. Lower latitude features are also seen at approximately 20-30°. Figure 5.6 shows a plot of surface spot occupancy as

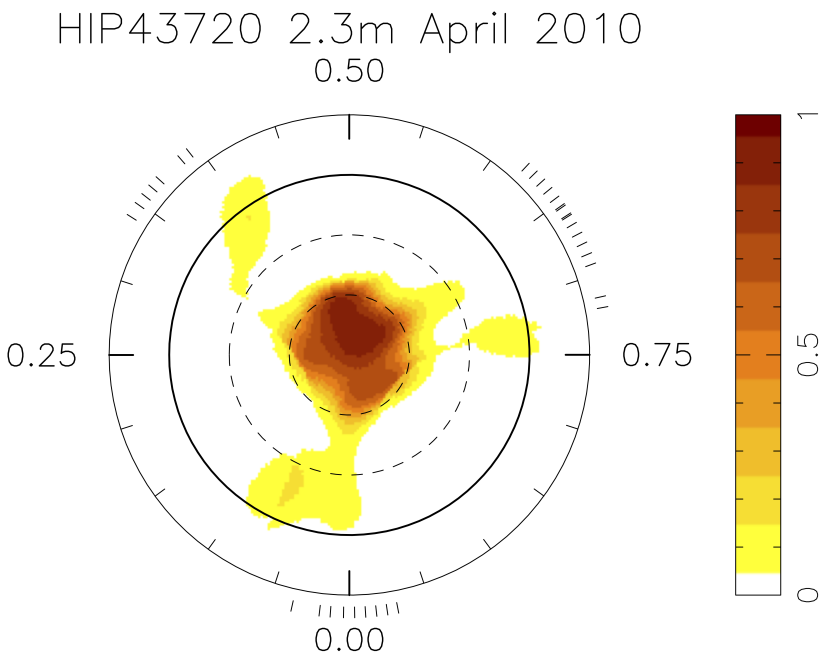

Figure 5.2: Maximum Entropy Brightness Image Combined for HIP43720 from April 1–5, 2010 on the 2.3-m . The image is a flattened polar projection. The radial ticks outside the plot give the phases of observation. The dotted circles from the centre are latitudes of +60° and +30°, the complete circle is the equator and the outside circle extends to -30°. The coloured bar indicates a gradation of spottedness with 0 (absent) to 1 (most intense)

a function of latitude for HIP43720 April 2010 AAT data set. Seen here is the main maximum in spot occupancy at latitude 25°, with a further maximum near the pole of the star (70°). The peak fractional spottedness for these two maxima correspond to $\sim$ 0.02% and $\sim$0.24%, respectively.

The 2.3-m data in the same projection is shown in Figure 5.7 while the fractional spottedness is shown in Figure 5.8 does not vary too much in latitude but shows a higher spottedness level at the peak. Just like the solar butterfly diagram helps define the dynamo operation of the Sun, a latitude distribution plot can assist in identifying the kind of dynamo that may be operating in these active young solar type stars. These fractional spottedness plots are created following the technique in (Marsden *et al.*, 2005). The plots are presented as rectangular plots of the spot occupancy maps for HIP43720 for both the AAT and 2.3-m data and they show clearly the latitudes at which the spot

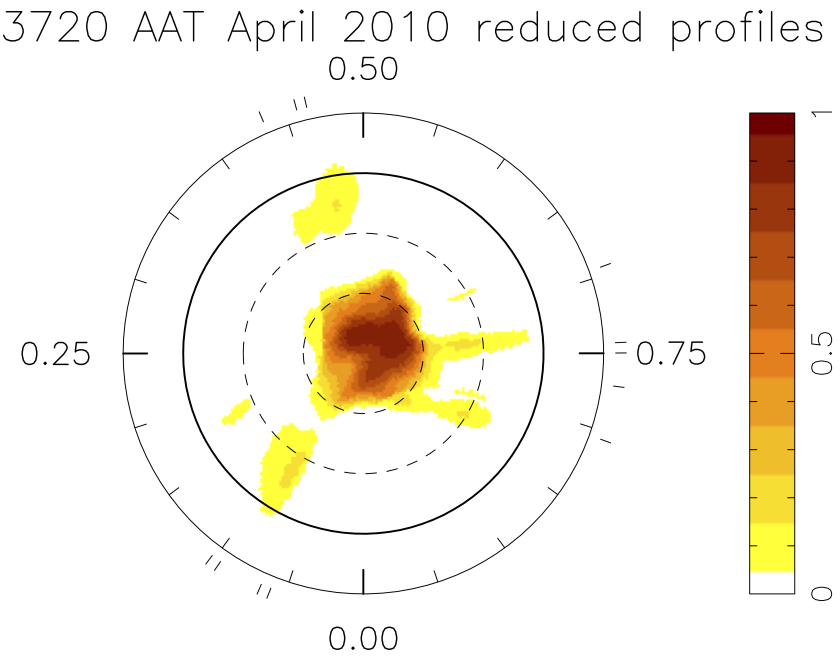

Figure 5.3: Maximum Entropy Brightness Image Combined for HIP43720 on the AAT - flattened polar projection with the figure as explained in Figure 5.2 using data from April 1-5, 2010.

occupancy of the targets are most evident, in this case from 50 -80°. The lower latitude activity is visible as small light areas on both plots.

Maximum entropy fits to the LSD Stokes I profiles of HIP43720 for 32 exposures on 1, 2, 3 and 5 April 2010 are given in Figure 5.4. These fits relate to Figure 5.10, the 2.3-m Maximum Entropy Brightness map using the χ^2-minimisation technique. There are thin lines representing the observed profiles and thick lines are the fits produced by the Doppler Imaging code. Each successive image is shifted for graphical purposes. The number to the right of each profile is the rotational phase of the observation.

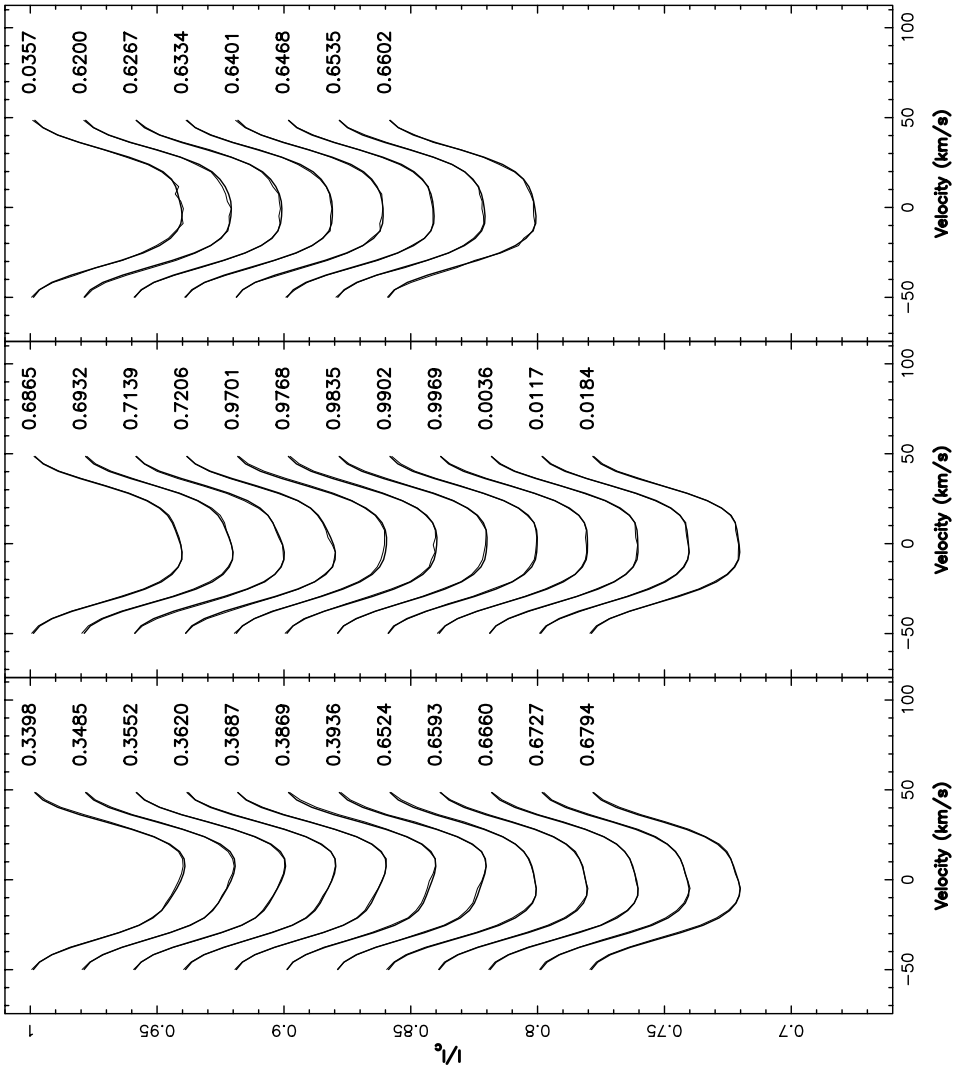

Figure 5.4: Maximum entropy fits to the observed LSD profiles of HIP43720 on 2.3-m in April 2010. The thin lines are the observed LSD profiles, and the thick lines are the modelled profiles. The rotational phasing of each observation is listed to the right of each profile.

5.7 HIP43720 - AAT Maximum Entropy Brightness Maps

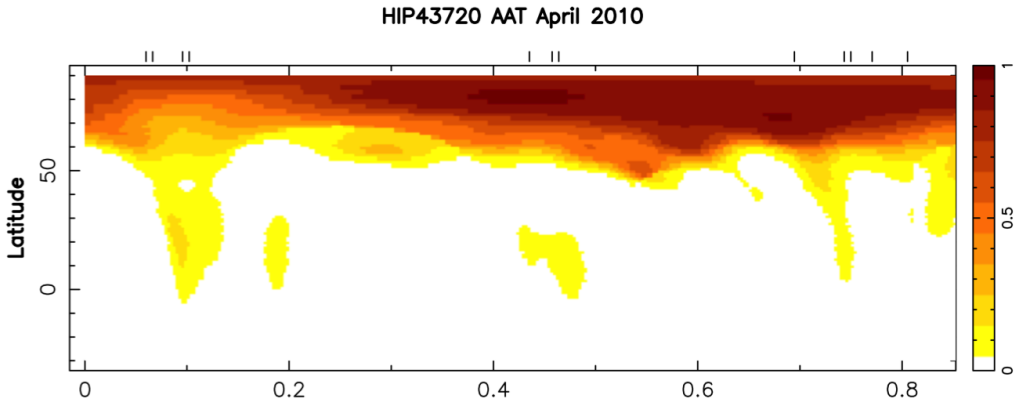

Figure 5.5: Rectangular AAT Doppler Imaging Spot Occupancy Map of HIP43720 April 2010 data set.

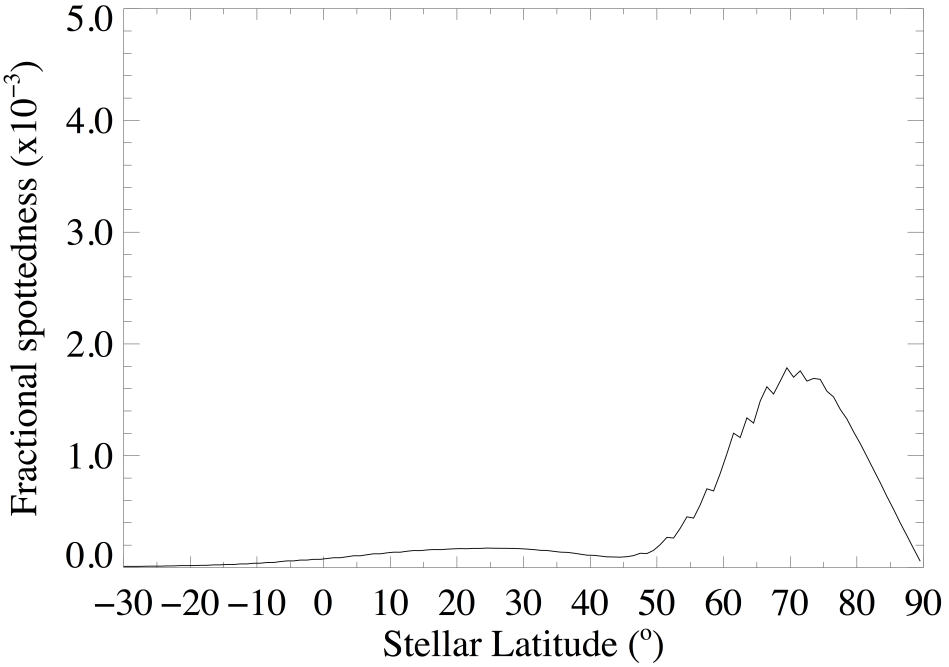

Figure 5.6: Plot of surface spot occupancy as a function of latitude of HIP43720 - AAT

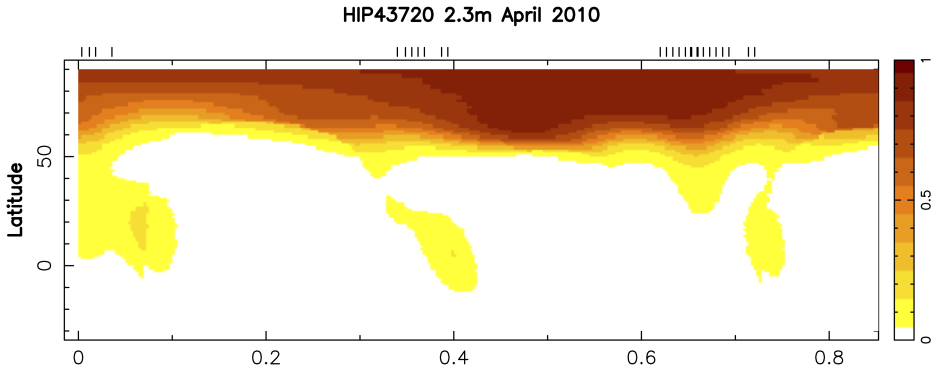

Figure 5.7: Rectangular 2.3-m Doppler Imaging Spot Occupancy Map of HIP43720 data.

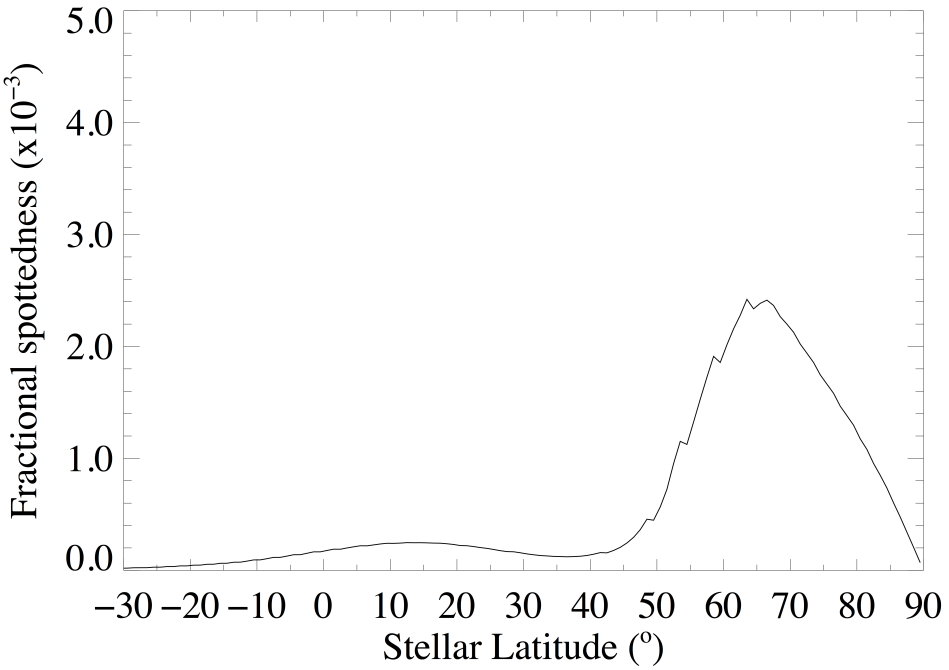

Figure 5.8: Plot of surface spot occupancy (fractional spottedness) as a function of latitude of HIP43720 - 2.3-m

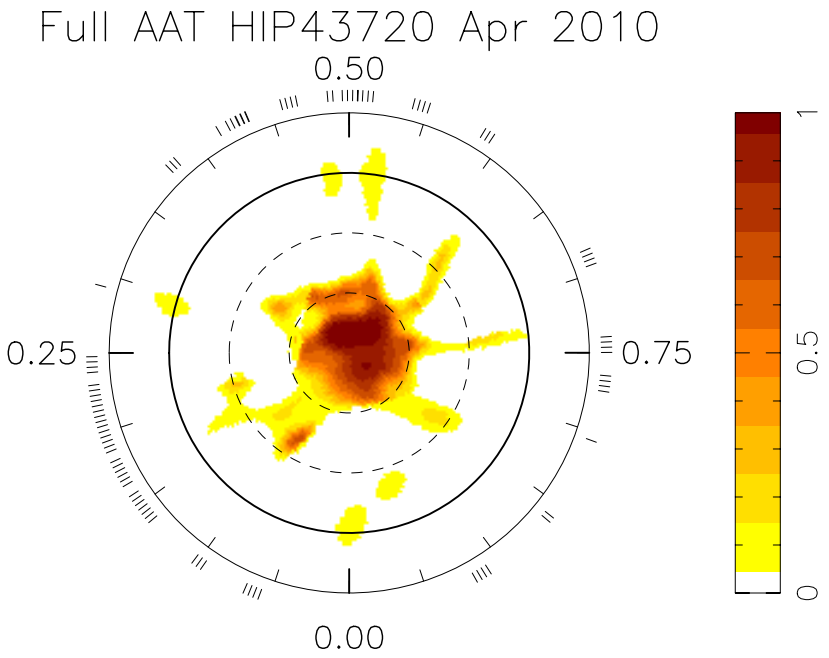

Figure 5.9: Maximum entropy brightness image for HIP43720 using all profiles from AAT March 25 to April 5 2010

As previously mentioned the full AAT April observing run went from March 25 to April 5, 2010 the map at Figure 5.9 shows the flattened polar projection. In this map, which has a far greater phase coverage, there is more detail in the polar spot and areas of light spot activity towards the equatorial regions.

The last Maximum entropy brightness images for HIP43720 Figures 5.10 and 5.11 were created from the 2.3-m data using parameters were calculated using the χ^2-minimisation technique in Chapter 4.5 . The map is slightly different to the AAT and 2.3-m maps produced earlier in this section which were done using the same parameters for the purpose of comparison. The parameters found using the 2.3-m data compared to those found from the AAT are given in Table 5.4.

The main difference was the $v\sin i$ measurement which is at 39.8 km s^{-1} for the 2.3-m data and at 39.5 km s^{-1} for the AAT and previously presented 2.3-m map (Figure 5.3 and 5.2). These measurements are, however, still within the error bars. Figures 5.12, 5.13 and 5.14 show the plots for the results of the

Table 5.4: Comparison of Stellar Parameters for HIP43720: 2.3-m as found using χ^2-minimisation technique and those from Waite *et al.* (2011) for the AAT data.

Parameter	AAT (Waite *et al.* (2011))	2.3-m from χ^2-minimisation technique
Equatorial Period	3.14±0.1 days	—
Inclination Angle (i)	55±5°	58°
Projected ($v\sin i$) Rotational Velocity	39.5±0.5 km s^{-1}	39.8 km s^{-1}
Photospheric Temperature (T_{phot})	6000±30 K	-
Spot Temperature, (T_{spot})	4100±30 K	-
Radial Velocity, v_{rad}	2.4±0.1 km s^{-1}	2.4 km s^{-1}
Stellar radius	3.0R$\odot$	

χ^2-minimisation technique to the refine the data for radial velocity, $v\sin i$ and stellar inclination angle (i).

It is believed that this star has a small faint companion but it has not yet been found. This has been put forward to explain the radial velocity changes that this star seems to experience. In 2010 it was 2.2 km s^{-1} and in 2011 it is 2.4 km s^{-1}. (Waite *et al.*, 2012)

5.7.1 Summary of Stellar Parameters

It can be seen from Figures 5.12, 5.13 and 5.14 that the χ^2 values are reasonably parabolic. The plots show a minimum, which is the most suitable value for the derived parameter to produce the best modelled fit to the observed data.

The final values for the stellar parameters using the χ^2-minimisation technique are: Radial velocity: 30.9 km s^{-1}
$v\sin i$: 89.5 km s^{-1} and
Stellar Inclination Angle (i) : 55°.

5.8 Summary and Conclusions

In this chapter observations of HIP43720 with both the AAT and 2.3-m telescope have been presented, reduced, and analysed using the technique of Doppler Imaging. Known fundamental parameters of the star were listed and

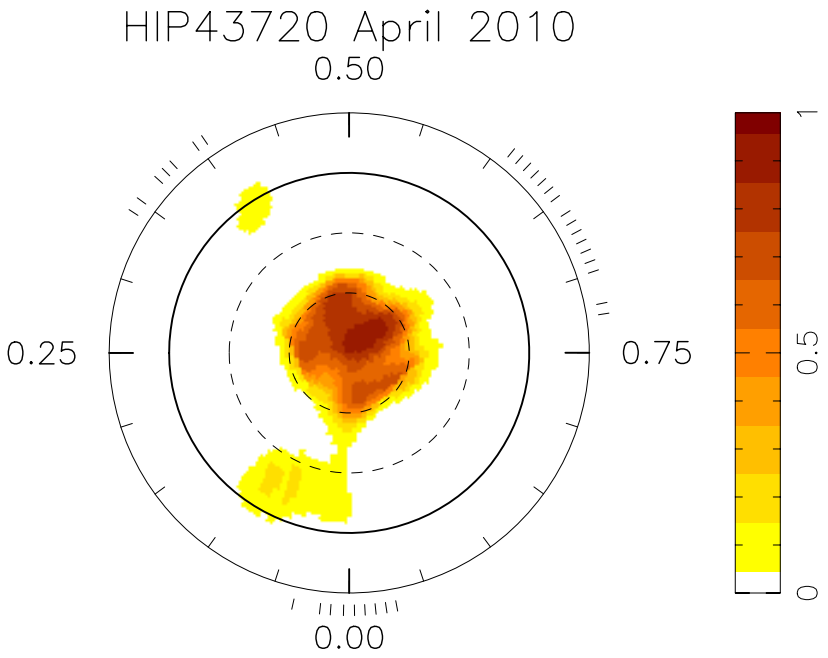

Figure 5.10: Maximum Entropy Brightness Image for HIP43720 using χ^2-minimisation on the 2.3-m data.The image is a flattened polar projection. The radial ticks outside the plot give the phases of observation. The dotted circles from the centre are latitudes of +60° and +30°, the complete circle is the equator and the outside circle extends to -30°. The coloured bar indicates a gradation of spottedness with 0 (absent) to 1 (most intense)

then examined independently through the maximum entropy code to find that most values were within the error bars. The maps produced from both the AAT and 2.3-m telescope have been compared and variations noted. The AAT because of its larger mirror and higher resolution spectrograph is capable of resolving more surface detail. The results show, that the ANU 2.3-metre telescope and its echelle spectrograph can obtain adequate maps even with this fainter, slower rotating object than AB Dor and that it is possible to do scientifically useful observations for DI with this telescope.

Spectral resolution and signal-to-noise ratio, which are equipment limitations, affect the resolvability of the surface features in a spot occupancy map particularly for faint targets. The limitation of signal-to-noise ratio can be counteracted by the use of LSD which is used to produce high signal-to-noise ratio profiles. The recoverable spot coverage is heavily reliant on the spatial

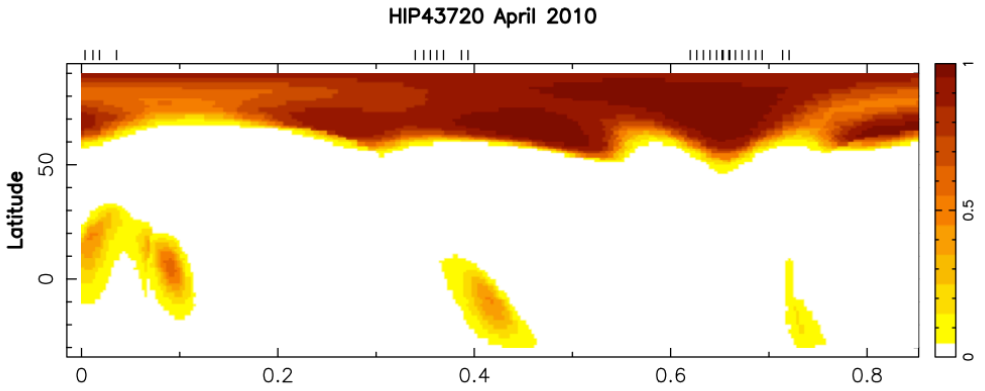

Figure 5.11: Rectangular 2.3-m Doppler Imaging Spot Occupancy Map of HIP43720 using fχ^2-minimisation on the 2.3-m data.

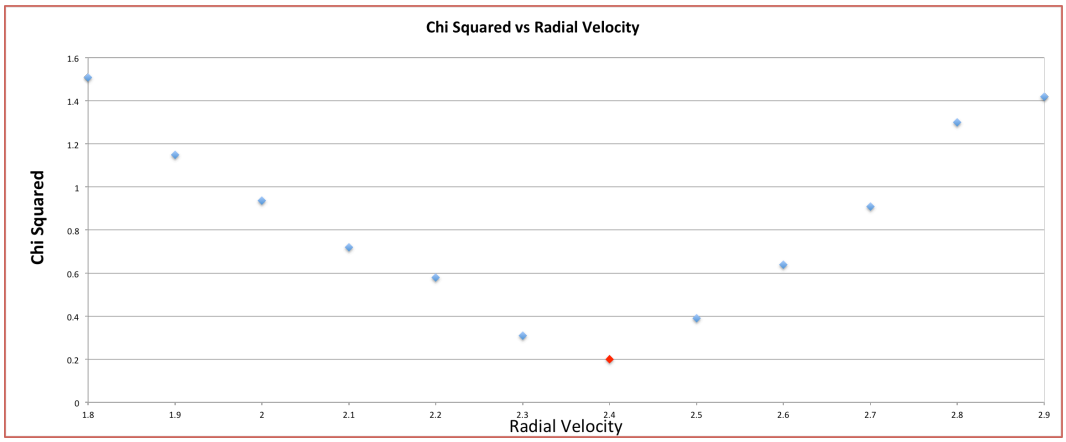

Figure 5.12: Graph of χ^2 versus Radial Velocity

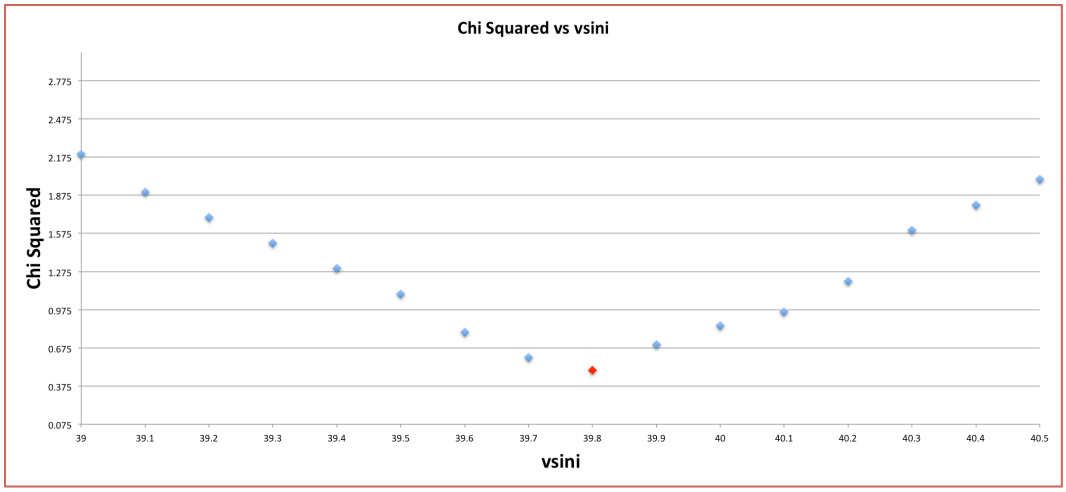

Figure 5.13: Graph of χ^2 versus $v$sini

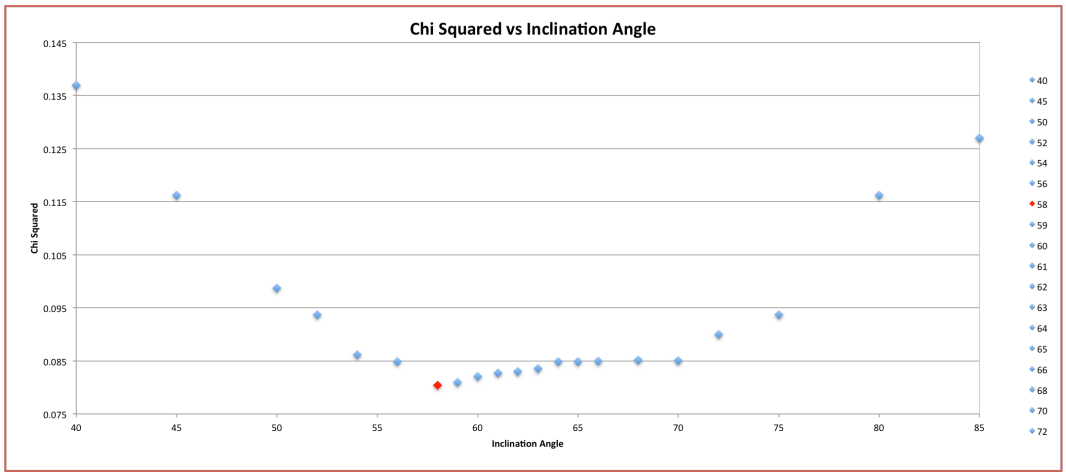

Figure 5.14: Graph of χ^2 versus Stellar Inclination Angle (i)

resolution, especially for targets with low values of $v\sin i$ (Piskunov *et al.*, 1990). This must be taken into account when comparing spot coverage percentages of targets with different $v\sin i$ values. Even with the advances in astronomical equipment that has occurred over the last 20 years, the issue of low resolution combined with low $v\sin i$ values must be taken into account, especially when choosing targets for observation.

At 39 km s^{-1} as a projected rotational velocity, HIP43720 was at the lower end of what had been believed could be imaged with the 2.3-m telescope and the echelle spectrograph. It is also a faint star requiring the 1800 sec exposures, which are the maximum time for an exposure due to the problem of cosmic rays. In the LSD profiles you can see the slight line deformation due to the presence of spots. However, we were able to get a reasonable signal-to-noise on average around 875 for each exposure. The ability to map this star further confirmed the capability of the telescope and instrument but also that it could observe stars at the lower end of the projected rotational velocity scale.

The observations and creation of DI maps for AB Dor and HIP43720 that have been compared with maps made from data collected at the AAT has shown it is possible. This makes the 2.3-m with the echelle spectrograph an ideal instrument to increase the sample size of southern targets being analysed using DI. This can be achieved by extending the current target list as well as obtaining more long term observations of the current targets, building up a representative sample of the activity of young solar-type stars. Other areas where DI would be of value is in considering the properties, including size, distribution and longevity of active regions on stars across the H-R diagram.

Through the production of comparison maps for AB Dor and the slower HIP43720 this work has clearly demonstrated that it is possible to map young suns with the ANU 2.3-metre telescope. In doing so it has laid the groundwork for a larger long-term survey of the powerful activity and dynamo of stellar proxies of early solar evolution. Such a program will enable the study the long-term evolution of spot coverage, spot distribution, prominence expulsion, and differential rotation and the emergence of the magnetic cycle, which is a key aspect of the solar dynamo today. Such observations are important ingredients in understanding early stellar evolution and how intense solar activity has influenced the early development of the solar system and the habitability of the Earth itself.

Chapter 6

Conclusions and Future Directions

6.1 Introduction

Given that young solar-type stars are characterised by rapid rotation and strong spot activity Collier-Cameron (2000), DI offers an effective way to probe their dynamos. In particular DI of starspots can be used to assess the spot latitude distribution and differential rotation of young solar analogues, thereby providing empirical data to compare with the predictions of interface-layer and distributed dynamo models.

Even solar-type dynamo models cannot be adequately tested using solar observations alone, as it is not possible to vary any of the parameters of the Sun. As the number of stars upon which long-term studies can be undertaken is increased, so is the potential to measure directly the systematic variations with stellar properties and long-term changes to better constrain the theoretical models. Spot evolution, solar-like cycles and changes in differential rotation will place important constraints on theoretical models using active regions and their evolution on various timescales.

There are currently a number of stars identified as suitable or potentially suitable for cool star DI studies in the Southern hemisphere. These include those from the survey of Waite *et al.* (2011); those potential candidates from the survey mentioned earlier in this thesis and others previously known, including AB Dor, HD106506, R58 and HIP43720. The majority of these stars are brighter than magnitude 10 and have a $v\sin i$ greater than 40 km s^{-1} and so would be suitable for observing with the 2.3-m telescope. The ongoing systematic observations of these targets can allow the study the evolution of spot features, prominence activity and identification of activity cycles on young

solar type stars.

6.2 Doppler Imaging into the Future - Long-term Monitoring for Solar-like Cycles

The sample size of solar-type stars studied using DI, ZDI and differential rotation analysis remains small in a statistical sense. An improved understanding of dynamo processes requires an increase in this sample size across spectral types, rotation rates and activity indices. This work, however, requires long-term access to telescope time, at regular intervals to monitor any cyclic activity and changes in spot distribution and differential rotation.

Järvinen *et al.* (2005) reported evidence for a possible activity cycle for AB Doradus of $\sim$ 20 years and the possible presence of a flip-flop cycle of $\sim$5.5 years. Innie teal (2008) repeated the study with new data and also determined a cycle period supporting the $\sim$20 year period suggested by Järvinen *et al.* (2005) while Lalitha and Schmitt (2013) presents evidence of a 17 year photometric cycle. Long-term on going observations of stars like AB Dor enable detailed study of activity cycles that may occur on young solar-type stars.

This project has laid the groundwork for follow-up studies of the nature of the activity and dynamo of stars representing early solar history. Time on large telescopes, (such as the AAT), can be particularly competitive and hard to obtain, and so the suitability of the 2.3-m for Doppler Imaging now offers a useful alternative for DI studies.

6.3 Issues and Challenges

Doppler Imaging studies using the 2.3-m telescope currently face some limitations and challenges. While some of these are common to all DI studies, some are unique to this specific telescope setup. The constraints include the magnitude of the target stars and their rotational velocity and rotational period.

For the 2.3-m, the target star needs to have a visual magnitude preferably brighter than 10 while the AAT and UCLES can observe stars up to magnitude 12. This is most critical if the star is an ultra-rapid rotator, as phase smearing becomes an issue when exposures greater than 1-2% of the phase period are required. These constraints can be overcome with long period observations

with regular long observing runs covering multiple rotation periods of the various target stars.

Another issue has been with the data reduction software ESpRIT.

ESpRIT software is a custom-written package written expressly for reduction of data collected on the AAT with UCLES when configured for ZDI observing.

Due to the peculiarities of the instrumental setup used for ZDI, Donati and Brown (1997) developed a dedicated package for image extraction (Mengel, 2005). Each order produced by UCLES include two spectra; one for each polarization state and the setup uses the Bowen-Walraven image slicer to produce a complicated order section profile, which results in distortion in the slit shape. Donati and Brown (1997) discusses how these peculiarities present difficulties for more conventional data reduction routines. UCLES is in a far more stable environment where few, if any, changes occur between runs, whereas the echelle instrument is one of two instruments on the Nasmyth B focus of the 2.3-m telescope and is often removed between runs. Each new observing run requires a manual setup, and it is not always possible to get exactly the same setup as for previous runs.

Many parameters are hard coded into ESpRIT, and this requires code modification and recompiling when analysing new target stars. In addition, the FITS file headers differ between both telescopes and it was necessary to write scripts to amend the headers. The 2.3-m headers do not record HJD and so the IRAF *setjd* task needs to be run on each nights data to set the Julian date so that phase information to be calculated, and accurate DI maps to be produced. The process of reducing the data from raw fits to final Doppler Image map also requires many steps and manual inputs. The software was written to work with fibres, not the long slit of the 2.3-m echelle so moving forward one future task would be to incorporate some software work-arounds into more permanent code changes and develop as automated a data reduction pipeline process as possible.

Creating robust and semi-automatic data reduction pipeline software that would work with minimal tweaks and make the necessary adjustments in software that it is so difficult to achieve in hardware would be a worthwhile project.

The 2.3-m echelle is a long slit spectrograph with less resolution, less orders and different chip geometry so the routines for *geometry*, *wcal* and *extract*, as described in Chapter 3, all required to be modified to work with 2.3-m data.

Using a target which is well known as far as stellar parameters and general surface features are concerned, (such as AB Dor), was a useful confirmation of the results.

Another issue is that the echelle on the 2.3-m has to be physically adjusted and setup for each run. This is a particularly manual process involving the adjusting of a vernier to the required setting, taking an arc frame to check the location of the chosen calibration pixels and repeating the process until the resulting setup is as close as can be achieved. It is thus almost impossible to get precisely the same set up the same for two runs. In contrast, on the AAT the amount of tweaking between runs is minimal; even when those runs are separated by periods of up to six months.

A major challenge is that the 2.3-m echelle spectrograph and its detector are old, inefficient and have ongoing problems including the number of occasions where more than 60% of the biases, flats or arcs taken on a night are not usable. A new instrument, which could operate from Cassegrain focus and have the spectrograph or spectropolarimeter instrument located in a stable clean room, would improve the usability of the set up considerably.

Continuous high-resolution spectra from an observing site that operates for many years without significant instrumental modifications could then provide observations, of a consistent quality for comparing Doppler maps across complete activity cycles.

6.4 Concluding Thoughts

This thesis project concentrated on assessing the suitability of the Australian National University's 2.3-m telescope for Doppler Imaging (DI) studies of stellar activity; and the observations and creation of DI maps for AB Dor and HIP43720 that have been compared with maps made from data collected at the AAT suggests this is possible. At 39 km s^{-1} as a projected rotational velocity, HIP43720 was at the lower end of what is normally imaged. It is also a faint star requiring the 1800-second exposures, the maximum time for an exposure due to the problem of cosmic rays. In the LSD profiles, slight line deformation due to the presence of spots can be seen and an acceptable signal to noise on average around 875 for each exposure was able to be obtained.

In overall terms, the 2.3-m with the echelle spectrograph, then offers a way to increase the sample size of southern targets being analysed using DI. Such

a survey can be achieved by extending the current target list and long term observations of current and new targets, to build a representative sample of the activity of young solar-type stars. DI would also be of value are in studying more generally the properties (including sizes, distributions and longevity) of active regions on stars across the H-R diagram.

In conclusion, through the production of comparison maps for AB Dor and HIP43720 this work has demonstrated that it is possible to map "young suns" with the ANU 2.3-metre telescope. In doing, so it has laid the groundwork for a larger long-term survey of the powerful activity and dynamo of stellar proxies for early solar evolution. Such observations are of value in understanding early solar evolution, and how intense solar activity influenced the early development of the solar system and the habitability of the Earth itself.

Works Cited

Amado, P. J., Cutispoto, G., Lanza, A. F., and Rodonò, M. (2001). AB Doradus: Long- and short-term light variations and spot parameters. In J. Garcìa López, R. Rebolo, and M. R. Zapatero Osorio, editors, *Proc. of the Eleventh Cambridge Workshop on Cool Stars, Stellar Systems, and the Sun*, pages 895–900, Cambridge. ASP Conference Series.

Babcock, H. W. (1961). The topology of the Sun's magnetic field and the 22–year Cycle. *The Astrophysical Journal*, **13**(2), 572–587.

Baliunas, S. L. and Vaughan, A. H. (1985). Stellar Activity Cycles. *Annual Review of Astronomy and Astrophysics*, **23**, 379–412.

Barnes, J. R., Collier-Cameron, A., James, D. J., and Donati, J.-F. (2000). Doppler images from dual-site observations of southern rapidly rotating stars – I. Differential rotation on PZ Tel. *Monthly Notices of the Royal Astronomical Society*, **314**(1), 162–174.

Barnes, J. R., Collier-Cameron, A., James, D. J., and Donati, J.-F. (2001). Doppler images from dual-site observations of southern rapidly rotating stars – II. Starspot patterns and differential rotation on Speedy Mic. *Monthly Notices of the Royal Astronomical Society*, **324**(1), 231–242.

Barnes, J. R., James, D. J., and Collier-Cameron, A. (2002). The boundaries of doppler imaging: Starspot patterns on M dwarfs. *Astronomische Nachrichten*, **323**(3-4), 333–335.

Barnes, J. R., Collier-Cameron, A., Donati, J.-F., James, D. J., Marsden, S. C., and Petit, P. (2005). The dependence of differential rotation on temperature and rotation. *Monthly Notices of the Royal Astronomical Society: Letters*, **357**(1), L1–L5.

Berdyugina, S. V. (2002). Sunspot and starspot interiors as seen from molecular lines. *Astronomische Nachrichten*, **323**(3/4), 192–195.

Berdyugina, S. V. (2005). Starspots: A key to the stellar dynamo. *Living Reviews in Solar Physics*, pages 1–62.

Berdyugina, S. V. and Tuominen, I. (1998). Permanent active longitudes and activity cycles on RS CVn stars. *Astronomy & Astrophysics*, **336**, L25.

Berdyugina, S. V. and Usoskin, I. G. (2003). Active longitudes in sunspot activity : Century scale persistence. *Astronomy & Astrophysics*, **405**, 1121–1128.

Bessell, M. (2011). 2.3 metre echelle.

Biermann, L. (1938). Konvektion im inneren der sterne II. *Astronomische Nachrichten*, **264**(22–24), 361–396.

Biermann, L. (1948). Konvektion in rotierenden sternen. *Astronomische Nachrichten*, **25**, 135.

Brown, S. F., J-F, D., Rees, D. E., and M, S. (1991). Zeeman–doppler imaging of solar–type and ap stars. iv. maximum entropy reconstruction of 2d magnetic topologies. *Astronomy & Astrophysics*, **250**, 463.

Chaisson, E. and McMillan, S. (2010). *Astronomy Today*. Pearson Education, Upper Saddle River, New Jersey, USA, seventh edition.

Chauvin, G., Thomson, M., Dumas, C., Beuzit, J.-L., Lowrance, P., Fusco, T., Lagrange, A.-M., Zuckerman, B., and Mouillet, D. (2003). Adaptive optics imaging survey of the tucana-horologium association. *Astronomy & Astrophysics*, pages 1–7.

Close, L. M., Lenzen, R., Guirado, J. C., Nielsen, E. L., Mamajek, E. E., Brandner, W., Hartung, M., Lidman, C., and Biller, B. (2005). A dynamical calibration of the mass–luminosity relation at very low stellar masses and young ages. *Nature*, **433**(7023), 286–9.

Collier-Cameron, A. (1992). Modelling stellar photospheric spots using spectroscopy. In P. B. Byrne and M. D, editors, *Surface Inhomogeneities on Late–Type Stars*, volume 397, pages 33–45. Springer–Verlag, Heidelberg.

Collier-Cameron, A. (2000). Mapping starspots and magnetic fields on cool stars. In *IAU Symposium 2003*, Manchester UK.

Collier-Cameron, A. and Donati, J.-F. (2002). Doin' the twist: secular changes in the surface differential rotation on ab doradus. *Monthly Notices of the Royal Astronomical Society*, **329**(1), L23–L27.

Collier-Cameron, A. A., Donati, J.-F., and Semel, M. (2002). Stellar differential rotation from direct starspot tracking. *Monthly Notices of the Royal Astronomical Society*, **330**, 699–705.

Deutsch, A. J. (1958). Harmonic analysis of the periodic spectrum variables. In B. Lehnert, editor, *Electromagnetic Phenomena in Cosmical Physics in IAU Symposium*, volume 6, pages 209–221, Cambridge, UK. Cambridge University Press.

Donahue, R. A., Baliunas, S., Soon, W., Horne, J., Frazer, J., Woodard-Eklund, L., Bradford, M., Rao, L., Wilson, O., and Zhang, Q. (1995). Chromospheric variations in Main-sequence stars II. *The Astrophysical Journal*, **438**, 269.

Donati, J.-F. and Brown, S. F. (1997). Zeeman-Doppler Iimaging of active stars. V. sensitivity of maximum entropy magnetic maps to field orientation. *Astronomy & Astrophysics*, **326**, 1135–1142.

Donati, J.-F. and Collier-Cameron, A. (1997). Differential rotation and magnetic polarity patterns on AB Doradus. *Monthly Notices of the Royal Astronomical Society*, **291**.

Donati, J.-F. and Landstreet, J. D. (2009). Magnetic fields of non–degenerate stars. *ArXiv Eprints*, pages 1–41.

Donati, J.-F. and Semel, M. (1990). Zeeman-doppler imaging - a new option for magnetic field study of AP and solar-type stars. *Solar Physics*, **128**, 227–242.

Donati, J.-F., Collier-Cameron, A., Hussain, G., and Semel, M. (1999). Magnetic topology and prominence patterns on AB Doradus. *Monthly Notices of the Royal Astronomical Society*, **302**, 437–456.

Donati, J.-F., Mengel, M., Carter, B. D., Marsden, S. C., Collier-Cameron, A., and Wichmann, R. (2000). Surface differential rotation and prominences

of the Lupus post T Tauri star RX J1508.6–4423. *Monthly Notices of the Royal Astronomical Society*, **316**, 699–715.

Donati, J.-F., Collier-Cameron, A., Semel, M., Hussain, G., Petit, P., Carter, B. D., Marsden, S. C., Mengel, M., Lopez–Ariste, A., Jeffers, S. V., and Rees, D. E. (2003a). Dynamo processes and activity cycles of the active stars AB Doradus, LQ Hydrae and HR1099. *Monthly Notices of the Royal Astronomical Society*, **345**, 1145–1186.

Donati, J.-F., Collier-Cameron, A., and Petit, P. (2003b). Temporal fluctuations in the differential rotation of cool active stars. *Monthly Notices of the Royal Astronomical Society*, **347**, 1187–1199.

Dorren, J. D. and Guinan, E. F. (1994). HD129333: The Sun in its infancy. *The Astrophysical Journal*, **428**, 805.

Freedman, R. A. and Kaufmann, W. J. (2007). *Universe*. W H Freeman & Co, New York, 8th edition.

García-Alvarez, D., Drake, J. J., Lin, L., Kashyap, V. L., and Ball, B. (2005). The Coronae of AB Doradus and V471 Tauri: Primordial angular momentum versus tidal spin-up. *The Astronomical Journal*, **621**, 1009–1022.

Goncharskii, A. V., Stepanov, V. V., Khokhlova, V. L., and Yagola, A. G. (1977a). Mapping of chemical elements on the surfaces of Ap stars. I. solution of the inverse problem of finding local profiles of spectral lines. *Soviet Astronomy Letters*, **26**, 690—696.

Goncharskii, A. V., Stepanov, V. V., Khokhlova, V. L., and Yagola, A. G. (1977b). Reconstruction of local line profiles from those observed in an Ap spectrum. *Soviet Astronomy Letters*, **3**, 147—149.

Gough, D. O. and McIntyre, M. E. (1998). The inevitability of a magnetic field in the Sun's radiative interior. *Nature*, **394**, 755–757.

Granzer, T. (2002). Relations between star–spot distribution and stellar parameters. *Astronomische Nachrichten*, **323**(3–4), 395–398.

Gray, D. F. (1992). *The Observation and Analysis of Stellar Photospheres*. Cambridge University Press, Cambridge, UK.

Guirado, J. C., Reynolds, J. E., Martí-Vidal, I., Lestrade, J., Preston, R. A., King, E. A., Lovell, J., McCulloch, P. M., and Johnston, K. J. (1997). Astrometric detection of a low-mass companion orbiting the star AB Doradus. *The Astrophysical Journal*, **490**, 835.

Hall, D. S. and Henry, G. W. (1994). The law of starspot lifetimes. *International Amateur–Professional Photoelectric Photometry Communication*, **55**, 51–57.

Hathaway, D. H. (2012). The solar dynamo.

Hatzes, A. P. (1995). Doppler imaging of the cool spot distribution on the weak T Tauri Star V410 Tauri. *The Astrophysical Journal*, **451**, 784–794.

Hog, E., Fabicius, C., Makaov, V. V., Uban, S., Corbin, T., Wycoff, G., Bastian, U., Schwekendiek, P., and Wicenec, A. (2000). The Tycho-2 catalogue of the 2.5 million brightest stars. *Astronomy & Astrophysics*, **355**, L27–30.

Horne, K. (1986). An optimal extraction for CCD spectroscopy. *Publications of the Astronomical Society of the Pacific*, **98**, 609–617.

Hussain, G. A. J. (2002). Starspot lifetimes. *Astronomische Nachrichten*, **323**(3–4), 349–356.

Hussain, G. A. J., van Ballegooijen, A. A., Jardine, M., and Collier-Cameron, A. (2001). Modeling the corona of AB Doradus. In *12th Cambridge Workshop on Cool Stars, Stellar Systems and the Sun.*, pages 1–10, Boulder Colorado.

Hussain, G. A. J., Brickhouse, N. S., Dupree, A. K., Jardine, M. M., van Ballegooijen, A. A., Hoogerwerf, R., Collier-Cameron, A., Donati, J.-F., and Favata, F. (2005). Inferring coronal structure from X-Ray light curves and Doppler Shifts: A Chandra study of AB Doradus. *The Astrophysical Journal*, **621**, 999–1008.

Innis, J. L., Thompson, K., and Coates, D. W. (1986). On the evolutionary status of the active chromosphere stars AB Doradus (HD36705) and PZ Telescopium (HD174429). *Monthly Notices of the Royal Astronomical Society*, **223**, 183–188.

Innis, J. L., Thompson, K., Coates, D. W., and Evans, T. L. (1988). Observations of active-chromosphere stars. II - Photometry of AB Dor, 1978-1987.

Monthly Notices of the Royal Astronomical Society, **235**, 1411–1422.

Järvinen, S. P., Berdyugina, S. V., Tuominen, I., Cutispoto, G., and Mengel, M. (2005). Magnetic activity in the young solar analog AB Dor: Active longitudes and cycles from long-term photometry. *Astronomy & Astrophysics*, **432**, 657–664.

Järvinen, S. P., Berdyugina, S. V., Korhonen, H., Ilyin, I., and Tuominen, I. (2007). Magnetic activity in the photosphere and chromosphere. *Astronomy & Astrophysics*, **472**, 887–895.

Jeffers, S. V., Donati, J.-F., and Collier-Cameron, A. (2006). Magnetic activity on AB Doradus: Temporal evolution of starspots and differential rotation from 1988 to 1994. *Monthly Notices of the Royal Astronomical Society*, **583**, 18.

Kochukhov, O., Drake, N. A., Piskunov, N. E., and de la Reza, R. (2004). Multi-element abundance doppler imaging of the rapidly oscillating Ap Star HR 3831. *Astronomy & Astrophysics*, **424**, 935–950.

Koen, C. and Eyer, L. (2002). New periodic variables from the Hipparcos Epoch Photometry. *Monthly Notices of the Royal Astronomical Society*, **331**, 45–59.

Koen, C., Kilkenny, D., van Wyk, F., and Marang, F. (2010). UBV(RI)$_C$ JHK observations of Hipparcos-selected nearby stars. *Monthly Notices of the Royal Astronomical Society*, **403**, 1949–1968.

Kron, G. E. (1947). The probable detection of patches of varying brightness on AR Lacertae B. *Publications of Astronomical Society of the Pacific*, **350**, 261–265.

Kurucz, R. L. (1993). CDROM #13 (ATLAS9 Atmospheric Models) and #18 (ATLAS9 and SYNTHE routines) spectral line databases.

Lalitha, S. and Schmitt, J. (2013). A solar-like magnetic activity cycle on the active ultra-fast rotator AB Dor A? *Astronomy & Astrophysics*.

Larmor, J. (1919). How could a rotating body such as the sun become a magnet? *Reports of the British Association*, **87**, 159–160.

Leighton, R. B. (1964). Transport of magnetic fields on the Sun. *The Astrophysical Journal*, **140**, 1547–1562.

Lim, J., White, S. M., Nelson, G. J., and Benz, A. O. (1994). Directivity of the radio emission from the K1 dwarf star AB Doradus. *The Astrophysical Journal*, **430**, 332.

Lockwood, G. W., Skiff, B. A., Henry, G. W., Henry, S., Radick, R. R., Baliunas, S. L., Donahue, R. A., and Soon, W. (2007). Patterns of photometric and chromospheric variation among sun-like stars: A 20-year perspective. *The Astrophysical journal Supplement*, **171**, 260–303.

Love, J. J. (1999). Reversals and excursions of the Geodynamo. *Astronomy & Geophysics*, **40**(6), 14–19.

Luhman, K. L., Stauffer, J. R., and Mamajek, E. E. (2005). The age of AB Doradus. *The Astrophysical Journal Letters*, **628**, L69–L72.

Maggio, A., Pallavicini, R., Reale, F., and Tagliaferri, G. (2000). Twin X-ray flares and the active corona of AB Dor observed with BeppoSAX. *Astronomy &Astrophysics*, **356**.

Malo, L., R, D., Lafreniere, D., Artigau, E., Gagne, J., Baron, F., and Riedel, A. (2013). Bayesian analysis to identify new star candidates in nearby young stellar kinematic groups. *The Astrophysical Journal*, **762**(2), 88.

Marsden, S. C., Waite, I. A., Carter, B. D., and Donati, J.-F. (2005). Doppler imaging and surface differential rotation of young open cluster stars – I. HD307938 (R58) in IC 2602. *Monthly Notices of the Royal Astronomical Society*, **359**, 711–724.

Marsden, S. C., Jardine, M. M., Velez, J. C., Ramirez, A. E., Brown, C. J., Carter, B. D., Donati, J.-F., Dunstone, N., Hart, R., Semel, M., and Waite, I. A. (2011). Magnetic fields and differential rotation on the pre-main sequence i: The early-g star hd 141943 - brightness and magnetic topologies. *ArXiv Eprints*.

Marsh, T. J. (1989). The extraction of highly distorted spectra. *Publications of the Astronomical Society of the Pacific*, **101**, 1032–1037.

Mathur, S., Salabert, D., Garcia, R. A., Metcalfe, T. S., Regulo, C., and

Ballot, J. (2011). Investigating stellar activity with corot data and complementary ground-based observations. In A. Baglin, M. Deleuil, E. Michel, and C. Moutou, editors, *2nd CoRoT symposium: Transiting planets, vibrating stars their connection*, Marseille.

Mengel, M. M. (2005). *The Active Young Solar-Type Star HR 1817*. Master's thesis, University of Southern Qld, Australia.

Moss, D. and Tuominen, I. (1997). Magnetic field generation in close binary systems. *Astronomy & Astrophysics*, **321**, 151–158.

Mossman, J. E. (1989). A comprehensive search for sunspots without the aid of a telescope, 1981–1982. *Quarterly Journal of the RAS*, **30**, 59–64.

O'Neal, D., Neff, J. E., and Saar, S. H. (1998). Measurements of starspot parameters on active stars using molecular bands in echelle spectra. *The Astrophysical Journal*, **507**, 919–937.

Parker, E. N. (1955). Hydromagnetic dynamo models. *The Astrophysical Journal*, **122**, 293.

Petit, P., Donati, J.-F., and Collier-Cameron, A. (2002). Differential rotation of cool active stars: the case of intermediate rotators. *Monthly Notices of the Royal Astronomical Society*, **334**, 374–382.

Petit, P., Donati, J.-F., and Collier-Cameron, A. (2004). Differential rotation of cool active stars. *Astronomische Nachrichten*, **325**, 221–225.

Phillips, K. J. H. (2006). *Guide to the Sun.* Cambridge University Press, Cambridge UK, digital printing edition edition.

Piskunov, N. E. (2008). Doppler imaging. *Physica Scripta*, **T133**, 014017.

Piskunov, N. E. and Rice, J. B. (1993). Surface imaging of late-type stars. *Publications of the Astronomical Society of the Pacific*, **105**, 1415.

Piskunov, N. E., Tuominen, I., and Vilhu, O. (1990). Surface imaging of late-type stars. *Astronomy & Astrophysics*, **230**, 363–370.

Radick, R. R., Lockwood, G. W., Skiff, B. A., and Baliunas, S. L. (1998). Patterns of variation among sun-like stars. *The Astrophysical journal Supplement*, **118**, 239.

Rice, J. B. (2002). Doppler imaging of stellar surfaces – techniques and issues. *Astronomische Nachrichten*, **323**, 220–235.

Rodonò, M., Lanza, A. F., and Catalano, S. (1995). Starspot evolution, activity cycle and orbital period variation of the prototype active binary rs canum venaticorum. *Astronomy & Astrophysics*, **301**, 75–78.

Saar, S. H. (1990). Magnetic fields on solar–like stars: The first decade. In J. O. Stenflo, editor, *Solar Photosphere: Structure, Convection and Magnetic Fields*, volume 138, pages 427–421, Kluwer, Dordrecht. IAU Symposium.

Scharmer, G. B., Gudiksen, B. V., Kiselman, D., Löfdahl, M. G., and Rouppe van der Voort, L. H. M. (2002). Dark cores in sunspot penumbral filaments. *Nature*, **420**, 151–153.

Scholz, A., Coffey, J., Brandeker, A., and Jayawardhana, R. (2007). Rotation and activity of pre-main sequence stars. *The Astrophysical Journal*, **662**, 1254–1267.

Schrijver, C. J. and Title, A. M. (2001). On the formation of polar spots in sun–like stars. *The Astrophysical Journal*, **551**, 1099–1106.

Schrijver, C. J. and Zwaan, C. (2003). *Solar and Stellar Magnetic Activity*. Number 34 in Cambridge Astrophysics Series. Cambridge University Press, Cambridge UK.

Schüssler, M. and Solanki, S. K. (1992). Why rapid rotators have polar spots? *Astronomy & Astrophysics*, **264**, L13–L16.

Schüssler, M., Holzwarth, V., Solanki, S. K., and Charbonnel, C. (1999). Buried flux tubes in the coronal graveyard. In *Cool Stars, Stellar Systems and the Sun*.

Schwope, A. (2001). Tomography of polars. In H. Boffin, J. Cuypers, and D. Steeghs, editors, *Astrotomography*, volume 573 of *Lecture Notes in Physics*, pages 127–154. Springer Berlin Heidelberg.

Semel, M. (1989). Zeeman–doppler imaging of active stars. *Astronomy & Astrophysics*, **225**, 456–466.

Semel, M., Donati, J.-F., and Rees, D. E. (1993). Zeeman-doppler imaging

of active stars. 3. instrumental and technical considerations. *Astronomy & Astrophysics*, **278**, 231–237.

Skilling, J. and Bryan, R. K. (1984). Maximum entropy image reconstruction: General algorithm. *Monthly Notices of the Royal Astronomical Society*, **211**(1), 111–122.

Strassmeier, K. G. (1999). Doppler imaging of stellar surface structure. XI. the super starspots on the K0 giant HD12545: larger than the entire sun. *Astronomy & Astrophysics*, **347**, 212–224.

Strassmeier, K. G. (2001). Latest results in doppler imaging. *The 11th Cool Stars Stellar Systems and the Sun ASP Conference Series*, **223**, 271–283.

Strassmeier, K. G. (2002). Doppler images of starspots. *Astronomische Nachrichten*, **323**(3-4), 309–316.

Strassmeier, K. G. (2008). Starspots: signatures of stellar magnetic activity. *Proceedings of the International Astronomical Union*, **4**(S259), 363.

Strassmeier, K. G. (2009). Starspots. *Astronomy Astrophysical Review*, **17**, 251–308.

Strassmeier, K. G. and Hall, D. S. (1994). Time–series photometric spot modeling of the RS CVn Binary HR7275. *Publications of the Astronomical Society of the Pacific.*, **64**, 483–485.

Strassmeier, K. G., Lupinik, S., Dempsey, R. C., and Rice, J. B. (1999). Astronomy and doppler imaging of stellar surface structure. the FK Comae–type star HD199178 = V 1794 Cygni. *Astronomy & Astrophysics*, **347**, 225–234.

Thomas, J. H. and Weiss, N. O. (2008). *Sunspots and Starspots*. Cambridge University Press, New York.

Torres, C. A. O., Quast, G. R., da Silva, L., de La Reza, R., F, M. C. H., and Sterzik, M. (2006). Search for associations containing young stars (sacy). i. sample and searching method. *Astronomy & Astrophysics*, **460**, 695–708.

Unruh, Y. C. and Collier-Cameron, A. (1995). The sensitivity of doppler imaging to line profile models. *Monthly Notices of the Royal Astronomical Society*, **273**, 1–16.

van Leeuwen, F. (2007). Validation of the new hipparcos reduction. *Astronomy & Astrophysics*, **474**(2), 653–664.

Vogt, S. S. and Penrod, G. D. (1983). Doppler imaging of spotted stars—application to the RS Canum Venaticorum star HR1099. *Publications Astronomical Society of the Pacific*, **95**, 566–576.

Vogt, S. S., Penrod, G. D., and Hatzes, A. P. (1987). Doppler images of rotating stars using maximum entropy image reconstruction. *The Astrophysical Journal*, **321**, 496–515.

Wade, G. A., Donati, J.-F., Landstreet, J. D., and S, S. S. L. (2000). High precision magnetic field measurements of ap and bp stars. *Monthly Notices of the Royal Astronomical Society*, **313**, 851– 869.

Waite, I. A., Marsden, S. C., Carter, B. D., and Hart, R. (2004). High-resolution spectroscopy of some active southern stars. *Publications of the Astronomy Society of Australia*, **28**(4), 323–337.

Waite, I. A., Carter, B. D., Marsden, S. C., and Mengel, M. W. (2011). High–resolution spectroscopy and spectropolarimetry of some late F–early G–type sun–like stars as targets for zeeman doppler imaging. *Publications of the Astronomy Society of Australia*, **28**(4), 323–337.

Waite, I. A., Marsden, S. C., Carter, B. D., Alecian, E., Donati, J.-F., Semel, M., Burton, D. M., and Hart, R. (2012). Magnetic fields and differential rotation on the G1 star HIP43720. in preparation.

Washuettl, A., Strassmeier, K. G., and Collier-Cameron, A. (2001). Latest doppler images of the RS CVn Binary EI Eridani. In R. J. Garcia Lopez, R. Rebolo, and M. R. Zapaterio Osorio, editors, *11th Cambridge Workshop on Cool Stars, Stellar Systems and the Sun*, volume 223 of *Astronomical Society of the Pacific Conference Series*, page 1308.

Washuettl, A., Strassmeier, K., and Weber, M. (2008). The chromospherically active binary star EI Eridani: II. long-term doppler imaging. *Astronomische Nachrichten*, **330**(4), 366–376.

Wetherill, W. G. (1980). Formation of the terrestrial planets. *Annual Review of Astronomy & Astrophysics*, **18**, 117.

Willson, R. C. and Mordvinov, A. V. (2003). Secular total solar irradiance trend during solar cycles 21–23. *Geophysical Research Letters*, **30**(5).

Zaqarashvili, T. V., Oliver, R., Ballester, J. L., Carbonell, M., Khodachenko, M. L., and Lammer, H. (2011). Rossby waves and polar spots in rapidly rotating stars : implications for stellar wind evolution. *Astronomy & Astrophysics*, **139**, 1–12.

Zeilik, M., Rhodes, M., Budding, E., and De Blasis, C. (1988). A half-century of starspot activity on sv cam. *The Astrophysical Journal*, **332**, 293–298.

Zirin, H. (1988). *The Astrophysics of the Sun.* Cambridge University Press.

Zuckerman, B. and Webb, R. A. (2000). Identification of a nearby stellar association in thehipparcos catalog: Implications for recent, local star formation. *The Astrophysical Journal*, **535**, 959–964.

Zuckerman, B., Song, I., and Bessell, M. S. (2004). The ab doradus moving group f. *The Astrophysical Journal*, **613**, L65–L68.

Zuckerman, B., Rhee, J. H., Song, I., and Bessell, M. S. (2011). The tucana/horologium, columba, ab doradus, and argus associations: New members and dusty debris disks. *The Astrophysical Journal*, page 47.

Appendix A

Spectral Format Table

This table shows the spectral range for each of the orders on the 2.3-metre high resolution echelle spectrograph. It also shows the wavelength in the middle of the order. This table is useful in planning the observation run as well as in setting up the instrument to ensure correct order selection for wavelength coverage. It also shows how from the lower to higher order the coverage is reduced as is the order overlap. This project used orders 34 to 57 to obtain coverage from Li (6707Å) Hα (6562Å)and CaHK (3934Å) (emission) and (3968Å)(absorption).

Table A.1: Spectral Format Tables for 2.3-m Telescope Echelle Spectrograph.

Order	Wavelength Minimum	Wavelength Centre	Wavelength Max	Free Spectral Range
	Å	Å	Å	Å
60	3725.08	3756.38	3787.68	62.61
59	3787.72	3820.09	3852.46	64.75
58	3852.48	3885.98	3919.48	67.00
57	3919.50	3954.18	3988.87	69.37
56	3988.87	4024.81	4060.74	71.87
55	4060.74	4097.99	4135.25	74.51
54	4135.23	4173.88	4212.53	77.29
53	4212.50	4252.62	4292.74	80.24
52	4292.71	4334.39	4376.06	83.35
51	4376.02	4419.35	4462.68	86.65
50	4462.63	4507.71	4552.78	90.15
49	4552.73	4599.66	4646.60	93.87
48	4646.53	4695.44	4744.35	97.82
47	4744.28	4795.29	4846.31	102.03
46	4846.22	4899.48	4952.73	106.51
45	4952.64	5008.29	5063.94	111.30
44	5063.84	5122.04	5180.25	116.41
43	5180.14	5241.08	5302.02	121.89
42	5301.90	5365.78	5429.66	127.76
41	5429.53	5496.56	5563.59	134.06
40	5563.46	5633.88	5704.30	140.85
39	5704.15	5778.23	5852.31	148.16
38	5852.15	5930.18	6008.21	156.06
37	6008.04	6090.34	6172.64	164.60
36	6172.45	6259.39	6346.33	173.87
35	6346.12	6438.10	6530.07	183.95
34	6529.85	6627.31	6724.77	194.92
33	6724.54	6827.99	6931.45	206.91
32	6931.19	7041.21	7151.23	220.04
31	7150.95	7268.18	7385.41	234.46
30	7385.11	7510.28	7635.45	250.34
29	7635.12	7769.06	7903.01	267.90
28	7902.65	8046.33	8190.01	287.37
27	8189.60	8344.13	8498.65	309.04
26	8498.19	8664.82	8831.45	333.26
25	8830.93	9011.16	9191.38	360.45
24	9190.79	9386.34	9581.89	391.10
23	9581.21	9794.13	10007.04	425.83
22	10006.26	10238.97	10471.67	465.41
21	10470.75	10726.14	10981.52	510.77
20	10980.44	11261.99	11543.53	563.10

Appendix B

Preliminary Survey for Southern Doppler Imaging(DI) Candidates

Table B.1: Echelle Exposure Times for Bright Magnitudes(Bessell, 2011).

Magnitude	Exposure Time (secs)	Magnitude (secs)	Exposure Time
3.5	30	8	240
4	60	8.5	340
4.5	45	9	450
5	60	9.5	650
5.5	60	10	900
6	80	10.5	1200
6.5	100	11	1800
7	120	11.5	1800
7.5	180	12	1800

B.1 Introduction

Over 200 young F, G and K spectral type HIPPARCOS unresolved variable stars were observed with the object of identifying suitable candidates for Doppler Imaging studies.

To determine their multiplicity, targets which appeared to have a rotational velocity greater than 20 km s^{-1} were observed at least twice, several hours or a day apart. The initial survey runs were on August 12-17, 2008; December 31, 2008 - January 4, 2009, and further survey work was undertaken on those nights when weather prevented DI observations. These included: June 11, 2009, February 26/27, July 18, July 22, August 28/29, September 16/17, 2010 and June 25/26, 2011 and April 5, 2012.

Exposure times for the survey stars ranged from 60 to 1,200 seconds and were calculated based on Table B.1. The stellar magnitudes ranged from 1.87 to 10.15 with the majority of targets being between 6 and 9 magnitude.

The target list was chosen using the original list from Koen and Eyer (2002). Late F to early K spectral type unresolved variable stars were selected using the following criteria: young stars, brighter than tenth magnitude and variability between 0.04 and 0.1 magnitude. Variability less than 0.04 magnitudes would mean that any spot activity would not be detectable via the deformation of the line profiles and variability greater than of 0.1 magnitudes the star would most likely be an eclipsing binary (Marsden *et al.*, 2005; Waite *et al.*, 2011).

Surveyed stars considered to be good candidates for DI follow up needed to be single or a wide binary, rapid or ultra rapid rotating stars showing evident line deformation and a $v\sin i$ of at least 40 km s^{-1}. Close binaries can be studied with DI but tidal interactions between the stars can, for example, reduce differential rotation on the surfaces of the involved stars(Moss and Tuominen, 1997). The spectral lines of both components may be visible in the spectrum in the case of close spectroscopic binaries. Radial velocities of both components need to be measured to obtain an accurate value of the orbital and rotational period as well as refining other stellar parameters.

The $v\sin i$ constraint is based on spectral resolution as discussed in 2.4.2 as well as on the $v\sin i$ of the target star. Although it is possible to use the DI technique on slower targets - stars with low rotational velocities give a degraded spatial resolution as the number of surface elements on the star that are resolvable is based both on the resolution of the instrument and the $v\sin i$. Spectral resolution and throughput are both instrument limitations, which affect the resolvability of the surface features in a spot occupancy map. The resolution of the 2.3-m echelle is at best 27,000 but averages about ∼24,000 and the throughput is considered to be low.

The resolution of DI is determined by the projected stellar rotation velocity $v\sin i$, as well as by the spectral resolution and noise of the observed spectra. The issue of minimal spectral resolution or minimum for useful DI was discussed in Piskunov *et al.* (1990). They considered resolutions ranging from 20,000 to 50,000 and considered $v\sin i$ values between 15 km s^{-1} and 30 km s^{-1}. At the lowest spectral resolution and with $v\sin i$ of 30 km^{-1} they could still accomplish reasonable recovery for the coarse features and similarly for the highest resolution and a $v\sin i$ of 15 km s^{-1}.

The LSD profile of the observed star provided the first indication of the $v\sin i$, multiplicity and line deformation which may indicate the presence of starspot activity as can be seen in Figure B.1. From the survey, a number of targets have been identified as suitable for follow up DI and spot mapping as they have a large $v\sin i$. Two of these are covered in more detail later in Appendix D.

It is obvious that from one spectrum or LSD profile of a star with potential spot activity it is possible to find the information about the longitude of the cool feature on the stellar surface. In order to reconstruct the latitude position a series of spectral line profiles are necessary taken at as many different

rotational phases of the star as possible.

In the profiles in Figure B.1 the arrows mark the location of possible spots. As the star rotate then the spot can be observed from different angles and perspectives. The bump or deformation will then appear at different parts of the line profile. To identify whether there is a polar or whether the spots are nearer to the equator requires analysis of as many spectra as possible. If the spot is close to the pole then the deformation will stay close to the central or lower part of the profile. A large polar spot will be evidenced by a characteristic flattening at the bottom of the profile. These spots tend also to move more slowly through the spectral line. Spots at lower latitudes can travel across the whole profile at a much higher speed than polar spots and can be seen to cause deformation even up near the wings of the profile.

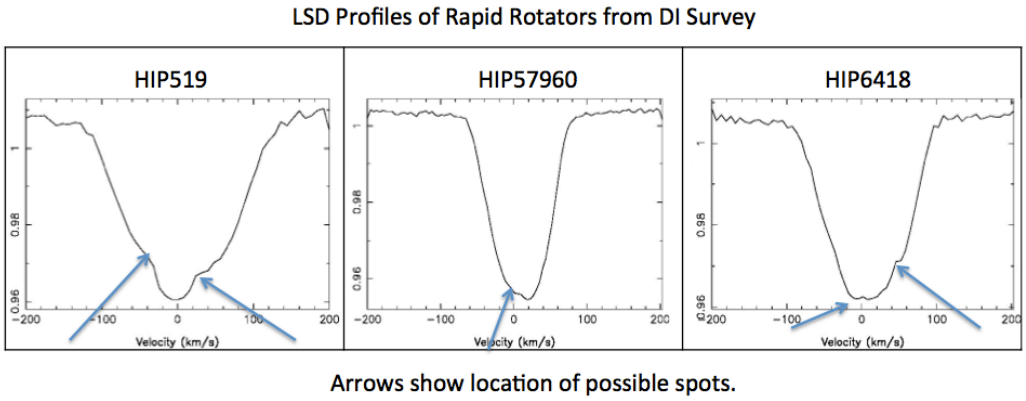

Figure B.1: LSD Profiles of Rapid Rotators from August 2008 observing run showing line deformation which could be evidence of the presence of starspots.

Twenty-one rapid or ultra-rapid rotating stars were identified that also showed evidence of starspot activity via deformation of their line profiles. Two of these new ultra-rapid rotators and are discussed in Appendix D.

Waite *et al.* (2011) defined a terminology to classify solar-type stars on the basis of their projected rotational velocities.

The classifications are:

- Slow Rotators (SR) with $v\sin i < 5$ km s^{-1};
- Moderate Rotators (MR) with $v\sin i$ 5 $\leq <$ 20 km s^{-1};

- Rapid Rotators (RR) with $v\sin i$ between 20 and 100 km s^{-1};
- Ultra-Rapid Rotator (URR) with 100 $\leq v\sin i <$200 km s^{-1}; and
- Hyper-Rapid Rotators (HRR) whose $v\sin i$ are $\geq$ 200 km s^{-1}.

Eighteen possible spectroscopic binaries were also identified via their LSD profiles. Examples are given in Figure B.2 of how the binary system may be easily detected using the LSD profile. These three stars are not listed as binaries on Simbad or in the literature.

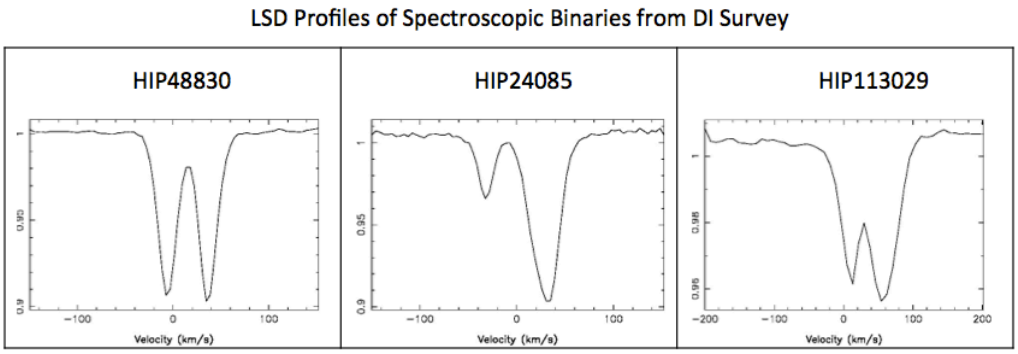

Figure B.2: LSD Profiles of 3 Spectroscopic Binary Stars Identified during the DI Survey

B.2 List of Survey Stars Observed as Part of the Southern DI Candidate Survey

The stars below have been observed as noted and initial work has been done on identifying their rotational velocities and suitability for Doppler Imaging surveys

Table B.2: List of Variable Stars Observed as part of the Search for Southern Sky DI Targets

Target	RA	DEC	Mag	Spectral Type	Exp Time	Notes	Total Obs	Total Nights
HIP355	00 04 30.1	-10 30 34	4.99	K3IBVAR	240		1	1
HIP458	00 05 28.2	-07 39 56	6.97	K5	240		1	1
HIP519	00 06 16.9	-64 14 26	7.92	F3IV	900	Partial	11	7
HIP605	00 07 22.1	-56 50 13	7.48	K5III	180		3	3
HIP999	00 12 30.3	+14 33 49	8.44	K0	340		3	3
HIP1655	00 20 44.5	-25 28 00	8.38	G5III	340		3	3
HIP1792	00 22 46.3	-09 13 51	7.94	G5	240		3	3
HIP2283	00 29 10.4	-11 35 53	7.35	K5III	180		1	1
HIP2340	00 29 54.2	+08 48 22	7.93	K2	300		2	2
HIP2607	00 33 07.3	-39 45 35	7.64	K5III	300		1	1
HIP2729	00 34 51.2	-61 54 58	9.56	K5V	900	possible target	6	6
HIP3146	00 40 00.1	-07 52 19	8.4	K5	340		1	1
HIP3419	00 43 35.4	-17 59 12	2.04	K0III	120		1	1
HIP4945	01 03 26.0	+03 15 20	7.96	K2	340		2	2
HIP4979	01 03 49.0	+01 22 01	6.06	FIV	300	possible target	4	3

Continued on next page

Table B.2 – *Continued from previous page*

Target	RA	DEC	Mag	Spectral Type	Exp Time	Notes	Total Obs	Total Nights
HIP5173	01 06 09.6	-38 13 59	8.21	K5III	300		2	2
HIP5268	01 07 18.7	-61 46 31	5.36	G5III	240		2	2
HIP6418	01 22 24.3	-43 36 09	7.03	F0IV	var		7	6
HIP6454	01 22 56.8	+07 25 09	7.3	G5	300		1	1
HIP6485	01 23 21.30	-57 28 51	8.53	G6V	600		1	1
HIP6565	01 24 20.7	-02 28 19	8.1	K5	300		1	1
HIP7015	01 30 19.4	-52 29 37	7.02	K5III	300		1	1
HIP8281	01 46 41.6	-24 00 50	8.1	K0IV	400		1	1
HIP8681	01 51 41.9	-36 48 18	9.26	K5	900		1	1
HIP9015	01 56 03.0	-37 49 09	8.18	K5/M0III	600		1	1
HIP9655	02 04 12.5	11 51 35	6.43	K4III	300		3	2
HIP9892	02 07 18.1	-53 11 57	8.64	G5V	600		2	2
HIP10188	02 10 58.7	-01 54 53	9.3	F8	900		2	2
HIP10191	02 11 02.2	-35 40 15	10.15	K0	1200		2	2
HIP11121	02 23 06.6	-37 34 34	6.47	K2III	300	multiple star	1	1

Continued on next page

Table B.2 – *Continued from previous page*

Target	RA	DEC	Mag	Spectral Type	Exp Time	Notes	Total Obs	Total Nights
HIP14757	03 10 35.4	-23 44 19	6.37	K0III	300		1	1
HIP15163	03 15 27.9	-34 50 37	7.85	K5III	600		1	1
HIP15291	03 17 17.4	-23 31 13	6.61	K3III	300		1	1
HIP15866	03 24 23.5	-31 07 36	7.35	K1IV/V	500		1	1
HIP17499	03 44 21.6	-21 06 23	8.18	K3III	700		1	1
HIP17759	03 48 06.5	+24 59 18	6.44	K5	300		1	1
HIP17798	03 48 35.7	-20 54 11	5.81	K5III	240		1	1
HIP17861	03 49 21.5	-36 05 33	6.75	K5/M0III	240		1	1
HIP18735	04 00 48.8	+18 11 38	5.89	F4V	300		2	2
HIP19242	04 07 25.2	-42 55 00	6.59	K0III	240		2	2
HIP19260	04 07 41.7	-01 37 18	9.07	K0	900	follow up	3	2
HIP20263	04 20 38.6	06 14 16	6.15	G8IV	240		1	1
HIP21421	04 35 55.2	+16 30 33	0.87	K5III	120		1	1
HIP21495	04 37 00.4	-51 50 27	8.39	G5V	600		2	2
HIP21547	04 37 36.1	-02 28 25	5.22	F0V	240	binary	2	2

Continued on next page

Table B.2 – *Continued from previous page*

Target	RA	DEC	Mag	Spectral Type	Exp Time	Notes	Total Obs	Total Nights
HIP21563	04 37 44.5	-31 24 38	8.13	K0III	600		2	2
HIP21648	04 38 55.7	-13 20 48	8.33	G8/K0	600		1	1
HIP21894	04 42 22.6	-00 55 48	6.73	F0	300		1	1
HIP21959	04 43 10.3	-15 37 15	7.85	K5/M0III	600		2	2
HIP22912	04 55 50.0	-27 42 16	8.46	K2IIpv	600		1	1
HIP23215	04 58 45.3	-18 39 23	8.13	K4III	600		1	1
HIP23231	04 59 45.3	-12 32 15	4.78	F0V	240	multiple star	8	5
HIP23381	05 01 36.2	-44 49 49	7.54	G8/K0III + F	300	binary	1	1
HIP23750	05 06 18.0	+17 48 59	8.82	K0	900		1	1
HIP24085	05 10 26.8	-77 13 02	7.73	K1IIIP	360	binary	1	1
HIP24713	05 18 03.4	-30 00 09	8.41	K5III	680		1	1
HIP25544	05 27 39.4	-60 24 58	6.99	G5V	240	possible target	1	1
HIP25579	05 28 00.4	-44 27 38	8.69	K5/M0III	680		1	1
HIP25737	05 29 44.0	-01 05 32	4.71	K5III	240		1	1
HIP26605	05 39 17.0	-17 49 43	7.77	K5III	300		1	1

Continued on next page

Table B.2 – *Continued from previous page*

Target	RA	DEC	Mag	Spectral Type	Exp Time	Notes	Total Obs	Total Nights
HIP26714	05 40 39.7	-20 17 56	7.44	K0IV	500	binary	1	1
HIP26795	05 41 26.8	+03 46 41	6.82	G5	300		3	2
HIP26953	05 43 09.3	-01 36 48	6.31	K4III	300		1	1
HIP27407	05 48 12.8	-33 13 53	9.11	K5	900		2	1
HIP27473	05 49 05.2	-28 22 47	8.44	K5	600		2	
HIP28780	06 04 36.1	-36 42 34	8.65	K	600		1	1
HIP29071	06 07 56.9	-54 26 21	7.68	G8/K0III + F	600		2	2
HIP29196	06 09 32.4	+22 11 25	5.93	K4III	240		1	1
HIP29592	06 14 11.9	-34 15 18	8.82	K5	700		1	1
HIP29679	06 15 08.4	-20 16 20	5.88	K2III	240		1	1
HIP29913	06 17 51.7	-52 43 59	6.4	K2/K3III	300		2	
HIP29999	06 18 51.4	-73 21 39	7.98	K5III	420		1	1
HIP30271	06 22 03.1	-30 32 01	7.57	K4/K5III	500		1	1
HIP30851	06 28 42.8	-28 14 15	8.69	G8IV	600		1	1
HIP31398	06 35 54.3	-30 05 31	6.94	K5III	360		2	2

Continued on next page

Table B.2 – *Continued from previous page*

Target	RA	DEC	Mag	Spectral Type	Exp Time	Notes	Total Obs	Total Nights
HIP31487	06 35 39.3	-47 26 01	7.41	K0III	360		2	2
HIP32531	06 47 18.7	-55 32 24	5.6	K5III	360		2	2
HIP33003	06 52 36.7	-70 30 37	7.14	K2/K3III	360		2	2
HIP33302	06 55 37.4	-20 008 11	4.66	F2IV/V	240	possible target	5	3
HIP33853	07 01 39.6	-23 30 05	6.73	K5III	360		2	2
HIP34055	07 03 51.6	+12 35 39	6.01	K5	240		1	1
HIP34095	07 04 10.4	+05 12 47	9.08	G5	900		1	1
HIP34177	07 05 16.4	-50 21 36	6.47	K3III	240		2	2
HIP34444	07 08 23.5	-26 23 36	1.83	M	120		2	2
HIP34909	0713 22.3	+16 09 32	5.07	K3V	240		2	2
HIP34939	07 13 48.0	-35 19 09	8.36	K5/M0	600		2	2
HIP35264	07 17 08.6	-37 05 51	2.71	K3Ib	120		2	2
HIP35848	07 23 29.0	-27 50 03	5.37	K4III	300		1	1
HIP35928	07 24 24.5	+18 54 37	8.04	K5	600		2	2
HIP36239	07 27 45.0	-24 46 26	8.38	G8/K0III	600		2	2

Continued on next page

Table B.2 – *Continued from previous page*

Target	RA	DEC	Mag	Spectral Type	Exp Time	Notes	Total Obs	Total Nights
HIP37648	07 43 32.4	-28 24 39	4.63	K5III	240		2	2
HIP37892	07 45 57.2	-18 54 16	7.58	K4III	600		2	2
HIP37985	07 47 07.4	-41 31 03	7.65	K7III	500		2	2
HIP38170	07 49 17.7	-24 51 35	3.34	G6Ia	120		1	1
HIP38516	07 53 16.0	-34 02 20	7.36	K4III	600		1	1
HIP39131	08 00 17.4	-37 50 46	8.68	K5	600		2	2
HIP40005	08 10 12.1	-35 38 48	8.168	K2	900		2	2
HIP40244	08 13 11.7	-23 58 12	8.59	K5/M0III	900		1	1
HIP40526	08 16 30.9	+09 11 08	3.53	K4III	120		2	2
HIP40763	08 19 14.4	-07 33 29	6.91	K5	300		2	2
HIP41670	08 29 44.5	-32 44 59	8.55	K2	600		2	2
HIP41875	08 32 17.3	+29 19 10	7.35	G5	600		2	2
HIP42071	08 34 29.7	-27 05 53	6.4	K3III	300		1	1
HIP42439	08 39 13.2	+07 34 24	7.93	K	600		2	2
HIP42469	08 39 29.8	-21 55 33	8.09	K5III	600		2	2

Continued on next page

Table B.2 – *Continued from previous page*

Target	RA	DEC	Mag	Spectral Type	Exp Time	Notes	Total Obs	Total Nights
HIP43290	08 49 05.7	-39 57 16	7.83	G5V	500		1	1
HIP43380	08 50 10.2	-49 55 29	7.55	F0IV	500		6	3
HIP43404	08 50 28.3	-28 23 24	8.81	K4III	700		1	1
HIP43739	08 54 30.8	+05 27 52	7.23	K5	600		1	1
HIP43798	08 55 12.4	-18 14 28	5.75	K2/K3III	240		4	2
HIP44719	09 06 43.8	-33 34 07	8.42	G8V	700		1	1
HIP44824	09 08 02.9	-25 51 31	4.62	K4/K5III	600		2	2
HIP45264	09 13 31.2	-49 05 40	6.61	K5III	300		2	2
HIP45505	09 16 23.0	-44 15 57	5.12	K3Ib	240		1	1
HIP45706	09 19 04.7	-36 37 57	9.1	K5	900		1	1
HIP46515	09 29 14.7	-35 57 05	4.51	K3III	240		2	2
HIP47959	09 46 23.3	+11 48 36	5.67	K4III	240		1	1
HIP48261	09 50 18.6	+05 13 18	8.47	K2	400		1	1
HIP48374	09 51 40.7	-46 32 51	4.58	G5Ib	240	follow up	2	2
HIP48598	09 54 39.1	-43 19 16	7.18	K2IIIp	240	follow up	2	2

Continued on next page

Table B.2 – *Continued from previous page*

Target	RA	DEC	Mag	Spectral Type	Exp Time	Notes	Total Obs	Total Nights
HIP49300	10 03 46.5	+12 07 20	7.93	K5	600		1	1
HIP49674	10 08 26.6	-11 06 55	8.15	G5	600		1	1
HIP50047	10 13 04.9	-47 55 11	7.21	K3/K4III	600		1	1
HIP50555	10 19 36.8	-55 01 45	4.59	K3III	600		1	1
HIP51140	10 26 48.9	-54 52 38	5.58	K3II/III	240		1	1
HIP51313	10 28 52.6	-64 10 20	5.27	K3Ib	300		1	1
HIP51775	10 34 48.0	+06 57 13	5.07	G8II-III	90		2	2
HIP51924	10 36 24.8	-31 49 59	8.53	K5	600		2	2
HIP52150	10 39 15.9	-74 29 36	6.08	K3II	120		2	2
HIP52564	10 44 47.9	-50 53 06	7.7	G6IV/V	500		1	1
HIP53264	10 53 36.0	-39 07 25	7.51	K2III	500	multiple star	3	3
HIP53325	10 54 26.1	-33 30 09	8.81	K5	900		1	1
HIP55460	11 21 29.3	+03 56 15	8.14	K5	600		1	1
HIP56851	11 39 22.2	-39 23 08	7.87	G8IV	500	binary	1	1
HIP57269	11 44 38.5	-49 25 03	8.91	K0/K1Vp	600		1	1

Continued on next page

Table B.2 – *Continued from previous page*

Target	RA	DEC	Mag	Spectral Type	Exp Time	Notes	Total Obs	Total Nights
HIP57512	11 47 19.1	-57 41 47	5.42	K5III	240		1	1
HIP58359	11 58 01.0	+14 02 17	8.42	G5	600	binary	3	3
HIP58498	11 59 48.9	-62 49 54	7.6	K4/K5Ib	600		1	1
HIP58596	12 00 57.3	-21 15 03	8.18	G6/G8III	600	multiple star	3	3
HIP58905	12 04 46.5	-76 31 09	5.04	K4III	600		1	1
HIP58997	12 05 49.1	-23 46 52	8.89	K5III	600		1	1
HIP59269	12 09 24.6	-38 43 47	8.77	K2III	700		1	1
HIP60918	12 29 05.7	+13 57 01	8.73	K5	600		1	1
HIP63283	12 58 06.3	+17 46 06	7.87	K5	600		2	2
HIP63650	13 02 43.3	-27 00 38	8.81	K0III/IV	600		1	1
HIP64262	13 10 17.0	+09 32 10	9.31	K5	240		1	1
HIP65981	13 31 39.5	-47 50 28	7.89	K5III	300		1	1
HIP67471	13 49 36.8	-09 11 56	8.97	K5	700		1	1
HIP67709	13 52 15.8	-01 30 22	8.97	K5	500		2	
HIP68128	13 56 50.3	-38 23 50	7.68	K5III	240		1	1

Continued on next page

Table B.2 – *Continued from previous page*

Target	RA	DEC	Mag	Spectral Type	Exp Time	Notes	Total Obs	Total Nights
HIP68383	13 59 53.4	-22 20 41	8.71	K1/K2III	500		1	1
HIP68998	14 07 33.5	-54 15 50	8.16	G6III	600	binary	1	1
HIP70919	14 30 10.4	-43 32 49	8.88	G8III	600		1	1
HIP71053	14 31 00.6	-43 50 59	3.57	K3III	120		1	1
HIP72465	14 49 05.9	-05 45 06	8.5	F5	600		1	1
HIP72566	14 50 15.7	-07 51 53	8.71	K5	600		2	
HIP74471	15 13 03.3	+09 34 41	8.32	K0	600		2	2
HIP74598	15 14 31.1	-59 44 07	7.17	K4III	600		2	2
HIP77749	15 52 33.7	-01 54 23	7.85	G5V	500		1	1
HIP77786	15 53 00.8	-57 35 03	8.22	K1III	700		1	1
HIP78377	16 00 02.2	+00 37 25	7.2	K5	600		1	1
HIP78743	16 04 30.6	-28 55 52	7.51	K5III	600		1	1
HIP80598	16 27 21.3	+06 16 15	8.98	K5	900		1	1
HIP81753	16 41 53.5	-63 24 10	8.95	K0III	900		3	3
HIP82544	16 52 19.7	+11 14 31	7.04	K5	600		3	3

Continued on next page

Table B.2 – *Continued from previous page*

Target	RA	DEC	Mag	Spectral Type	Exp Time	Notes	Total Obs	Total Nights
HIP83545	17 04 29.6	-12 40 34	6.91	K0III	600		2	2
HIP84231	17 13 02.9	-58 54 41	8.28	K4III	600		3	3
HIP84586	17 17 25.5	-66 57 04	6.87	K1Vp	200	binary both active	3	3
HIP84708	17 18 52.8	-70 48 47	12.19	Gp	2400	follow up	2	2
HIP86527	17 40 58.5	-32 12 52	6.01	K3III + G	90		2	2
HIP87688	17 55 44.9	+18 30 01	9.22	K5	300		2	2
HIP87880	17 57 07.5	-23 56 21	6.52	K5II	150		1	1
HIP88240	18 01 07.2	+14 07 12	7.77	K5	300		1	1
HIP88743	18 07 00.2	-48 14 50	7.11	G8/K0II/IIIp	220		1	1
HIP90020	18 22 07.0	-46 02 07	8.38	G8III/IV	340		2	2
HIP90100	18 23 14.7	-28 24 44	8.47	K2/3 +M	340		2	2
HIP90420	18 26 57.0	+17 44 02	8.85	K2	450		2	2
HIP90811	18 31 29.0	-21 14 58	8.5	K5/M0III	340		2	2
HIP91847	18 43 31.6	-11 20 13	6.95	K5	160		1	1
HIP92252	18 48 02.5	+10 23 10	8.77	K5	550		2	2

Continued on next page

Table B.2 – *Continued from previous page*

Target	RA	DEC	Mag	Spectral Type	Exp Time	Notes	Total Obs	Total Nights
HIP94450	19 13 21.9	+14 37 05	7.58	K5	300		1	1
HIP94496	19 13 58.6	+00 07 32	7.9	G5	240		2	2
HIP96022	19 31 25.1	-13 58 41	8.71	K2/K3V	550		2	2
HIP98313	19 58 32.5	-03 33 13	6.79	K5	180		2	2
HIP98766	20 03 36.0	-37 31 43	6.85	G8IV	180		2	2
HIP99093	20 07 01.9	+13 19 27	7.14	K5	150		2	2
HIP99553	20 12 12.3	-29 33 11	8.49	K2III	340		2	2
HIP99624	20 13 04.4	-00 19 51	6.47	K5	300		1	1
HIP99881	20 15 53.0	-30 41 15	78.89	K5/M0III	700		1	1
HIP99903	20 16 11.7	-23 30 37	7.83	G5/G6III	240		2	2
HIP101204	20 30 51.4	-00 27 30	9.13	K5	650		2	2
HIP101925	20 39 17.8	-06 11 27	7.47	K5	240		2	2
HIP102355	20 44 21.1	-34 31 08	9.13	K	650		2	2
HIP102803	20 49 37.3	-80 08 01	7.91	K0IIIp	240	follow up	2	2
HIP105224	21 18 52.0	+11 12 12	5.97	K5III	100		2	2

Continued on next page

Table B.2 – *Continued from previous page*

Target	RA	DEC	Mag	Spectral Type	Exp Time	Notes	Total Obs	Total Nights
HIP105389	21 20 50.1	-09 09 06	7.45	K2	180		2	2
HIP106497	21 34 16.6	-13 29 01	7.72	K0IIIp	230		2	2
HIP106993	21 40 08.0	-56 59 23	9.61	K3III	1200		2	2
HIP107523	21 46 35.7	-57 59 48	9.04	K7V	650		2	2
HIP108422	21 57 51.5	-61 12 50	8.9	G8V	450	possible target	23	9
HIP108556	21 59 24.2	-42 48 36	7.71	K5III	300		1	1
HIP109973	22 16 26.6	-41 37 38	5.11	G8III	240		1	1
HIP110204	22 19 23.7	+15 32 45	6.91	K2V	180		2	2
HIP111315	22 33 04.1	-07 10 27	8.75	K5	450		2	2
HIP111791	22 38 35.7	-63 34 21	8.97	G8/K1III	450	possible target	9	6
HIP112166	22 43 02.9	+16 30 15	9.97	K0	900	binary	1	1
HIP112267	22 44 21.3	-14 40 34	7.09	K4/K5III	200		1	1
HIP113029	22 53 28.3	+08 26 19	9.56	K0	1200	binary	1	1
HIP113356	22 59 59.4	+05 09 34	7.15	K0	150	follow up	2	2
HIP113902	23 03 59.6	-58 41 38	5.79	K0III	300		1	1

Continued on next page

Table B.2 – *Continued from previous page*

Target	RA	DEC	Mag	Spectral Type	Exp Time	Notes	Total Obs	Total Nights
HIP114072	23 06 10.8	58 41 38	8.14	F0V	300	possible target	43	13
HIP114155	23 07 06.7	+25 28 06	4.76	K0IIp	60		2	2
HIP114414	23 10 16.6	-35 23 56	8	K5III	300		2	2
HIP114698	23 14 05.7	+10 09 39	9.4	K2	650		2	2
HIP114908	23 16 30.4	-27 04 50	7.36	K5/M0III	180		2	2
HIP115102	23 18 49.4	-32 31 55	4.41	K1II	240		1	1
HIP116799	23 40 18.1	+04 48 24	7.44	K5	240		1	1
HIP118222	23 58 49.1	+09 33 00	8.25	K5	300	binary	2	2

Appendix C

Input File Formats for the Reduction and Analysis of Targets

Data collected as per the methodology discussed in Chapter 3 needs to be converted into wavelength calibrated spectra. To achieve this, a custom-written package called ESpRIT (Echelle Spectra Reduction: an Interactive Tool) is used.

A summary of the operation of ESpRIT was also given in Chapter 3 and the various input files required to take the raw observation to the final map are shown in this Appendix.

A more detailed description can be found in Donati and Collier-Cameron (1997)

Since the 2.3-m data is very different from the AAT data (for which ESpRIT was written) a number of modifications are necessary. Before the data can be used by ESpRIT the headers need to be modified. After the headers and Julian Date issue are fixed then the initial data reduction needs four steps to turn the modified raw frames into wavelength calibrated spectra and then three more steps to create the map.

Each of these steps require input files and this section provide typical examples of these files.

C.1 Preparation of Data

This step modifies the FITS headers to work with the soft are and to update the Julian Date using IRAF.

Table C.1: The following table shows the FITS Header Modifications and additions which are needed for ESpRIT to work with 2.3-metre data.

OBSERVAT	SSO
TELESCOP	2.3 m
EPOCH	2012.271533
UTDATE	2012-04-09T16:15:20.5
HASTART	-2:55:50
HAEND	-2:40:47
ZDSTART	37.59457
ZDEND	34.41
UTSTART	16:15:21
UTEND	16:30:21
MEANRA	274.9683333
MEANDEC	-29.27583333
UTMJD	56026.67734
TOTALEXP	899.993
STSTART	15.41425
STEND	15.66502778
LAT_OBS	-31.27336
LONG_OBS	149.0612
ALT_OBS	1149
JD	2456027.183
HJD	2456027.184
LJD	2456027

This is a Typical Input File for Creating a Master Flat for use in the calibration process. A similar process is run to create a Master Bias as well.

Table C.2: Typical Input file for creating a master flat

Name of first file	**2011012100012.fits**
Median Value	**D**
No of Files you want to operate on	**5**
List of filenames	**2011012100043.fits**
	2011012100044.fits
	2011012100045.fits
	2011012100046.fits
Save	**s**
Output as a 16 bit fits file	**16**
Master Flat Filename	**flat.fits**
Quit:	**q**

C.2 Step 1: Geometry Correction

This is a typical input file to set up the geometry of the chip, to trace the echelle spectra on the detector so the software knows where to find information it needs. Detector geometry data is manually entered via the *geom.in* file. The software then analyses the flat, bias and arc frames and generates polynomials for tracing on the spectral orders on the CCD and is output to the *geom.dat* file. The input file provides an estimate of the location of the centre of the field and the width of the first order. The ESpRIT code then locates and traces each order in the flat-field frame.

Table C.3: Typical *Geometry_23m* Input File

Flat field exposure:	
Name of file to read FITS data from	**flat.fits**
Comparison:	
Name of file to read FITS data from	**arc.fits**
for Fabry-Perot exposure (not used in DI)	**n**
Fabry-Perot:	
Name of file to read FITS data from	**bias.fits**
Input CCD subformat (pix0, npix for each axis)	**55 2045 1 2050**
Is dispersion along columns	**n**
Is wavelength increasing with pixels along orders	**n**
Do you want to invert orders	**n**
Centre point of first order (at row 1000)	**60.5**
Approximate separation between orders	**107**
Starting order	**34**
Increment number for orders	**1**
Number of orders	**24**
Correct for slit curvature	**y**
File to save data to	**geom.dat**
Do you want to save reduced comparison spectrum	**y**
File to Save Stokes I profile to	**th.s**

C.3 Step 2: Wavelength Calibration

The script *wcal_23m* takes the information manually specified in the *wcal.in* file and then generates polynomials that represent the wavelength calibration for each spectral order. In the *wcal.in* file the initial wavelength position and dispersion measurement for the first order are manually entered. The ESpRIT code then attempts to calibrate the first selected order; starting with the initial

input and an atlas of known line positions, the code performs a preliminary identification of lines which should be present in the selected order and then iteratively calibrates each order.

Table C.4: Typical Input File for Wavelength Calibration

Uncalibrated spectrum of comparison lamp	
Name of file to read Stokes I profiles from:	**th.s**
How many orders in the spectrum	**24**
Number of starting order (pix 0 to 2044) and order increment:	**34 1**
Do you want to use an a priori calibration table (y/n):	**n**
Approx lam0 (nm) and disp. (nm/pix) for order 34:	**653.524 0.09154**
Name of file to read th-ar line wavelengths from:	**thar.arc**
Name of file to save Stokes profiles to:	**th.ws**
Name of file to save calibration table to:	**calib.dat**

C.4 Step 3: Spectra Extraction

Extraction of the Intensity Spectra requires the extraction of the stellar exposure, a flat-field exposure and a bias exposure in conjunction with the output of the previous two steps.This produces a preliminary spectrum, which is automatically corrected for the heliocentric motion.

Table C.5: Typical Input File for *Extract_23m*

Stellar Exposure:	
Name of file to read FITS data from:	**ABDor230120.fits**
Flat field exposure:	
Name of file to read FITS data from	**flat.fits**
Bias:	
Name of file to read FITS data from	**bias.fits**
Name of file to read geometry data from:	**geom.dat**
Detector gain (e/ADU) and read noise:	
(from RSAA detector webpage)	**2.44.4**
Optimal Extraction of spectrum y/n	**y**
Rejection threshold - use default value	**10.0**
Do you have calibration information	**y**
Name of file to read calibration table from:	**calib.dat**
Do you want spectrum to be normalised	**y**
Name of file to save stokes profiles to:	**ABDor230120.dat**

C.5 Step 4: Removing the Telluric Lines

Typical Inputs for *sum_ tel* for the Removing of Telluric Lines

In this step the telluric lines from the spectrum are extracted. This allows the software to make minor shifts in the spectrum to correct for small instrumental shifts. It essentially extracts the telluric lines to produce a LSD profile of these lines, fits a Gaussian to the LSD profile and estimates the shift in that profile and compares what the position should be.

Table C.6: Typical Input File for *Sum_ tell*

Intensity Spectrum: Name of file to read Stokes I data from:	**ABDor230120.dat**
Name of file to read lines from:	**/toolkit/atlas/tel**
Weighting:	
0: g, 1: prof∗g, 2: lam∗prof∗g, 3: prof,	
4:lam∗prof, 5: 1, 6:prof∗ (lam∗g)^2:	**2**
Upper and lower velocities in km s^{-1}:	**−210210**
Velocity step in LSD profile in km s^{-1};	**4.2**
Width of Fourier filtering (pixel):	**4.2**
Do you want to save results	**y**
Name of file to save Stokes profiles to:	**tel.lsd**

Typical Inputs for *gfit_ tel.in*

Table C.7: Typical Input File for *Gfit_ tell*

Name of file to read Stokes I profiles from:	**tel.lsd**
File to be selected (1-2):	**1**

C.5.1 Typical Input File for *Gfit*

Table C.8: Typical Input File for **Gfit**

Name of file to read Stokes I profiles from:	**ABDor230120.dat**
File to be selected (1-2):	**1**
Shift in km/s:	**2.88**
Name of file to save Stokes profiles to:	**ABDor230120dopcor.dat**

C.6 Step 5 - Least Square Deconvolution

Typical Inputs for *sum.in*

Table C.9: Typical Input for *sum.in* to create an LSD Profile

Name of file to read Stokes I profiles from	**ABDor230120dopcor.dat**
Name of file to read lines from:	**/Users/donna/toolkit/atlas/k1**
Weighting:	
0: g, 1: prof∗g, 2: lam∗prof∗g, 3: prof,	
4:lam∗prof, 5: 1, 6:prof∗ (lam∗g)^2:	**2**
Upper and lower velocities in km s^{-1}	**−100 210**
Velocity step in LSD profile in km s^{-1}	**4.2**
Width of Fourier filtering (pix):	**4.0**
Do you want to save results:	**y**
Name of file to save Stokes profiles to:	**ABDor230120.lsd**

C.7 Step 6: Reformatting the Line Profile Data

List of Typical Parameters and Layout for *reformat.in*

Reformat takes the data from **sum** and then makes the .dat file required for **ZDICam** by taking the data from the previous steps and rearranging them into a form suitable for the imaging codes in the next step to make the intensity map. and rearranges it for input to the imaging codes. It also make use of photometric data if it is available.

Table C.10: Typical Input values for *reformat.in*

Do you want to include Photometry:	**n**
Is it a binary star:	**n**
How many phases to read:	**10** *will equal number of profiles you have*
Number of lines to extract:	**1**
p	**Mean**
lam (nm)	**0.00**
Left and right span (nm)	**−100100** (*v***sin***i***frompointsselectedonprofilewings**)
Shift (nm)	**valueofradialvelocity**
Continuum level for line 0	**0.9985**
Name of file to read Stokes I profiles from:	**ABDor230101.lsd**
File to be selected	1
Type of Observation	**I** *(from intensity profile)*
Phase	**0.0000** *(from calculation)*
SN	**877** (from *sum.log*)
Resolution for spectrum 0	**24, 000** (from *wcal.out*)
File to output data to	**ABDor.s**

Table C.11: Input Table for use in Creating *reformat.in*

filename	**profile**	**Type of obs**	**phase**	**SNR**	**resolution**
ABDor110121014.lsd	1	I	0.0000	857	24000
ABDor110121015.lsd	1	I	0.0138	854	24000
ABDor110121017.lsd	1	I	0.0746	854	24000
ABDor110121018.lsd	1	I	0.0884	849	24000
ABDor110121019.lsd	1	I	0.1022	845	24000
ABDor110121020.lsd	1	I	0.1160	840	24000
ABDor110121021.lsd	1	I	0.1300	846	24000
ABDor110121022.lsd	1	I	0.1437	848	24000
ABDor110121023.lsd	1	I	0.1575	846	24000
ABDor110121024.lsd	1	I	0.1715	844	24000
ABDor110121025.lsd	1	I	0.1853	839	24000
ABDor110121026.lsd	1	I	0.1991	800	24000
ABDor110121027.lsd	1	I	0.2129	836	24000
ABDor110121028.lsd	1	I	0.2269	833	24000
ABDor110121029.lsd	1	I	0.2413	825	24000

Gscale normalises equivalent width of all LSD profiles to first LSD profile in list and then takes the information from previous profiles and selects the best. It also flattens out the wings that makes for a better fit to model data. This gives a graphical output of Signal to Noise to Equivalent Width.

Table C.12: Typical Input Values for *gscale.in*

Name of file to read spectral data from:	**filename.s**
Name of file to save spectral data to:	**filename.rs**

C.8 Step 7: Imaging

Typical Input factors for **ZDICam**

The maximum entropy code called ZDICAM was developed by Brown *et al.* (1991); Donati and Collier-Cameron (1997). It works on the principle of a statistical analysis of the output of the image reconstruction that involves the minimum amount of surface spot features to solve for the variations in the observed spectroscopic data. It then used a χ^2 value to determine what the best fit for the model against the given information, where the lower χ^2 value

the more correct the solution.

Table C.13: Typical Input Values for *zdicam.in*

Is it a magnetic image:	**n**
Read an old image file:	**n**
Number of grid points, inclination angle $v\sin i$:	**5000 60 90.0**
Photospheric EW fit:	**n**
Default filling factor:	**1**
Default Photospheric temp; spot temp T$_eff$:	**5000 3500**
Delta and gamma for differential rotation:	**0.000 0.0000**
Outfile from gscale:	**ABDor.rs**
Profile tab - this file is a presentation of a slowly rotating star:	**Gau_14.tab**
Multiplication factors for line:	**0.6400.320**
Do you want to use mean LSD profile:	**y**
What is the largest phase smearing allowed?	**1**
Oversampling factor:	**1**
Do you wish to weigh the pixels by cell area?	**Y**
Lfac value for iteration - assuming a linearisation of the maximum entropy:	**1**
Input values for Caim and Maxit:	**0.2 25**
Output brightness file text file:	**ABDor.b1**
Do you want to save synthetic spectra:	**y**
Output spectral data - modelled LSD profiles:	**ABDor.s1**

Creating a Map Using GDATA2 with Input File *new.in*

Table C.14: Typical Input values for new.in

Rectangular, polar or spherical view (r/p/s):	**S** spherical, **p** polar, **r** - rectangular
Number of plots, npx, npy:	**111**
Name of file to read brightness data from:	**zdicam.b1**
Name of file to read spectral data from:	**zdicam.s1**
Plot color (bw: **0**; brown:**1**, blue/red:**2**, green/red:**3**)	**1**
Phase range:	**0.01.0**
Thresholds:	**1.00.0**
Label on x axis:	**SpotOccupancy**
Title	**Hip43720**

Appendix D

Two Ultra-Rapidly Rotating Young Active Targets for Doppler Imaging Follow up.

D.1 Introduction

The following two stars are highlighted, as they are potential targets for future Doppler Imaging. Each LSD profiles of the individual stars show spectral line deformation in their profiles which may indicate the presence of starspots. Each star has been observed on multiple occasions and show definite variation in its LSD profile between observations. The stars will need further examination to determine if the line deformation is due to spot activity or the star being a binary. These stars were also chosen as their Hα profiles show that Hα is in emission in these stars. If there is variation in the Hα profile, as demonstrated for HIP2729 and HIP108422, then this could indicate that the stars have prominences, that could be mapped, using the technique of Doppler Imaging on the Hα profile alone (Donati *et al.*, 2000). It is thought that prominence expulsion could play a major part in the angular momentum loss from a star, and prominence mapping can be done on relatively faint stars, as evidenced by Donati *et al.* (2000).

D.2 HIP2729 (HD3221)

This is K5V dwarf star with a mass of 0.9 solar masses and a $v\sin i$ of around 130 km s^{-1} and an age of around 20-30 Myr (Scholz *et al.*, 2007; Zuckerman *et al.*, 2004). This star has a short period of approximately 9 hours and displays active spot activity as well as possible prominence activity. It is a possible member of the Tucana-Horologium Association and is located around 54.9 parsecs from the Earth (Torres *et al.*, 2006). It is a chromospherically active star with a Hα equivalent width of 2Å$\pm$ 0.24 Hα.

The profile in Figure D.1 shows the LSD profile for this star and the Hα profile. The deformation of the line profile is most probably due to the presence of large spot groups. In this case there is a very flat bottom to the profile, which is usually indicative of a large polar spot. The Hα profile of HIP2729 shows some possible variability which may possibly be due to prominence activity.

D.2.1 Stellar Parameters

Table D.1 shows the various stellar parameters from literature for HIP2729.

The initial exposure times for this star were 650 seconds and showed the broad LSD profile and and characteristic "bump" in the profile. However, the

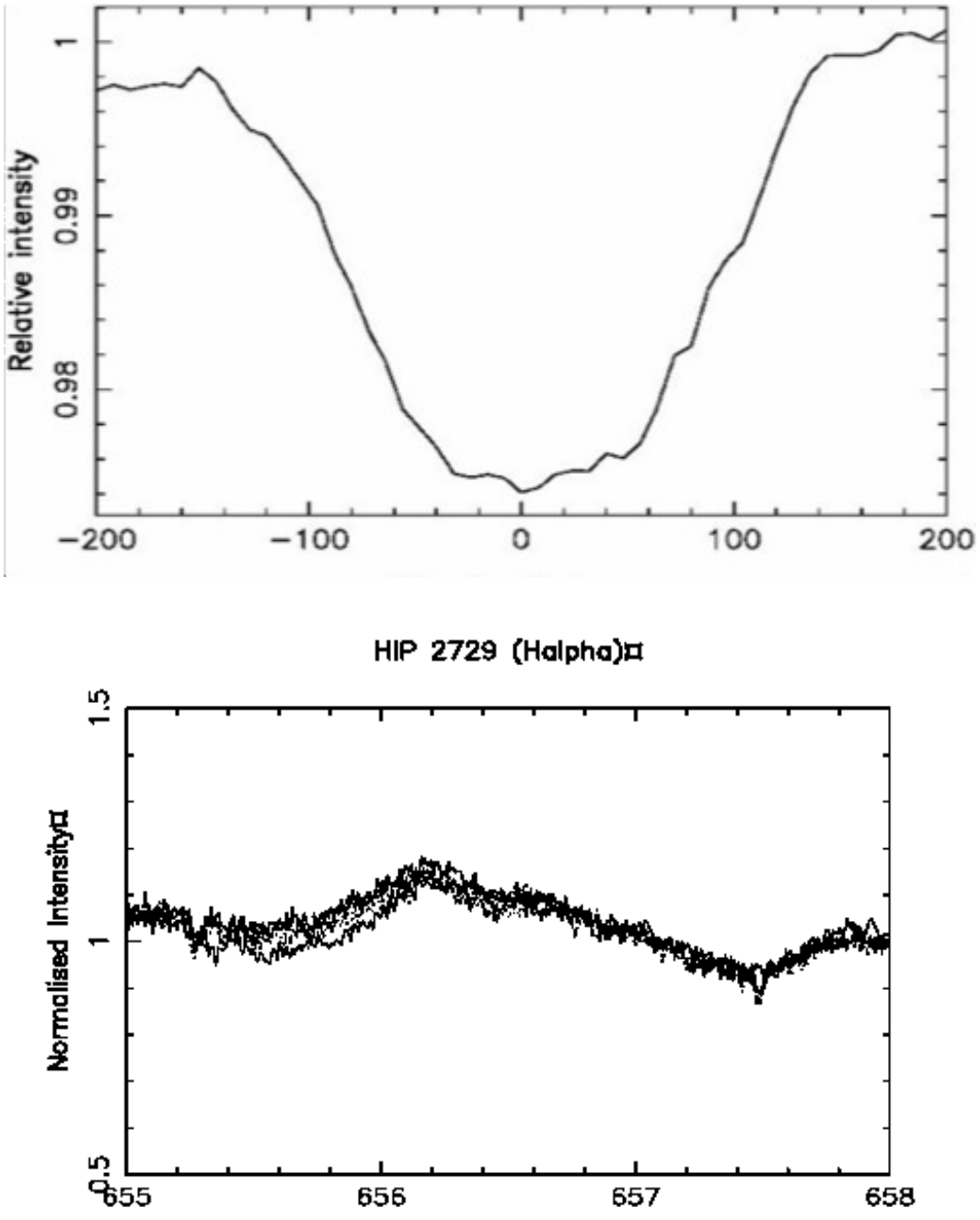

Figure D.1: Least-squares deconvolution profile (upper), and Hα profile (lower), for the Ultra-Rapid Rotator: HIP2729

Table D.1: Stellar Parameters for HIP2729.

Parameter	Value	Refs
Age	20-30Myr	(Zuckerman and Webb, 2000)
Distance	54.9 pc	(Scholz *et al.*, 2007)
Magnitude (V)	9.56	(van Leeuwen, 2007)
Spectral Type	K5V	(Scholz *et al.*, 2007)
	K4Ve	(Torres *et al.*, 2006)
Stellar axial Inclination, i	55° ±5°	(Zuckerman *et al.*, 2011)
Projected equatorial rotation velocity $v\sin i$	127 ± 2.5 km s^{-1}	(Torres *et al.*, 2006)
Photospheric temperature	4,400 ° ± 30 K	(Zuckerman *et al.*, 2011)
Spot temperature	3,800° ± 30 K	(Zuckerman *et al.*, 2011)
Radial velocity	5.7 km s^{-1}	(Malo *et al.*, 2013), (Torres *et al.*, 2006)
Mass	0.9 solar masses	(Zuckerman *et al.*, 2011)
Radius	1.1 Solar Radius	(Zuckerman *et al.*, 2011)
Rotational Period at Equator	∼0.4±0.1days	(Torres *et al.*, 2006)

original profiles were very 'noisy' and the signal-to-noise was only 40 in order 34 so exposure time was increased to 900-seconds. This was necessary to gather sufficient light to undertake effective Doppler Imaging as it is the faintest of the targets for which a preliminary collection of snapshots were taken. It was necessary to select an exposure time that also reduced the generating of rotational broadening due to the rapid rotation of ≈128km s^{-1}. Since the star is believed to have a period of only 0.4± 0.1 days the star rotates 1° in 96 secs so 900 seconds would see it cover ≈9.4° which is 2.6% of the rotational period. With this exposure time for a star of this magnitude it was still possible to obtain a signal-to-noise ratio of 78 at order 34 and an overall mean SNR of 780 in the LSD profile was achieved.

HIP2729 certainly displays spot deformation over a short period of time. From its Hα profile it also may have prominence activity and this is something that will be followed up on future observing runs. It is classified as an ultra-rapid rotator being between 100 and 200 km s^{-1}. Since HIP2729 has Hα emission but no apparent HeI, although an explanation may be that the extreme broadening go the spectral line is hiding the HeI line. It is most likely caused by the chromospheric activity broadened by its fast rotation rather

than by being an accretor, another cause could be an undiscovered close binary. However, it has been studied extensively in X-ray, radio and UV and including the Spitzer and Hubble Space Telescope looking for a planet or sub-stellar companion so far without success. The star has been observed on one or two half nights over the last 3 years and there is no evidence, as yet, in the LSD profile of a secondary star.

D.3 HIP108422 (HD208233)

This is a Pre Main Sequence 1.1M_{odot} G8 or G9 star, considered to be a member of the Tucana-Horologium Association and therefore aged around 20-30 Myr. HIP108422 is a ultra-rapid rotator with a projected rotational velocity *vsini* of 128 km/s Zuckerman and Webb (2000).

Chauvin *et al.* (2003) believes that this star has a low mass companion as shown in Figure D.2. The presence of a low mass companion can cause variations in the radial velocity and Hα activity can also be a result of a stellar or sub-stellar companion.

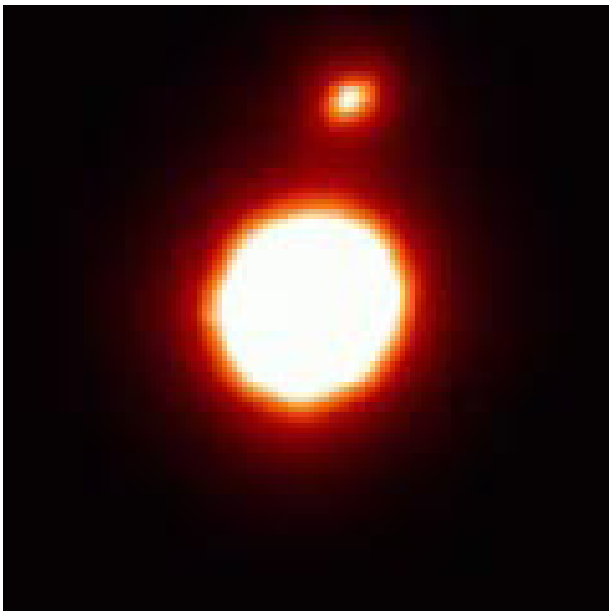

Figure D.2: ADONIS/SHARPII AO classical imaging of HIP108422 showing a possible low mass companion. (Chauvin *et al.*, 2003)

Table D.2: Stellar Parameters for HIP108422

Parameter	Value	Refs
Distance	45.9 pc	(Scholz *et al.*, 2007)
		(Chauvin *et al.*, 2003)
Magnitude (V)	8.9	(Scholz *et al.*, 2007)
Spectral Type	G8V	(Scholz *et al.*, 2007)
	G9IV	(Torres *et al.*, 2006)
Stellar axial		
Inclination, i	55°±5°	(Zuckerman *et al.*, 2011)
Projected equatorial		
Rotation velocity $v\sin i$	148 ± 29.2 km s^{-1}	(Torres *et al.*, 2006)
Photospheric temperature	5200 ° ± 50 K	(Zuckerman *et al.*, 2011)
Spot temperature	3,900° ± 30 K	(Zuckerman *et al.*, 2011)
Radial velocity	1.2 km s^{-1}	(Malo *et al.*, 2013),
		(Torres *et al.*, 2006)
Mass	1.18 solar masses	(Zuckerman *et al.*, 2011)
Rotational Period at	∼0.5± 0.1 days	(Torres *et al.*, 2006)
Equator		

D.3.1 Stellar Parameters

Table D.2 shows a list of parameters for this ultra-rapid rotator. This star has a 0.5 day rotational period and a $v\sin i$ of 128 km s^{-1}.

Exposures of 600 seconds duration were used to reduce phase smearing (≈ 1 - 2% of the rotation period) and still gather sufficient light to undertake effective Doppler Imaging without generating rotational smearing of the spots due to the rapid rotation of ≈128km s^{-1}. Since the star is believed to have a period of only 0.5± 0.1 days so it would rotate 1° every 2 minutes so 600 seconds would see it cover 5° which is just 1.4% of the rotational period. Even with this exposure time for a star of this magnitude a signal to noise ratio of 89 at order 34 and an overall mean SNR of 975 in the LSD profile was achieved.

Figures **??** and D.3 shows the line deformation in the profile that could most probably be due to the presence of large spot groups. ThHα profile provides evidence that may possibly be prominence activity and needs to be followed up on future observing runs.

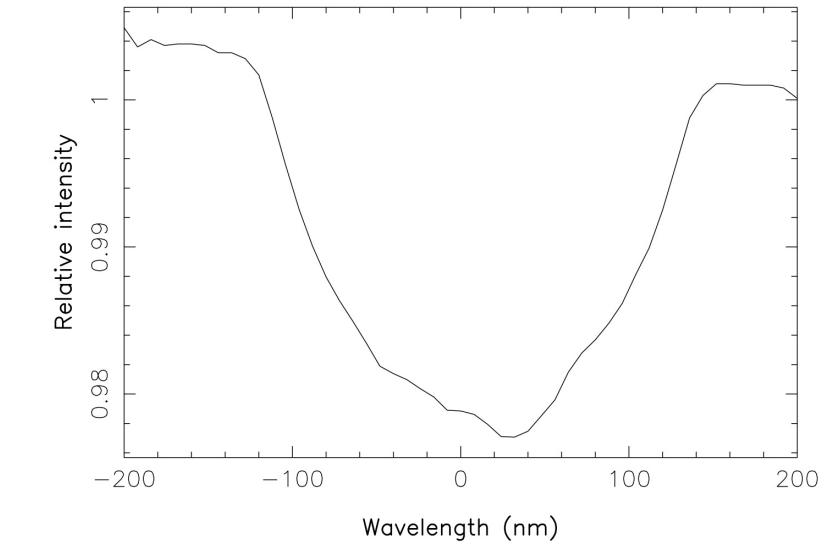

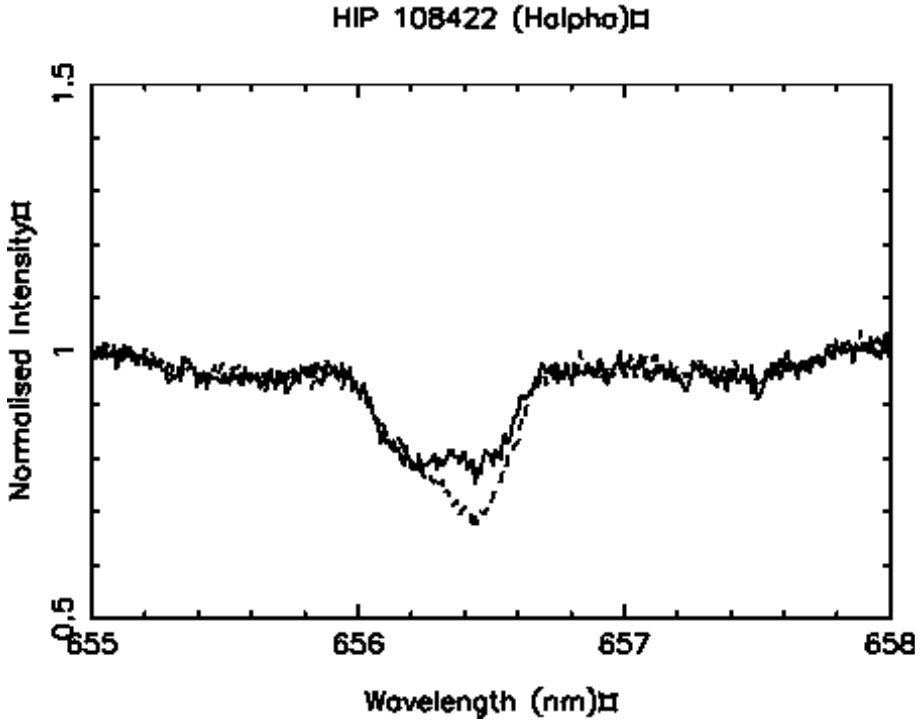

Figure D.3: Hα profile, for the Ultra-Rapid Rotator: HIP108422, taken on two separate observations.

D.4 Summary

These are only 2 of over 21 single young active stars found during the Southern DI Candidate survey. Their magnitude, rotational periods and $v\sin i$ make them ideal targets for followup with the ANU 2.3-metre telescope and echelle spectrograph.